AEDC-TR-91-17

Engineering Model of Unsteady Flow in a Cavity

R. C. Bauer and R. E. Dix
Calspan Corporation/AEDC Operations

December 1991

Final Report for Period October 1989 through September 1991

Approved for public release; distribution is unlimited.

**ARNOLD ENGINEERING DEVELOPMENT CENTER
ARNOLD AIR FORCE BASE, TENNESSEE
AIR FORCE SYSTEMS COMMAND
UNITED STATES AIR FORCE**

NOTICES

APPROVAL STATEMENT

This report has been reviewed and approved.

PAUL LACASSE, Capt, CF
Facility Technology Division
Directorate of Technology
Deputy for Operations

FOR THE COMMANDER

KEITH L. KUSHMAN
Director of Technology
Deputy for Operations

REPORT DOCUMENTATION PAGE

Form Approved
OMB No. 0704-0188

1. AGENCY USE ONLY (Leave blank)	2. REPORT DATE	3. REPORT TYPE AND DATES COVERED
	December 1991	Final, October 1989 -- September 1991

4. TITLE AND SUBTITLE
Engineering Model of Unsteady Flow in a Cavity

5. FUNDING NUMBERS
PE - 62602F

6. AUTHOR(S)
Bauier, R. C. and Dix, R. E., Calspan Corporation/AEDC Corporation

7. PERFORMING ORGANIZATION NAME(S) AND ADDRESS(ES)
Arnold Engineering Development Center/DOT
Air Force Systems Command
Arnold AFB, TN 37389-5000

8. PERFORMING ORGANIZATION REPORT NUMBER
AEDC-TR-91-17

9. SPONSORING/MONITORING AGENCY NAMES(S) AND ADDRESS(ES)
Arnold Engineering Development Center/DO
Air Force Systems Command
Arnold AFB, TN 37389-5000

10. SPONSORING/MONITORING AGENCY REPORT NUMBER

11. SUPPLEMENTARY NOTES
Available in Defense Technical Information Center (DTIC).

12a. DISTRIBUTION/AVAILABILITY STATEMENT
Approved for public release; distribution is unlimited.

12b. DISTRIBUTION CODE

13. ABSTRACT (Maximum 200 words)
A mathematical model was assembled from fundamental fluid dynamic relations and turbulent single-stream mixing zone relations to predict spectra, i.e., the frequency and amplitude, of unsteady pressures acting in a rectangular cavity exposed to an external flow parallel to the cavity opening. Characteristics of the approaching boundary layer are expected as inputs, thereby allowing computation of spectra for cases of mass-injection upstream of the cavity. The equations were compiled as a code that can be run in less than 15 sec on a personal computer. Maximum dynamic loads acting on the contents of the cavity can be estimated, in addition to the primary frequencies of oscillation.

14. SUBJECT TERMS
aeroacoustics, **CAP Code**, **prediction models**, **boundary layers**, **Navier-Stokes solutions**, **unsteady flow**

15. NUMBER OF PAGES
91

16. PRICE CODE

17. SECURITY CLASSIFICATION OF REPORT	18. SECURITY CLASSIFICATION OF THIS PAGE	19. SECURITY CLASSIFICATION OF ABSTRACT	20. LIMITATION OF ABSTRACT
UNCLASSIFIED	UNCLASSIFIED	UNCLASSIFIED	SAME AS REPORT

COMPUTER GENERATED

Standard Form 298 (Rev. 2-89)
Prescribed by ANSI Std Z39-18
298-102

PREFACE

The work reported here was done at the Arnold Engineering Development Center (AEDC), Air Force Systems Command (AFSC), at the request of the AEDC Directorate of Technology (AEDC/DOT). The work was accomplished by Calspan Corporation, AEDC Operations, operating contractor for the aerospace flight dynamics test facilities at AEDC, AFSC, Arnold Air Force Base, Tennessee, under AEDC Project Number DC72PW. Mr. Daniel E. Schatt, a graduate student at the University of Tennessee Space Institute (UTSI), made significant contributions to the work as a summer intern sponsored by the Air Force Office of Scientific Research (AFOSR). Mr. Schatt's contributions are gratefully acknowledged by the authors. The Air Force Project Manager was Captain (CF) J. E. P. Lacasse, AEDC/DOTR. Work was accomplished during the period October 1989 through September 1991, and the manuscript was submitted for publication on December 5, 1991.

CONTENTS

ILLUSTRATIONS

TABLE

APPENDIXES

1.0 INTRODUCTION

Unsteady flow fields in and near an open cavity excited by an external flow parallel to the plane of the opening have been studied for at least a hundred years — literally. An historical perspective was provided by Covert (Ref. 1), who cited works by Strouhal, Rayleigh, and Kohlrausch in the late nineteenth century. By the 1950s, Krishnamurty and Roshko were studying acoustic radiation from cavities for NACA (Refs. 2 and 3, respectively), and in the early 1960s, Plumblee, Gibson, and Lassiter at Lockheed-Georgia performed both theoretical and experimental studies of cavity flow, including a deep cavity of length-to-depth ratio (L/D) of only 0.8 (Ref. 4). In 1964, J. E. Rossiter, reporting to the Aeronautical Research Council in the United Kingdom, produced what is still the most widely used method for estimating the frequencies of pressure oscillation to be expected in a cavity flow field (Ref. 5). Later in the 1960s and early 1970s, East (Ref. 6), Heller, Holmes, and Bliss (Ref. 7), and Smith and Shaw (Ref. 8), among many others, performed experiments of flow over a cavity and the associated induced pressure oscillations, building on Rossiter's earlier work. In 1973, Bilani and Covert (Ref. 9) suggested that the oscillations in the cavity were associated with vortex roll-up and the concomitant instability in the shear layer, a thought that drew concurrence by Tam and Block at NASA (Ref. 10). Experiments have continued into the 1980s, with Clark, Bartel, and McAvoy, and Kaufman and Maciulaitus for the USAF Wright Aeronautical Laboratories examining actual cavities in aircraft (Refs. 11, 12, and 13). Work at NASA has continued also, with the examination of cavity flow fields in rectangular cavities of various L/D at subsonic, transonic, and supersonic speeds (Blair, Stallings, Wilcox, and Plentovich, Refs. 14, 15, and 16).

The works cited, as well as the many others not mentioned, may be sorted into three categories: experimental investigations, acoustic solutions, and Navier-Stokes solutions. (Extensive bibliographies are available in Refs. 7 and 12.) One of the more comprehensive and practical experimental studies has been a recent test program at the Arnold Engineering Development Center (AEDC) by Dix (Ref. 17). Data obtained in the program have been used to verify Navier-Stokes solutions and to help develop simpler, semi-empirical methods. Recently, with the availability of large and fast computing machines, the analytical approach to cavity flow-field prediction has moved beyond approximations to fluid dynamic phenomena through the use of fundamental equations and empirical constants to full, time-accurate, Navier-Stokes solutions. Several investigators have published solutions, including Om, Baysal, Rizzetta, Suhs, and Dougherty (Refs. 18 through 23). However, computer time on the order of 100 cpu-hr of a multiple-cpu, parallel-processing, Class VI computer was required. However, an encouraging trend has been demonstrated by Suhs at AEDC (Ref. 21) in showing that it is possible to estimate mean pressure distributions and rms pressure distributions in a cavity with time-accurate Navier-Stokes solutions in about 20 cpu-hr by applying a thin-layer viscosity approximation (restricting viscous effects to a thin layer near the cavity boundaries), and assuming symmetry about the longitudinal center, or XZ, plane of the cavity. However, since a computed spectrum was not included, the results cannot be used to estimate the dynamic forces acting on the structure of the cavity. Simpler acoustic theories have been applied in an attempt to predict the spectrum, but these can only be used to predict the natural frequencies based on the dimensions of the cavity, and not the magnitude of the peak pressures that occur at these frequencies. A fresh attempt has been made, therefore, to examine the fundamental fluid dynamic phenomena involved, with the intent of developing a means of predicting at least a first-order estimate of both the frequency and amplitude of the tones occurring in a cavity.

Data to support the prediction study was acquired during the recent test program by Dix (mentioned previously) involving a simple flat plate and cavity model. (The test program has been documented in an AEDC Technical Report, and is summarized in Appendix A.) The database includes surface pressure measurements acting on the plate/cavity model recorded using both conventional static-pressure instrumentation and fluctuating-pressure transducers.

2.0 DEVELOPMENT OF A CAVITY ACOUSTIC MODEL

2.1 IMPLICATIONS OF TEST DATA

Before proceeding with development of a math model of cavity acoustics, it is important to examine some typical plate/cavity surface pressures from the tests. Surface pressure profiles measured along the centerline of the three cavities (L/D values of 4.5, 9.0, and 14.4) are illustrated in Fig. 1 for a range of Mach numbers from subsonic to high transonic. Conventional static-pressure measuring techniques were used, but the recorded pressures were decidedly unsteady. (The profiles illustrated in Fig. 1 are actually mean profiles calculated from 6 to 12 repeated data points. The statistical standard deviation of the repeated pressure measurements is also illustrated in Fig. 1.) At all conditions, the standard deviation of the repeated measurements exceeded the uncertainty interval for the surface pressure measurements (See Table A-2 in Appendix A) over much of the length of the deeper cavity (L/D = 4.5), over some of the length of the transitional cavity (L/D = 9.0), and over almost none of the length of the shallow cavity (L/D = 14.4). The measured surface pressures in the transitional and deep cavities were clearly unsteady. Furthermore, the flow over the deeper cavity (L/D = 4.5) did not expand into the cavity at any Mach number (Fig. 1a), whereas the flow over the most shallow cavity (L/D = 14.4) expanded into the cavity at all Mach numbers (Fig. 1c). Flow over the L/D = 9.0 cavity expanded into the cavity at subsonic conditions, but did not for Mach numbers of 1.50 and higher (Fig. 1b). Behavior of this type has led to the widely used designations "open cavity" (L/D < 9), "transitional cavity" (9 < L/D < 13), and "closed cavity" (13 < L/D), according to a model offered by Stallings and Wilcox (Ref. 15), and illustrated in Fig. 2.

Considering the mean pressure profiles illustrated in Fig. 1 to represent essentially root-mean-square (rms) values, it is clear that the maximum rms pressures occurred in the stagnation region at the downstream wall, regardless of cavity L/D. This observation is important in the development of the analytical method presented here.

2.2 THEORETICAL MODEL

A simple mathematical model of cavity acoustics can be developed by considering the amplitudes of pressure fluctuations in a cavity to be attributable to an interaction of fluid dynamic and fundamental acoustic phenomena. First, it is asserted that the turbulent mixing zone that separates the ordered flow outside a cavity from the disordered atmosphere inside a cavity generates a continuous spectrum of acoustic waves that are, in turn, responsible for the pressure fluctuations detected in the cavity. The acoustic waves may be considered to act like relay switches that trigger much stronger pulses in the form of vortices that begin to roll up in the mixing zone as the flow passes over the leading edge of the cavity. Although the acoustic amplitudes may vary with frequency, the strengths of the created vortices are equal, as determined by the constant vorticity at the edge of the cavity.

Second, a variable damping term is proposed for inclusion in the frequency response equation for the cavity. The value of the damping term is stated as an empirical function of the relative magnitude of the frequencies of the fundamental acoustic modes of the cavity and the "edgetones" that are generated as the flow separates at a cavity edge. Minimum damping is expected to occur when an edgetone frequency is equal to one of the three fundamental acoustic frequencies, producing a maximum pressure amplitude at the edgetone frequency.

Finally, as stated in Section 2.1, the maximum rms pressure in a cavity occurs at the downstream wall where the turbulent mixing zone impinges, leading to an assertion that the maximum rms pressure is related to the maximum rms pressure in the turbulent mixing zone. Therefore, a method is offered for estimating the maximum rms pressure that would occur at the detected frequencies.

2.3 FUNDAMENTAL EQUATIONS

A theoretical approach to predicting the fluctuating flow field in a cavity must include mathematical models of the following quantities:

1. acoustic resonant frequencies,
2. edgetone frequencies,
3. pressure on downstream wall of cavity as a function of time,

4. frequency response,
5. damping phenomena,
6. maximum rms pressure in the turbulent mixing zone, and
7. spectra reference pressure.

The mathematical models will be discussed in sequence in the following sections.

2.3.1 Acoustic Resonant Frequencies

Some typical SPL spectra for three cavities are illustrated in Figs. 3, 4, and 5. Of particular interest are the values of the tones that are detected at the location of transducer K18. (The output of transducer K18, located as illustrated in Fig. A-4, is used throughout as a criterion, since that location was in the region of highest acoustic levels in the cavity, and was never covered by the adjustable floor.) Also marked in Figs. 3 through 5 are the natural, or fundamental, acoustic modes for the cavity. The fundamental acoustic modes may be likened to Helmholtz resonances, but the analogy is not perfect since the cavity is not a totally enclosed volume with only a small aperture to the surrounding environment. Another possible analogy is that of a classical closed organ pipe, (which, by definition, is physically closed on just one end). In this classical model, the closed end is a displacement node; but again the analogy to a cavity is weak, since the cavity is closed on both ends. It is asserted that the best analogy is that of the open organ pipe, for which each end is a pressure node, i.e., the pressure amplitude at each end is a maximum. Then, proceeding from the fundamental relationship for wave motion,

$$f = \frac{a}{\lambda_a}$$

and assuming the cavity responds like an open organ pipe, the frequencies of the fundamental acoustic modes for the length L, and width, W, are

$$f_L = \frac{a_t}{2\,L}$$

and

$$f_W = \frac{a_t}{2\,W}$$

Calculation of the fundamental depth mode is more difficult, since the top of the cavity is open, like the classical closed organ pipe. The equation selected was developed by Bauer for a tube (See Appendix B),

$$f_D = \frac{a_t}{2\pi D}\sqrt{\frac{2}{\gamma}}$$

(In this instance, the parameter γ represents the ratio of specific heats for a gas. In other equations, γ represents Rossiter's phase constant, as in Section 2.3.2.) It must be emphasized that the equations cited here apply only to simple rectangular cavities. A more elaborate acoustic analysis must be made for cavities of more complex geometry.

In Ref. 5, Rossiter presents a simple theory for estimating the frequencies of the edgetones that are produced by the shedding of vortices at the upstream edge of the cavity. It is important to note that the tones detected in the cavity experiments do not occur at the fundamental acoustic modes, but primarily at the edgetone frequencies (Figs. 3 through 5). Unfortunately, Rossiter does not offer a method for predicting the magnitudes of the pressure pulses occurring at the edgetone frequencies.

2.3.2 Edgetone Frequencies

The most widely used equation for estimating the edgetone frequencies was developed by Rossiter (Ref. 5),

$$f_e = \frac{V_\infty (m - \gamma)}{L\left(M_\infty \frac{a_\infty}{a_t} + \frac{1}{\phi_d}\right)}$$

where m = 1, 2, 3, ... = the frequency mode number of the edgetone.

Rossiter introduced two empirical parameters in his original formula, γ and ϕ_d, which were shown to apply almost universally to a wide range of cavities of $L/D < 10$ and with thin initial boundary layers. These two empirical parameters will be discussed separately.

2.3.2.1 Phase Constant, γ

Rossiter identified the parameter γ as a phase constant between vortex shedding and acoustic wave response in the cavity. (Rossiter's model of cavity acoustic generation is illustrated in Fig. 6.) By averaging results over the entire range of Mach number used in his experiments, and assuming that the parameter $\phi_d = 0.57$, he suggested that the phase constant was approximately 0.25 of one vortex wave length for a cavity of $L/D = 4.0$. Other values of γ were offered by Rossiter as representing the best choices for the cavities of specific L/D ratio that were included in his investigation. The values are illustrated as discrete data points in Fig. 7, to which both linear and second-order curves were fit. Unfortunately, neither curve fit is satisfactory. Although the same values of γ could be predicted for two of the cavities used in the test program, viz. the L/D = 4.5 and the L/D = 9.0 cavities, extrapolation to L/D = 14.4 was ambiguous. In fact, extrapolation to L/D = 14.4 is not appropriate, since no sharp tones occur in that cavity (Fig. 5), yet no mathematical limitation exists to prevent extrapolation.

Edgetone modal frequency predictions for the cavities used in the recent test program were made using the modified Rossiter equation with values of γ of 0.28 and 0.56 for the L/D = 4.5 and L/D = 9.0 cavities, respectively, consistent with either of the curves fit to the data illustrated in Fig. 7. Predicted and measured frequencies are listed in Table 1 and are illustrated in Figs. 8 and 9. Agreement between predicted and measured values was good for the first three edgetone modes over the range of Rossiter's experiments, viz., $0.40 < M_\infty < 1.20$, and L/D ratios of less than 10. However, for modes 4 and 5, and at Mach numbers above 1.20, the modal frequencies did not occur at the predicted frequencies. No modes could be detected in the L/D = 14.4 cavity; hence, no predictions were made.

Only the longitudinal edgetone frequencies in the cavity are considered in Rossiter's equation; hence, the equation can properly be applied only to cavities with leading edge at zero angle of yaw with respect to the direction of the external flow. Better generality of an analytical method would result from consideration of lateral and vertical, or depth, modes.

A study was made of the phase parameter γ by Dobson (Ref. 24), proceeding from a suspicion that γ might be some function of mode number and Mach number. Adjusted values for γ were identified that provide better frequency predictions (Appendix C). It is important to recall, however, that all the values of γ considered here are valid for an assumed value of the parameter $\phi_d = 0.57$, which is in turn valid only for thin initial boundary layers.

2.3.2.2 Average Vortex Velocity Parameter, ϕ_d

The other parameter, ϕ_d, was defined by Rossiter to be the ratio of the average vortex velocity in passing over the cavity to the free-stream velocity. Rossiter selected an empirical value of $\phi_d = 0.57$ for thin initial boundary layers, but decreasing as the approaching boundary-layer thickness increased. Although a value of 0.57 has often been accepted, East (Ref. 6), identified a range of values for ϕ_d of from 0.35 to 0.65. Later, Heller, Holmes, and Covert (Ref. 7) also accepted 0.57, and Smith and Shaw (Ref. 8) subsequently concurred.

The effect of an initial boundary layer is included here by asserting that the vortices move at the dividing streamline velocity. Hence, the constant ϕ_d becomes the ratio of the dividing streamline velocity to the free-stream velocity. (The theoretical value of ϕ_d for no initial boundary layer in an incompressible flow is 0.6163, which compares favorably with Rossiter's value of 0.57.) A rigorous approach could be taken to calculate ϕ_d, such as the method presented by Bauer in Refs. 25 and 26; however, a semi-empirical equation is used here, beginning with the theoretical incompressible value, and extending to other Mach numbers by fitting Bauer's data,

$$\phi_d = (0.6163 + 0.0178\, M_\infty)\left(1 - e^{-\frac{0.8}{\eta_p}}\right)$$

where $\eta_p = \sigma \dfrac{\delta}{L}$, a turbulent mixing position parameter (Ref. 26),

and σ = the similarity parameter for turbulent mixing, after Bauer (Refs. 27 and 28).

2.3.2.3 Mixing Considerations: Mass Injection

A general model of the approaching flow and the subsequent turbulent mixing that occurs would include the possible injection of fluid into the stream. In fact, fluid injection into the boundary layer upstream of the cavity has been reported by Vakili and Gauthier to be effective in reducing the amplitude of pressure oscillations in the cavity (Ref. 29). First, for the case of no injection, the similarity parameter for turbulent mixing, is defined as σ_0, and values of σ_0 are assumed to be a function of free-stream Mach number (Ref. 28),

$$M_\infty \le 1, \quad \sigma_0 = 3M_\infty + 12$$

$$1 < M_\infty \le 4, \quad \sigma_0 = 8M_\infty + 7$$

$$M_\infty > 4, \quad \sigma_0 = 39$$

If fluid is injected into the cavity, then the mixing is treated as a case of two-stream mixing, and the similarity parameter can be determined from the following equation:

$$\sigma = \sigma_0\left(\frac{1 + \phi_c}{1 - \phi_c}\right)$$

where

$$\phi_c = \frac{V_b}{V_\infty}$$

The velocity of the injected fluid, or bleed-in fluid, V_b, can be determined if it is assumed that the bleed-in fluid is injected uniformly over the upstream wall of the cavity at a density based on the free-stream static pressure and total temperature.

If the bleed flow is injected upstream of the cavity and uniformly over the width of the cavity, then it is assumed that all of the injected fluid remains in the boundary layer, thereby increasing the thickness. If it is further assumed that the velocity profile of the boundary layer is unchanged by fluid injection, then from conservation of mass, the boundary-layer thickness is predicted by

$$\delta = \delta_0 + \frac{\dot{m}_b}{W\,R\,V_\infty\left(1 - \frac{\delta^*}{\delta}\right)}$$

where δ_0 = the initial boundary-layer thickness and for no injection,

and $\frac{\delta^*}{\delta}$ = the ratio of displacement thickness to total thickness.

The quantity δ^*/δ is estimated with empirical equations selected to represent the theoretical results presented by Tucker in Ref. 30 for a 1/7-power velocity profile shape. The equations are listed here for the subsonic and supersonic regimes:

for

$$M_\infty \leq 1 \qquad \frac{\delta^*}{\delta} = 0.0328\,M_\infty + 0.1250$$

and for

$$M_\infty > 1 \qquad \frac{\delta^*}{\delta} = 0.0840\,M_\infty + 0.0738$$

2.3.3 Wall Pressure

Pressure acting on the downstream wall of the cavity is modeled as the sum of 512 forcing-function sine waves of frequencies equal to the first 512 edgetones, and with (possibly) 512 different amplitudes. The model is consistent with the 512 sets of Fourier coefficients determined from the fast Fourier transform (FFT) technique applied in analyzing the experimental data (Appendix A),

$$\frac{P_{wall}}{P_{ref}} = \sum_{n=1}^{512} a_n \sin(\omega_n t)$$

where a_n = the amplitude coefficient of each sine wave, and is simply a special case of the frequency-response equation to be developed in the following two sections,

$\omega_n = 2\pi f_e$

and P_{ref} = the vortex pressure strength, assumed to be the same for all frequencies.

Note that the equation is not exactly a Fourier series, since the difference in consecutive frequencies is not equal to the fundamental frequency because of the phase parameter, λ, in Rossiter's equation.

2.3.4 Frequency Response

It is important to note that in the experimental spectra of the database, the minimum amplitudes are about the same for both low and high frequencies (Figs. 8 and 9). Cavity frequency response is, therefore, very unlike mechanical systems, for which amplitudes decrease continuously at frequencies greater than the natural frequencies. Such response is, however, very similar to the frequency response characteristic derived by Bauer for unsteady flow in a tube (Appendix B). The general equation for a response coefficient that was applied to a cavity is

$$R_s = \frac{\left[1 + \left(\frac{f}{f_e}\right)^2\right]^2 + 4\,d^2\left(\frac{f}{f_e}\right)^2}{\left[1 - \left(\frac{f}{f_e}\right)^2\right]^2 + 4\,d^2\left(\frac{f}{f_e}\right)^2}$$

where f = forcing frequency,

f_e = edgetone frequency,

and d = effective damping ratio.

Note: The effective damping ratio, d, is especially important as a new concept that is introduced at this point. The fundamental property sought for the damping function is that amplitudes at frequencies other than edgetones should be damped, whereas amplitudes at frequencies approaching the edgetones should be progressively less damped, thereby producing a spectrum of the pressure at a cavity wall.

The response coefficient, R_s, can be interpreted as a ratio of the amplitude at a frequency to the amplitude at the forcing frequency. For example, if a single forcing frequency is imposed on the cavity, then the equation for the response coefficient, R_s, would be the equation for each coefficient in the wall pressure equation. Various single forcing frequencies could be used to calculate the theoretical spectra of the wall pressure, but here the actual wall pressure is assumed to result from a continuous spectrum of forcing frequencies. Hence, the forcing frequency, f, in the response coefficient equation is, in sequence, each edgetone frequency ($f = f_e$). Consequently, the coefficients, a_n, in the equation for the wall pressure (Section 2.3.3) become a function of only the effective damping ratio, d_n,

$$a_n = R_{s_n}(f_{e_n}) = \frac{1 + d_n^2}{d_n^2}$$

where n = 1, 2, 3, . . . , 512.

2.3.5 Damping Phenomena

When the preceding equations are used to calculate a spectrum of pressures acting on the downstream wall of a cavity, it is clear that the relative magnitudes of the pressure peaks in the spectrum are determined by the damping ratio, d_n. If the cavity were very deep, with $L/D << 1.0$ (i.e. like a tube), then the damping ratio would be determined by viscous effects, and would be given by the following equation, which can be derived from the material in Appendix B:

$$d_u = \frac{8.885\, \mu_t\, L\, W\, D\, a_t \sqrt{\dfrac{1}{\gamma}}}{P_\infty (L\, W)^2}$$

where μ_t and a_t are the fluid viscosity and sonic speed, respectively, based on the total temperature. (In this instance, the parameter γ represents the ratio of specific heats for a gas. In other equations, γ represents Rossiter's phase constant, as in Section 2.3.2.) However, applying the d_μ equation to a relatively shallow cavity provides an unrealistically small damping ratio (when compared to experimental data). Furthermore, since the expression for d_μ is not a function of frequency, all pressure peaks in the spectrum are calculated as equal, which is generally not true (cf. Figs. 1 through 3). Consequently, it is postulated that another type of damping exists, which is believed to be that predicted by acoustic theories.

As defined here, acoustic "wave damping" is attributable to the mutual interaction of the various acoustic waves, with an ultimate loss of energy out the opening of the cavity. It is assumed to be a simple function of the ratio of edgetone frequency to fundamental acoustic frequency. After iteration — assuming a relationship, calculating a spectrum, and comparing with spectra in the database — the following relation was defined for wave damping:

$$d_w = \left(1 - \frac{f_e}{f_L}\right)^2 + \left(1 - \frac{f_e}{f_W}\right)^2 + \left(1 - \frac{f_e}{f_D}\right)^2$$

Finally, the equation for damping ratio is assumed to be an empirically determined combination of viscous and wave contributions that is unique for each mode and Mach number:

$$m = 1, d = d_w e^{d_w} (0.006617 M_\infty + 0.0003734)$$

$$m = 2, d = d_w e^{d_w} (0.01284 M_\infty - 0.005529)$$

$$m = 3, d = d_w e^{d_w} (0.006617 M_\infty + 0.0003734)$$

$$m = 4, d = d_w e^{d_w} (2.837 M_\infty - 1.691)$$

$$m = 5, d = d_w e^{d_w} (2.845 M_\infty - 1.7047)$$

$$m \geq 6, d = d_w e^{d_w} (0.996 M_\infty - 0.5954)$$

In each case, if the value calculated is $d < 0$, then the damping ratio is set equal to the viscous term, i.e., if $d < 0$, then $d = d_\mu$.

Note: The equations and constants listed here were selected to provide the best match of predictions and available experimental data at $M_\infty = 0.60$ and $M_\infty = 0.95$, and are therefore strictly appropriate only for $M_\infty \leq 0.95$.

It is not certain that acoustic theory can be used to predict the wave damping, since the coupling of acoustic and fluid mechanic phenomena are not addressed in acoustic theory. The necessary coupling probably can be represented only with complete Navier-Stokes equations.

2.3.6 Maximum rms Wall Pressure

It is clear from the centerline pressure distributions recorded during the experiments that the maximum pressures in the cavity occur on the downstream wall near the opening of the cavity, where the turbulent mixing zone impinges (Fig. 1). An equation for estimating the rms pressure in a turbulent mixing zone can be derived from Bernoulli's equation,

$$dP + \rho\, u\, du = 0$$

It is proposed that the rates of change of pressure, dP, and velocity, du, be treated as fluctuations attributable to turbulence. Then the rms of Bernoulli's equation is

$$P_{rms} = \bar{\rho}\, \bar{u}\, u_{rms}$$

where the quantities $\bar{\rho}$ and $\bar{u}$ represent the mean values of density and velocity at the wall, respectively.

The turbulent kinetic energy is

$$\tau_{KE} = \frac{u^2_{rms}}{2}$$

so that

$$P_{rms} = \bar{\varrho}\,\bar{u}\,\sqrt{2\,\tau_{KE}}$$

It is common to assume that a linear relationship exists between the Reynolds shear and the turbulent kinetic energy, so that the shear force may be defined as

$$F_s = a_1\,\bar{\varrho}\,\tau_{KE}$$

with a corresponding friction coefficient of

$$C_f = \frac{F_s}{q_\infty}$$

Substituting in the P_{rms} equation for τ_{KE} in terms of C_f produces

$$P_{rms} = \bar{u}\sqrt{\frac{2\,\bar{\varrho}\,q_\infty\,C_f}{a_1}}$$

This equation has been applied successfully to a boundary layer, and is assumed to apply to a turbulent mixing zone as well. Note that the values of $\bar{\varrho}$, $\bar{u}$, and C_f for a turbulent mixing zone must be evaluated along the dividing streamline. Recalling that the free-stream Crocco number is defined from the energy equation as

$$C^2_\infty = \frac{V^2_\infty}{2\,c_p\,T_t}$$

then the equation for the rms pressure in a turbulent mixing zone becomes

$$\frac{P_{rms}}{q_\infty} = 2\,\phi_d\sqrt{\frac{(1 - C^2_\infty)\,C_f}{a_1\,[1 - (C_\infty\,\phi_d)^2]}}$$

A method presented by Bauer in Ref. 25 is used to determine the friction coefficient, C_f, along the dividing streamline. It is asserted that the momentum of the entrained mass flow must equal the total shear force along the dividing streamline. The equation for C_f for the case of no initial boundary layer is

$$C_f = 2 \frac{(1 - C_\infty^2)\, I_d}{\sigma}$$

where I_d represents the normalized momentum of the entrained mass flow, and can be determined from curves fit to the theoretical values offered by Bauer in Ref. 25. The curve fits are

$$\text{for} \quad M_\infty \leq 0.5, \quad I_d = 0.15$$

and

$$\text{for} \quad M_\infty > 0.5, \quad I_d = 0.0338\, M_\infty + 0.15$$

Provision for a nonzero initial boundary layer can be made by applying the experimental result that the value of C_f in a fully developed mixing zone is an order of magnitude greater than C_f in a corresponding boundary layer. An appropriate correction factor can be posed in terms of η_p, the mixing position parameter determined by Bauer in Ref. 27. Hence, C_f for a nonzero initial boundary layer can be calculated from

$$C_f = 2 \frac{(1 - C_\infty^2)\, I_d}{\sigma} (0.9\, e^{-5\eta_p} + 0.1)$$

2.3.7 Spectra Reference Pressure

The absolute level of the pressure spectrum is determined by the strength of the vortices produced by the acoustic waves generated in the turbulent mixing zone. The reference pressure, P_{ref}, is defined to be the strength of the vortices, and is assumed to be the same for all frequencies. Since the overall rms pressure is determined by turbulent mixing (Section 2.3.6), then the reference pressure is

$$P_{ref} = \frac{P_{rms}}{\sqrt{\sum_{n=1}^{512} \frac{a_n^2}{2}}}$$

3.0 COMPARISON OF PREDICTIONS WITH DATA

3.1 THE CAP CODE

Equations comprising the model described previously were compiled into a code named the Cavity Acoustic Prediction Code (CAP Code). Only approximately 200 lines of BASIC® code were needed for installation on a personal computer of modest capacity and calculation speed. Run times of 10 sec or less were routine. (A listing of the code is not included, since the equations are simple algebraic and exponential expressions, and potential users will need to write code using commands unique to the selected computer.)

3.2 RESULTS — NO MASS INJECTION

3.2.1 Effect of Cavity L/D Ratio

CAP Code predictions of spectra of sound pressure level (SPL) in the frequency range of 0 to 5,000 Hz are compared with experimental data in Figs. 10 and 11. Although the damping terms were optimized for the range $M_\infty \leq 0.95$, predictions for the L/D = 4.5 cavity are illustrated in Fig. 10 for a range of Mach numbers from 0.6 to 5.0. It is clear that spectra predicted using the CAP Code model are in good agreement with the experimental data for subsonic and transonic Mach numbers, i.e., the conditions for which the damping function was optimized. Frequencies of the detected tones are predicted very well. Although tonal amplitudes are not in perfect agreement with data in all cases, the overall rms pressure, illustrated as Overall Sound Pressure Level (OASPL), is in good agreement at the optimum subsonic and transonic conditions.

Predictions and data for a cavity of L/D = 9.0 are illustrated in Fig. 11. Because of the transitional nature of the aeroacoustic flow field in the L/D = 9.0 cavity (Appendix A), there are no detected tones at $M_\infty = 0.60$ and only very weak tones at any Mach number. When tones are detectable, the frequencies are predicted well, using the Rossiter equation that is built into the CAP Code. Note that the predicted overall rms is in good agreement with data at all Mach numbers, despite the inaccuracies of the CAP Code spectral peak amplitudes.

The failure of the CAP Code to predict accurately the spectral amplitudes may be attributed to an inaccurate damping ratio, d. (The damping ratio serves to limit amplitudes at frequencies between the edgetone frequencies through the f/f_e terms of the response coefficient, R_s.) As yet, there is no explicit theoretical basis for combining the postulated viscous- and wave-damping contributions to create an effective damping ratio. The effective damping ratios described in Section 2.3.5 are purely empirical for each mode and Mach number.

Since the data were recorded at several different values of total pressure, the use of spectral, or logarithmic, graphs can be misleading. An alternate method of presenting the data is through the parameter P_{rms}/q_∞. The overall sound pressure level (OASPL) is illustrated in both ways in Fig. 12 for the L/D = 4.5 cavity, and in Fig. 13 for the L/D = 9.0 cavity. Although the OASPL predicted using the CAP Code seems in good agreement with the data, more serious discrepancies appear when the rms pressure is normalized by free-stream dynamic pressure. At the present stage of code development, the only explanation that can be offered is the empirical nature of the turbulent mixing similarity parameter, σ.

3.2.2 Effect of Cavity Size

Two sizes of cavity were used, providing a limited opportunity to investigate cavity size effects. The basic cavity model was 18 by 4 by 4 in. (Fig. A-1), but by using the U-block insert, a half-size cavity of 9 by 2 by 2 in. was created (Fig. A-2). Two comparisons of CAP Code and test data were possible, one with the U-block installed with the open end downstream, and one with the U-block installed with the open end upstream. In the former case, it was possible to use the same transducer, K18, as a criterion, just as for the full-size 18-in. cavity, but the approaching boundary layer was thicker than for the 18-in. cavity. In the latter case, the approaching boundary layer was the same as for the full-size 18-in. cavity, but the K18 transducer was covered, forcing the use of transducer K12 (which was partially covered by the U-block) as a criterion. Not surprisingly, predictions and measured spectra for the half-size cavity were in only fair agreement (Figs. 14 and 15).

The different boundary layer and transducer are probable reasons for the poor agreement. With the open end of the U-block downstream, estimates of the boundary layer were made on the basis of a turbulent, $1/7^{th}$-power velocity profile. The predicted frequencies were shifted, probably, because of the lack of knowledge of the approaching boundary layer and the corresponding uncertainty of the correct value of the turbulent mixing parameter, η_p (Section 2.3.2.2). In the case of the open end upstream, for which transducer K12 was used, both the frequencies and the overall amplitudes were in better agreement, since the approaching boundary layer was the same as for the full-size cavity. (Amplitude agreement may be fortuitous, however, since it is known that amplitudes vary with location in the cavity, especially between sites at the bottom and top of the downstream wall. Differences of 3 or 4 dB have been measured, Ref. 17).

3.2.3 Boundary-Layer Influence

As implied in Section 3.2.1, the degree of correlation between CAP Code predictions and data is strongly dependent on the initial boundary layer (at the upstream edge of the cavity). A further indication is illustrated by the two CAP Code curves of Figs. 12 and 13. One curve was predicted on the assumption of a zero boundary-layer height, whereas for the other, a boundary-layer height based on experimental values was assumed. Only a few measurements of the boundary layer were made during the experiments, and then only at the supersonic Mach numbers 2.50, 3.51, and 5.04, and with a trip grit applied near the leading edge of the plate (Appendix A). On the basis of these data, a turbulent boundary layer was assumed, with a $1/7^{th}$-power velocity profile. Estimates of boundary-layer height for subsonic approach flows were made by beginning with the SWIM code (Ref. 31), then applying adjustments to match data by Tucker (Ref. 30). The final values are illustrated in Fig. 16.

It is clear from Figs. 12 and 13 and from the conditions contributing to the results illustrated in Figs. 14 and 15 that the approaching boundary-layer characteristics exert a strong influence on the CAP Code predictions. In fact, most schemes for alleviating or suppressing cavity acoustics involve interacting with the approaching flow (e.g., spoilers). In the CAP Code, the influence is exerted primarily through the model assumed for the turbulent mixing position parameter, η_p (Section 2.3.2.2).

3.3 RESULTS — WITH MASS INJECTION

Another technique of acoustic suppression involves the injection of fluid, either into the boundary layer upstream of the cavity, or directly into the cavity, or through any of various other injection schemes. The intent is to interact with the turbulent mixing zone, stabilizing it or deflecting it away from impact with the downstream wall. One such technique, by Vakili and Gauthier at the UTSI, is described in Ref. 29. Fluid mass is injected through a pattern of holes in the plate upstream of the cavity, altering the approaching boundary layer and reducing the OASPL. A secondary effect is to change the frequency of vortex separation from the cavity edge, so that the edgetones become different from the natural frequencies of the cavity.

A prediction of the upstream injection case was made using the CAP Code. Although Vakili and Gauthier did not present a spectrum for comparison, it was possible to calculate an overall SPL with the effect of mass injection included. The results were gratifying in that the trend was matched, as illustrated in Fig. 17, despite having little information concerning boundary-layer profile or temperature of the injected mass flow.

4.0 CONCLUDING REMARKS

An analytical technique was developed to provide predictions of both the frequency and amplitude, i.e. the spectra, of acoustic tones in smooth-surfaced, rectangular cavities exposed to a grazing external flow. Equations were compiled in a small code (designated the Cavity Acoustic Prediction Code, or CAP Code), intended to produce solutions in less than 15 sec on a personal computer of modest capability. An existing empirical technique of predicting the edgetone frequencies of a rectangular cavity, the modified Rossiter equation, was used for predictions of the frequencies of tones in a cavity. Amplitudes were predicted by considering the flow passing over the cavity to be a single-stream turbulent mixing zone, with the maximum wall pressure defined as a function of the rms kinetic energy in the turbulent mixing zone along the dividing streamline. Characteristics of the approaching boundary layer were included through the use of the turbulent mixing similarity parameter. An empirical damping concept was developed as a function of the ratio of a specific frequency to the edgetone frequencies. Comparisons of CAP Code predictions with a large database were made, with the following observations:

1. Good correlation was noted between predictions and data for SPL spectra and overall SPL in a moderately deep cavity (L/D = 4.5) at $M_\infty < 1.50$. Correlation with spectral data was weak in the supersonic regime, since the empirical damping constants that were used were selected for optimum agreement in the transonic regime. Similar results were noted for a transitional cavity of L/D = 9.0.

2. Apparent effects of cavity size on the accuracy of CAP Code amplitude predictions were noted, but the few data points available for comparison prevented establishing limits on the use of the CAP Code for scaling results. Controlled experiments should be completed in which approaching boundary layer is scaled to the cavity length — probably through momentum thickness. Future investigations should include documentation of the characteristics of the approaching boundary layer.

3. It was also possible to use the CAP Code to predict spectra and overall SPL for a case of mass-injection into the approaching boundary layer. Again, good correlation of the overall SPL was observed with the limited data available.

4. Although the fundamental concepts seem valid, additional study is needed to refine the damping terms in the code. The strong dependence of the CAP Code on knowledge of the approaching boundary-layer profile suggests that additional boundary-layer data should be obtained. Additional data are also needed for further validation and extension to cases of mass-injection into the cavity proper, to cavities of different scale, and to complex cavities, such as nonrectangular cavities and cavities with mechanical spoilers.

REFERENCES

1. Covert, Eugene E. "An Approximate Calculation of the Onset Velocity of Cavity Oscillations." *AIAA Journal*, Vol. 8, No. 12, December 1970, pp. 2189-2194.

2. Krishnamurty, K. "Acoustic Radiation from Two-Dimensional Rectangular Cutouts in Aerodynamic Surfaces." NACA TN 3487, August 1955.

3. Roshko, Anatol. "Some Measurements of Flow in a Rectangular Cutout." NACA TN 3488, August 1955.

4. Plumblee, H. E., Gibson, J. S., and Lassiter, L. W. "A Theoretical and Experimental Investigation of the Acoustic Response of Cavities in an Aerodynamic Flow." WADD-TR-61-75 (AD-277803), March 1962.

5. Rossiter, J. E. "Wind Tunnel Experiments on the Flow Over Rectangular Cavities at Subsonic and Transonic Speeds." Ministry of Aviation, Aeronautical Research Council, Reports and Memoranda No. 3438, October 1964.

6. East, L. F. "Aerodynamically Induced Resonance in Rectangular Cavities." *Journal of Sound and Vibration,* Vol. 3, No. 3, 1966, pp. 277-287.

7. Heller, H. H., Holmes, G., and Covert, E. "Flow-Induced Pressure Oscillations in Shallow Cavities." AFFDL-TR-70-104 (AD-880496), December 1970.

8. Smith, D. L., and Shaw, L. L. "Prediction of the Pressure Oscillations in Cavities Exposed to Aerodynamic Flow." AFFDL-TR-75-34 (AD-A018518), October 1975.

9. Bilani, A. J., and Covert, E. E. "Estimates of Possible Excitation Frequencies for Shallow Cavities." *AIAA Journal,* Vol. 11, No. 3, March 1973, pp. 347-351.

10. Tam, C. K. W. and Block, P. J. W. "On the Tones and Pressure Oscillations Induced by Flow Over Rectangular Cavities." *Journal of Fluid Mechanics,* Vol. 89, November 1978.

11. Clark, Rodney L. "Evaluation of F-111 Weapon Bay Aeroacoustic and Weapon Separation Improvement Techniques." AFFDL-TR-79-3003 (AD-A070253), February 1979.

12. Bartel, H. W. and McAvoy, J. M. "Cavity Oscillation in Cruise Missile Carrier Aircraft." AFWAL-TR-81-3036, June 1981.

13. Kaufman, Louis G., II, Maciulaitus, Algirdas, and Clark, Rodney. L. "Mach 0.6 to 3.0 Flows Over Rectangular Cavities." AFWAL-TR-82-3112 (AD-A134579), May 1983.

14. Blair, A. B., Jr., and Stallings, Robert L., Jr. "Supersonic Axial-Force Characteristics of a Rectangular-Box Cavity With Various Length-to-Depth Ratios in a Flat Plate." NASA-TM-87659, December 1986.

15. Stallings, R. L., Jr. and Wilcox, F. J., Jr. "Experimental Cavity Pressure Distributions at Supersonic Speeds." NASA-TP-2683 (N87-22626), June 1987.

16. Plentovich, E. B. "Three-Dimensional Cavity Flow Fields at Subsonic and Transonic Speeds." NASA Technical Memorandum 4209, September 1990.

17. Dix, R. E. "On Simulation Techniques for the Separation of Stores from Internal Installations." SAE Technical Paper Series, No. 871799, Presented at the SAE Aerospace Technology Conference and Exposition, Long Beach, California, October 5-8, 1987.

18. Om, Deepak. "Navier-Stokes Simulation for Flow Past an Open Cavity." AIAA-86-2628, October 1986.

19. Baysal, O. and Stallings, R. L., Jr. "Computational and Experimental Investigation of Cavity Flow Fields." AIAA-87-0114, January 1987.

20. Rizzeta, D. P. "Numerical Simulation of Supersonic Flow Over a Three-Dimensional Cavity." AIAA-87-1288, June 1987.

21. Suhs, N. E. "Computations of Three-Dimensional Cavity Flow at Subsonic and Supersonic Mach Numbers." AIAA-87-1208, June 1987.

22. Baysal, Oktay, Srinivasan, Shivakumar, and Stallings, R. L., Jr. "Unsteady Viscous Calculations of Supersonic Flows Past Deep and Shallow Three-Dimensional Cavities." AIAA-88-0101, January 1988.

23. Dougherty, N. S. et al. "Time-Accurate Navier-Stokes Computations of Self-Excited Two-Dimensional Unsteady Cavity Flows." AIAA-90-0691, January 1990.

24. Dobson, T. W., Jr. "Discrete Frequency Acoustics Correlation for Rectangular Cavities Exposed to High-Speed Flows." University of Tennessee Space Institute Thesis, December 1990.

25. Bauer, R. C. "Characteristics of Axisymmetric and Two-Dimensional Isoenergetic Jet Mixing Zones." AEDC-TDR-63-253, December 1963.

26. Bauer, R. C., and Matz, R. J. "Influence of Initial Boundary Layer on the Two-Dimensional Turbulent Mixing of a Single Stream." AEDC-TR-71-79, April 1971.

27. Bauer, R. C. "An Analysis of Two-Dimensional Laminar and Turbulent Compressible Mixing." *AIAA Journal*, Vol. 4, No. 3, March 1966, pp. 392-395.

28. Bauer, R. C. "Another Estimate of the Similarity Parameter for Turbulent Mixing." *AIAA Journal*, Vol. 6, No. 5, May 1968, pp. 925-927.

29. Vakili, Ahmad D. and Gauthier, Christian. "Control of Cavity Flow by Upstream Mass Injection." AIAA-91-1645, June 1991.

30. Tucker, Maurice. "Approximate Turbulent Boundary-Layer Development in Plane Compressible Flow Along Thermally Insulated Surfaces with Application to Supersonic-Tunnel Contour Correction." NACA TN 2045, March 1950.

31. Whitfield, D. L. "Integral Solution of Compressible Turbulent Boundary Layers Using Improved Velocity Profiles." AEDC-TR-78-42 (AD-A062946), December 1978.

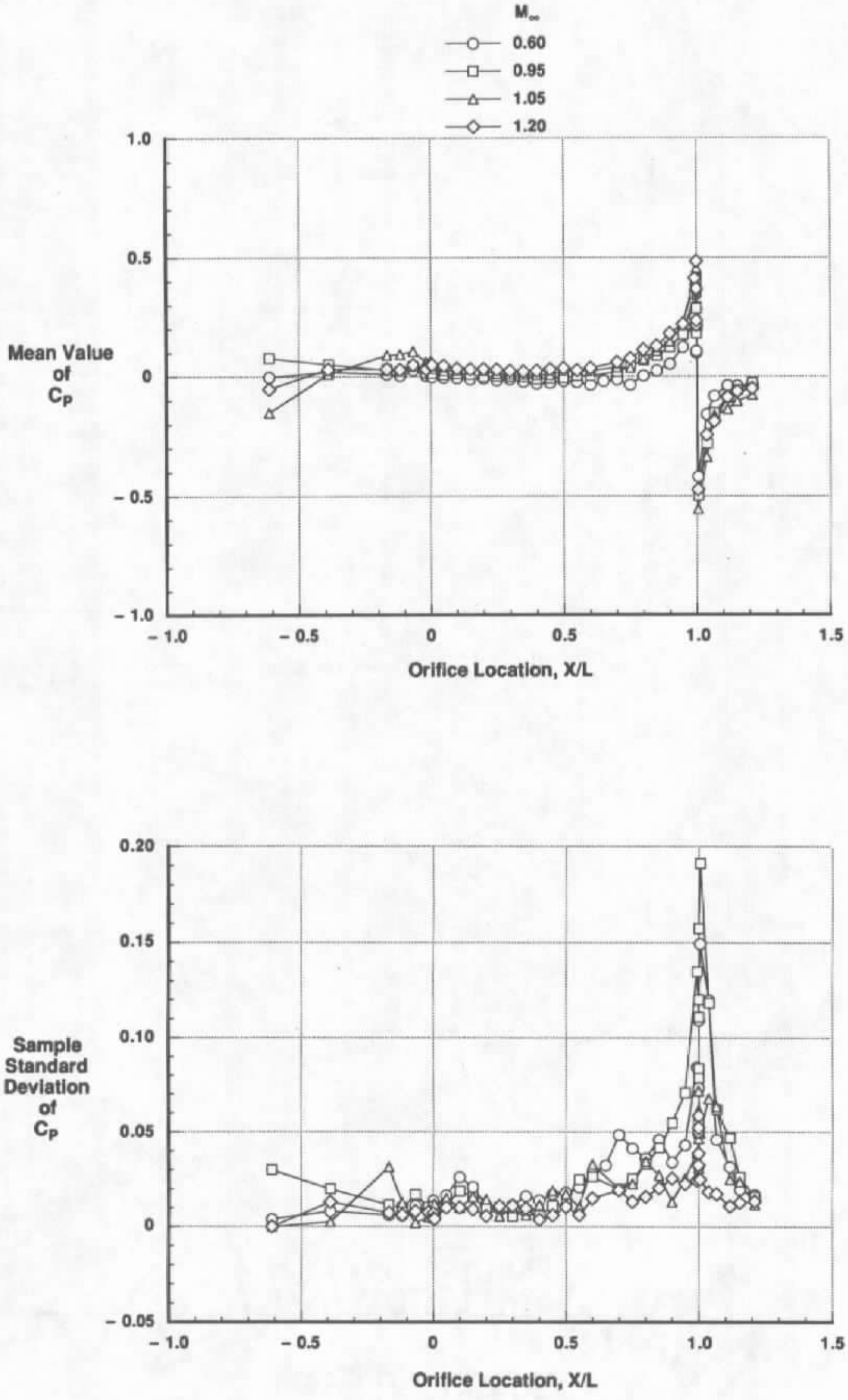

a. Deep cavity (L/D = 4.5)

Figure 1. Centerline distribution of surface pressures — mean value and standard deviation.

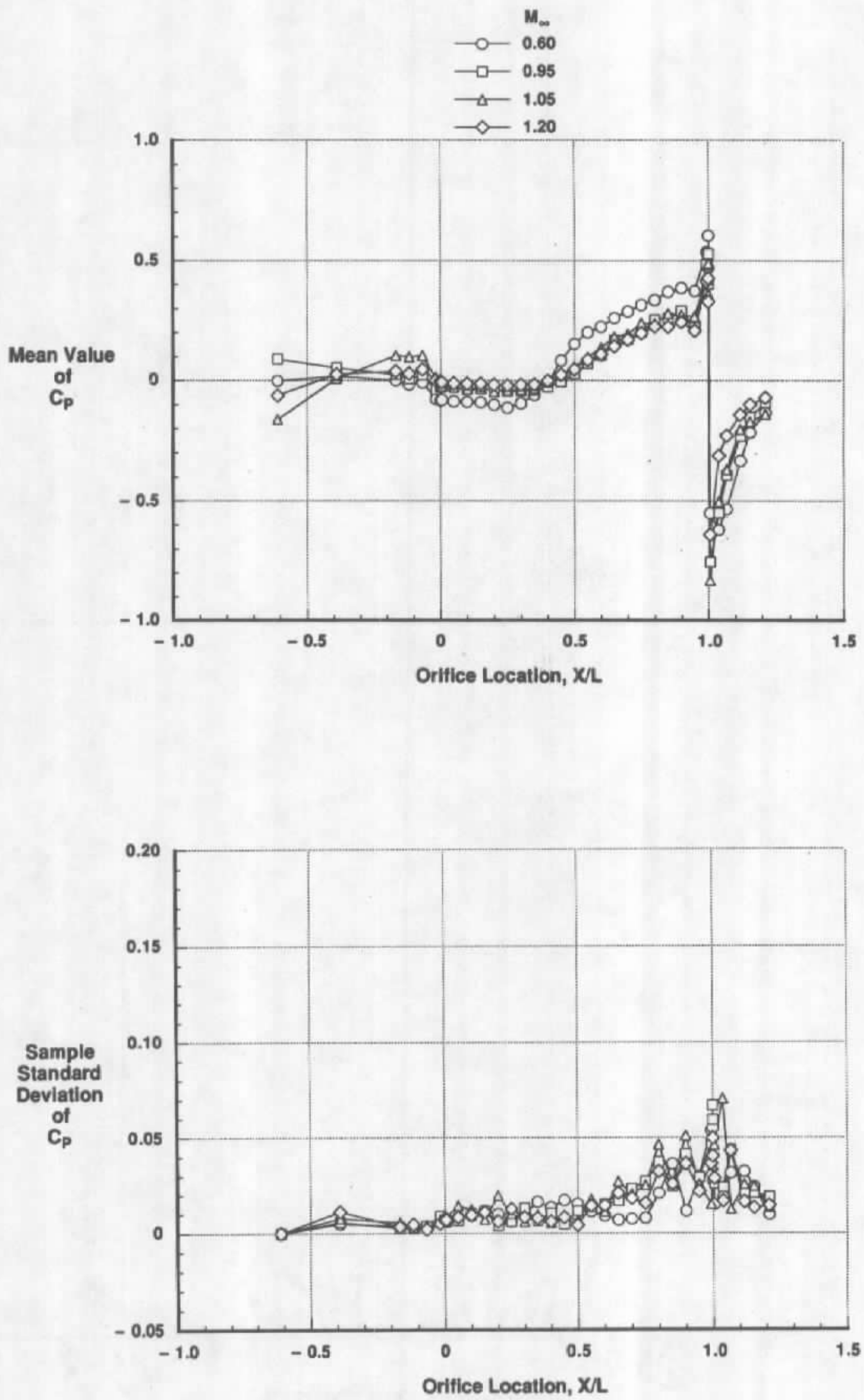

b. Transitional cavity (L/D = 9.0)
Figure 1. Continued.

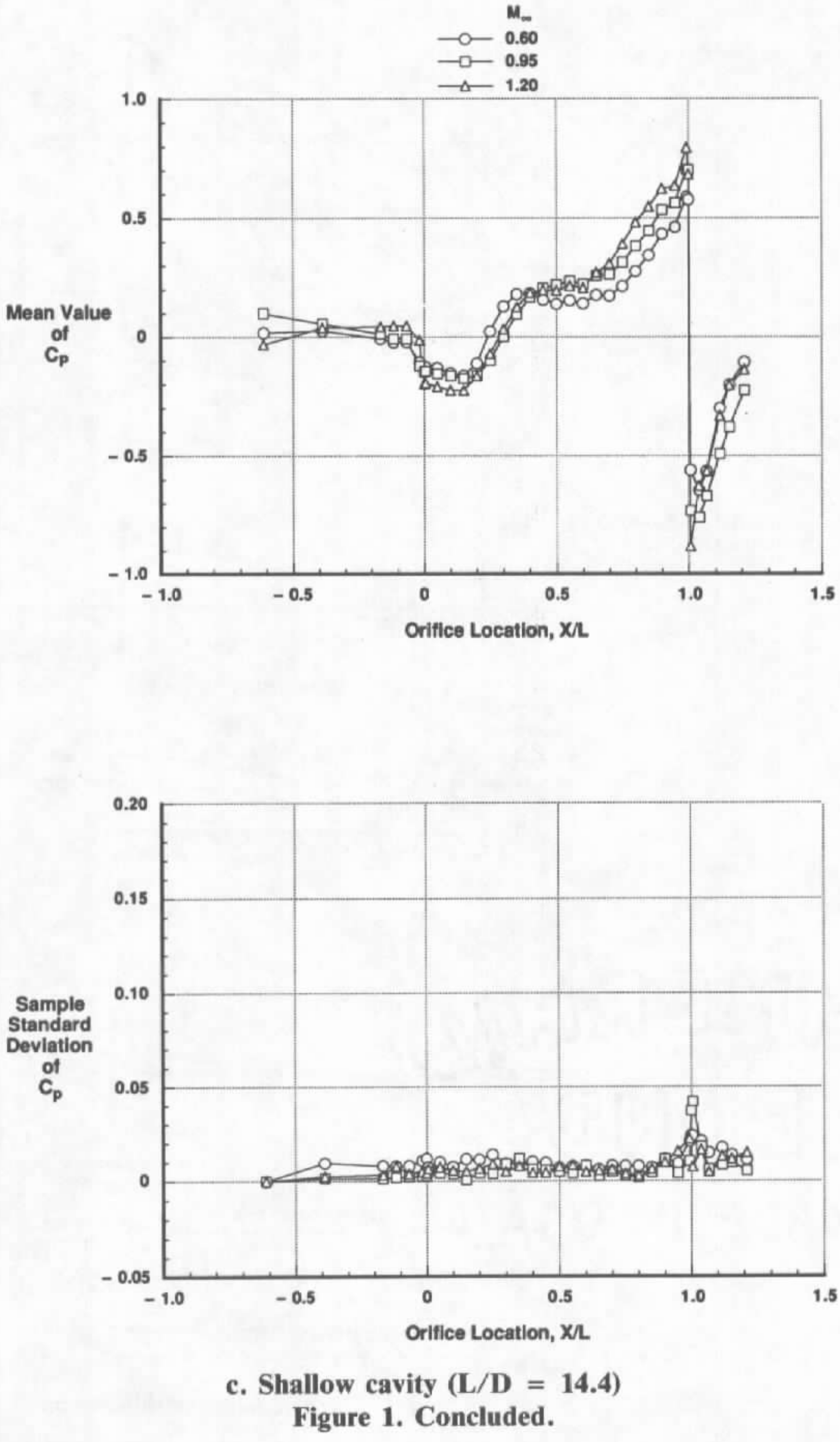

c. Shallow cavity (L/D = 14.4)
Figure 1. Concluded.

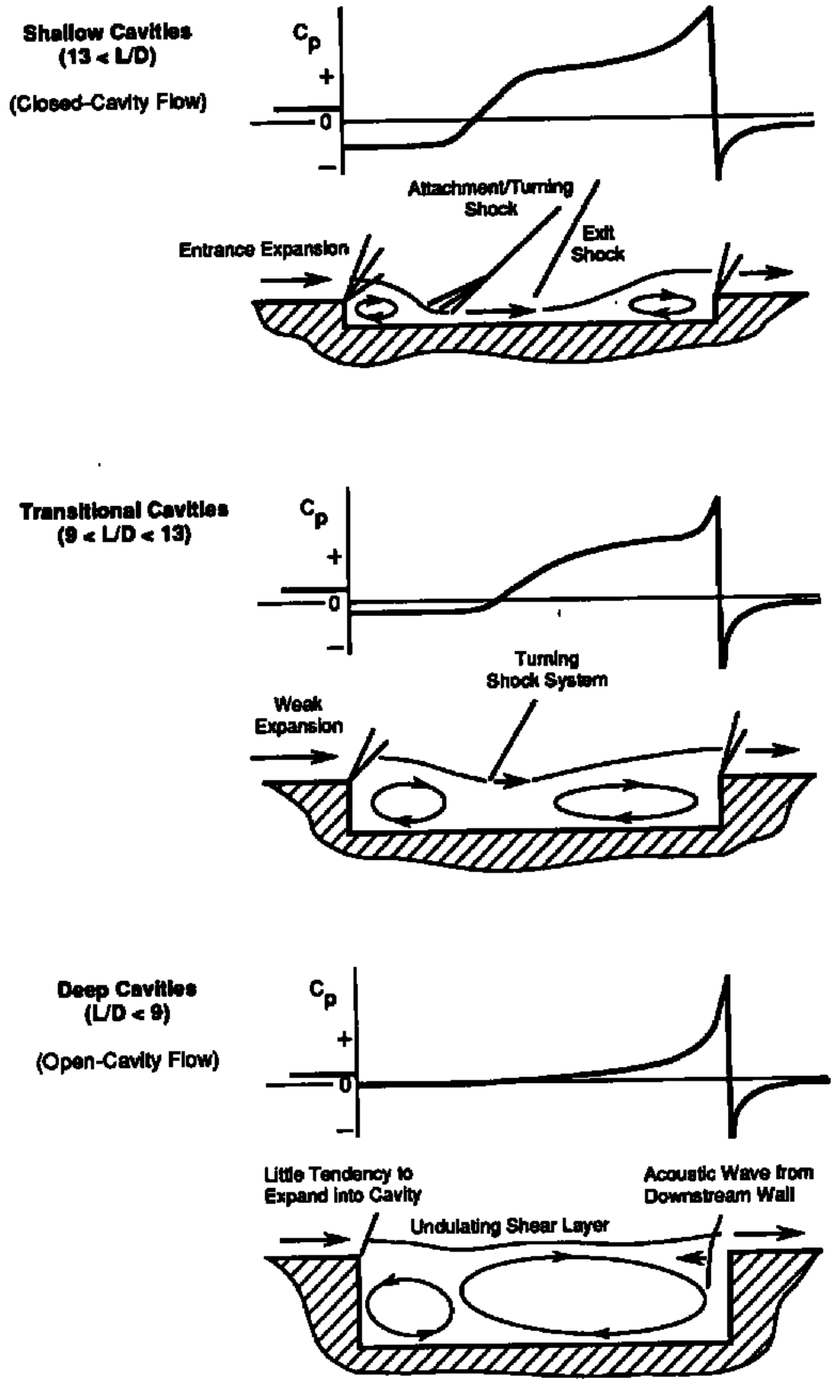

Figure 2. Qualitative model of cavity flow for supersonic approach flow.

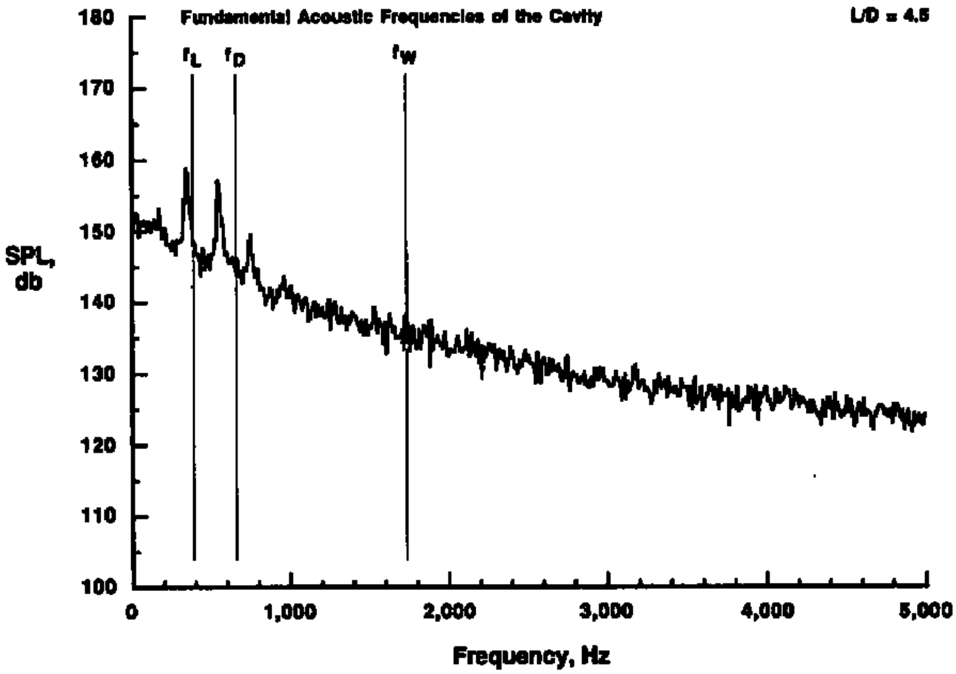

a. M_∞ = 0.60

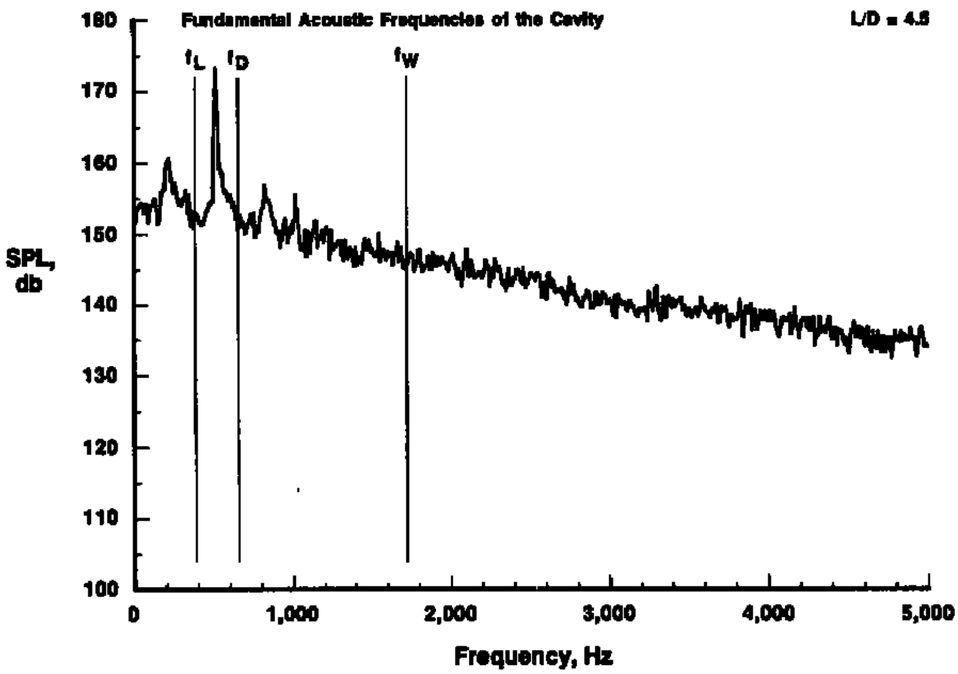

b. M_∞ = 1.20

Figure 3. Typical cavity pressure spectra and fundamental acoustic modes, L/D = 4.5.

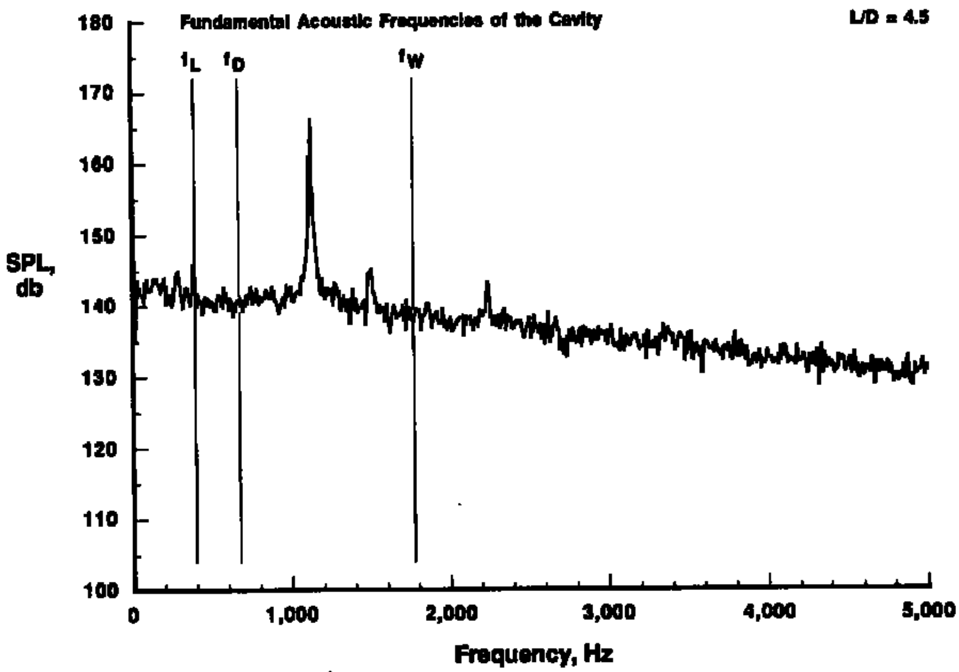

c. M_∞ = 2.75

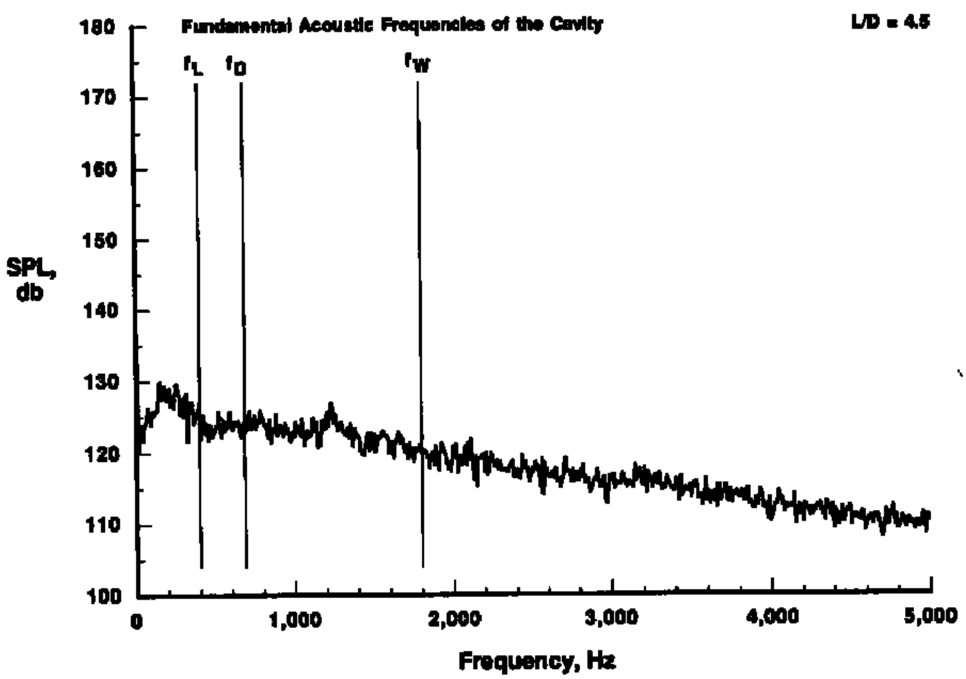

d. M_∞ = 5.04

Figure 3. Concluded.

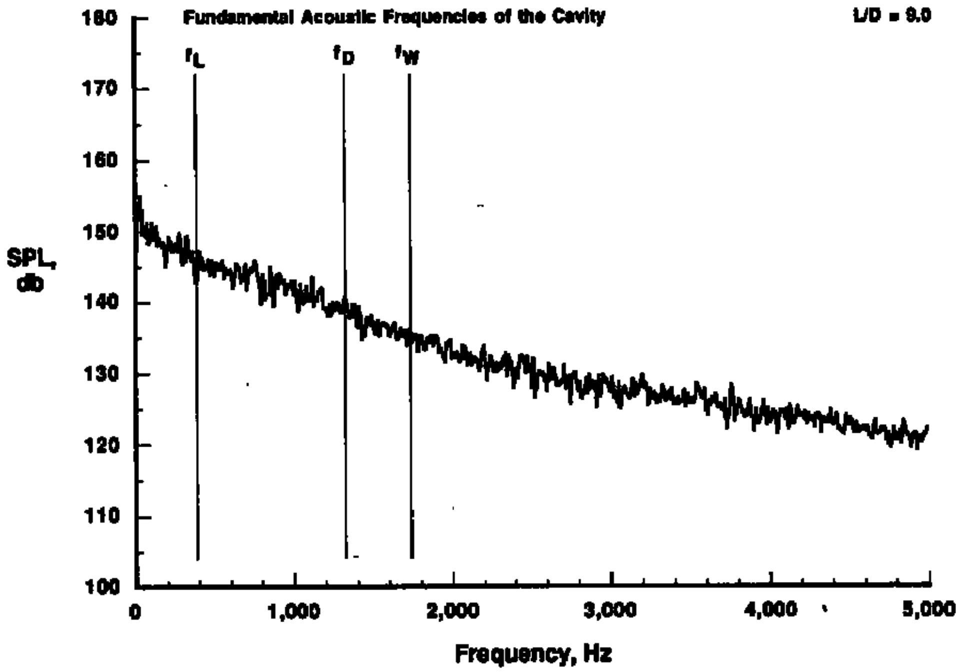

a. $M_\infty = 0.60$

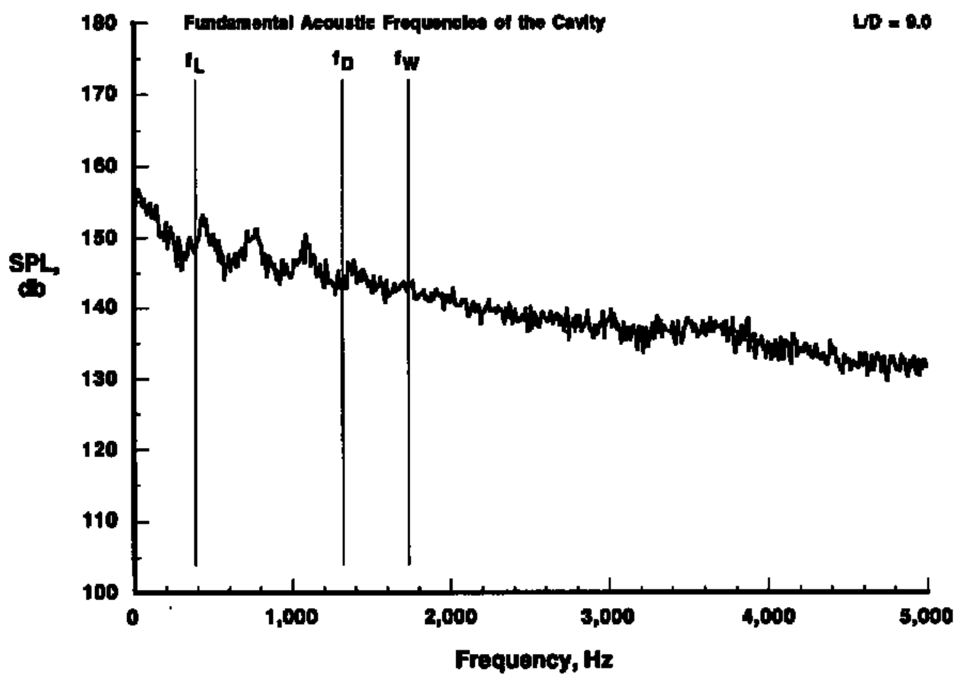

b. $M_\infty = 1.20$

Figure 4. Typical cavity pressure spectra and fundamental acoustic modes, L/D = 9.0.

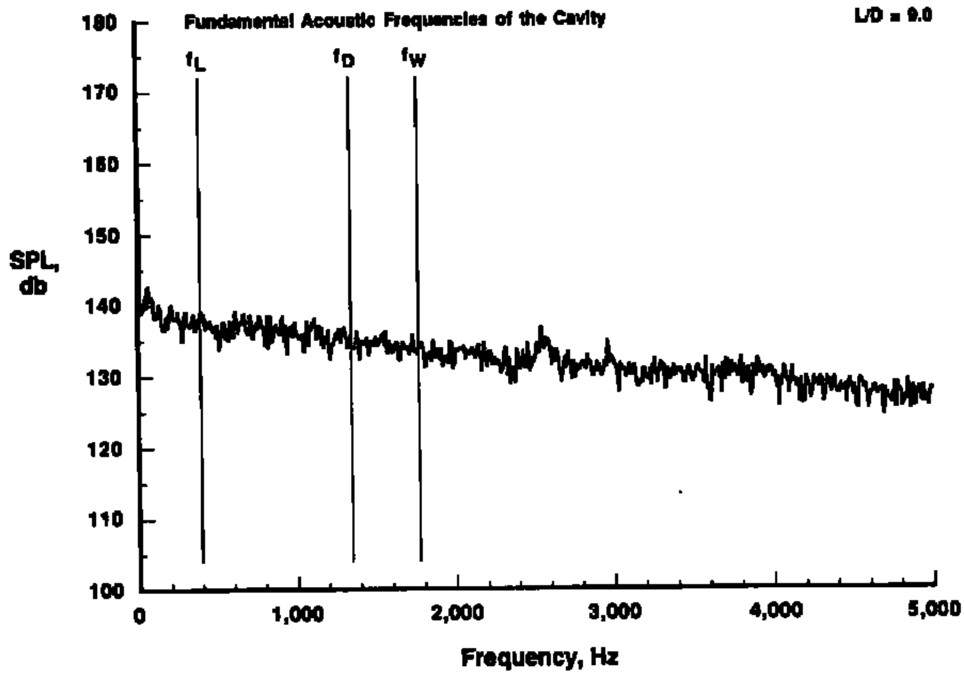

c. $M_\infty = 2.75$

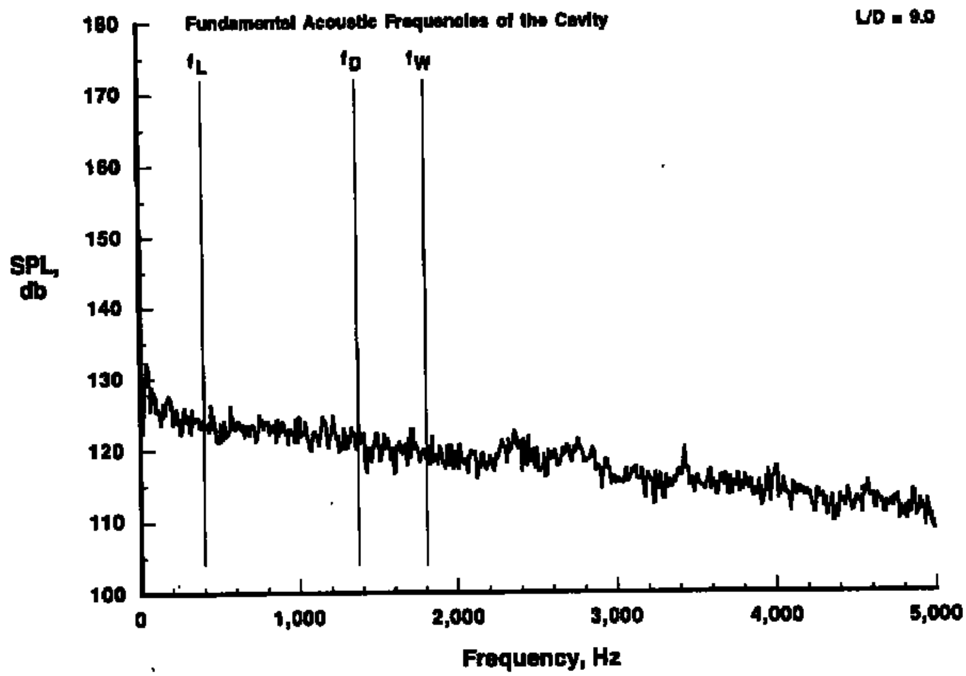

d. $M_\infty = 5.04$

Figure 4. Concluded.

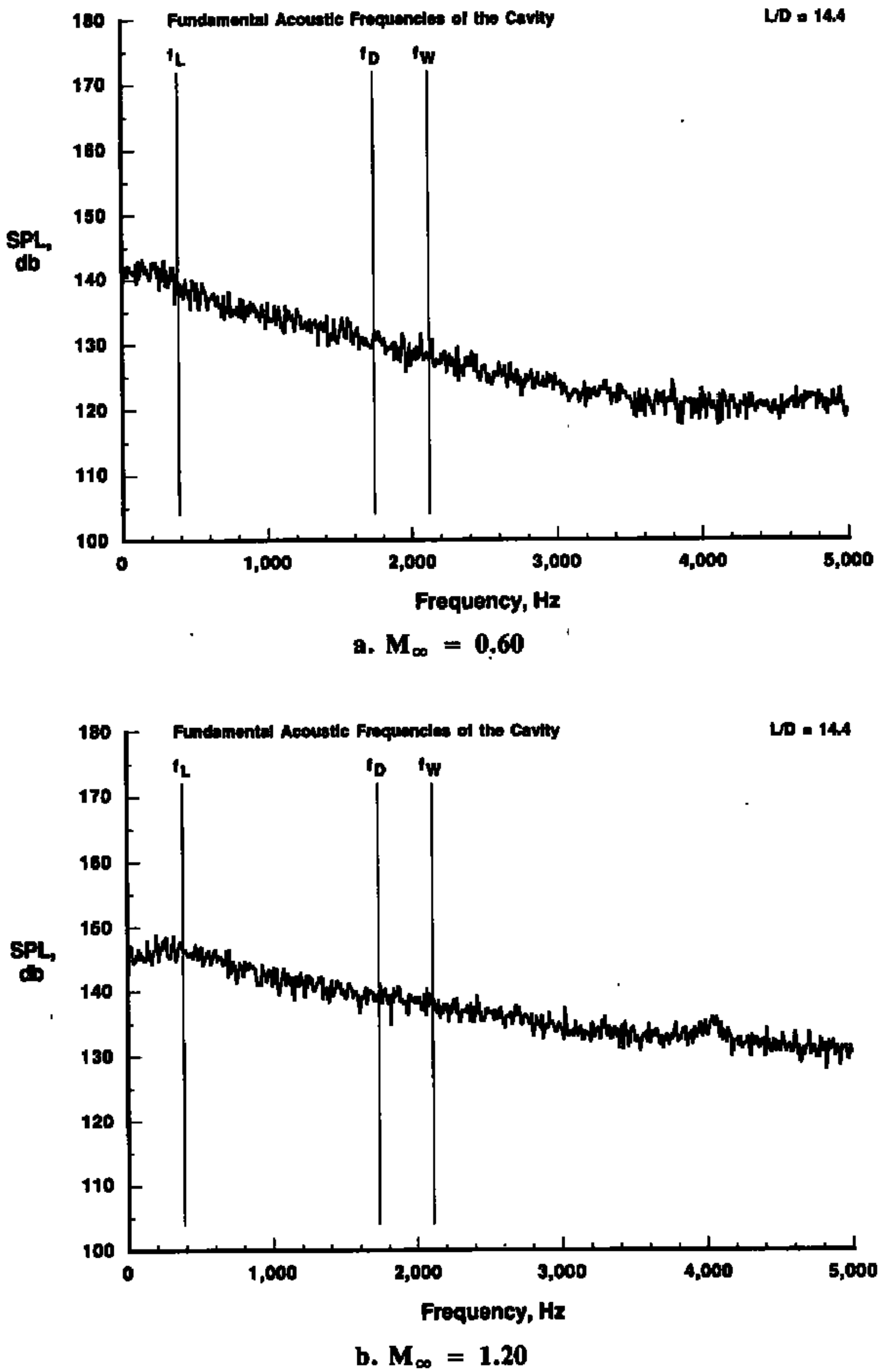

Figure 5. Typical cavity pressure spectra and fundamental acoustic modes, L/D = 14.4.

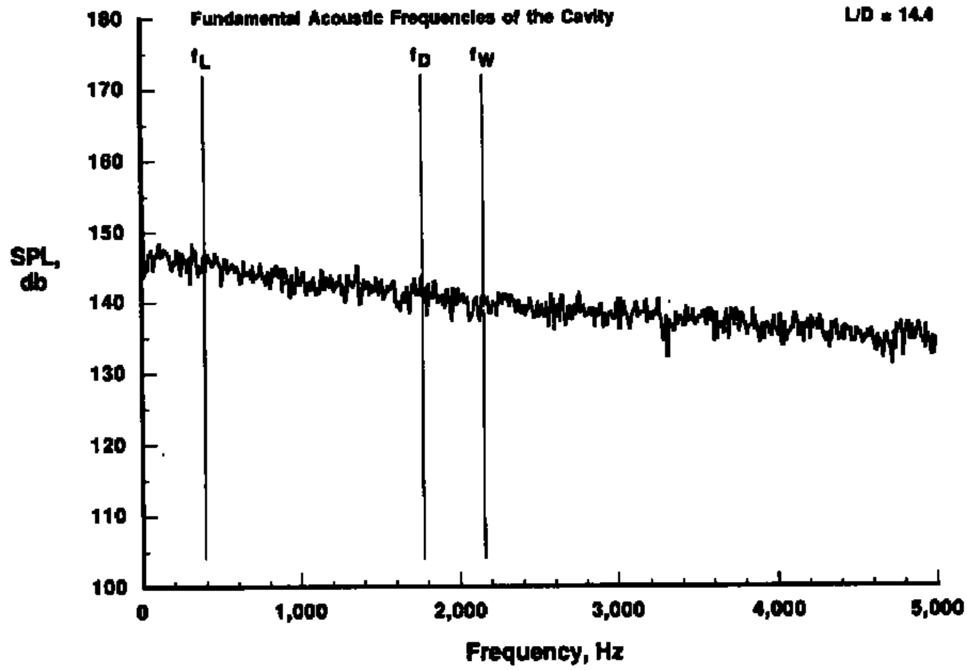

c. M_∞ = 2.75

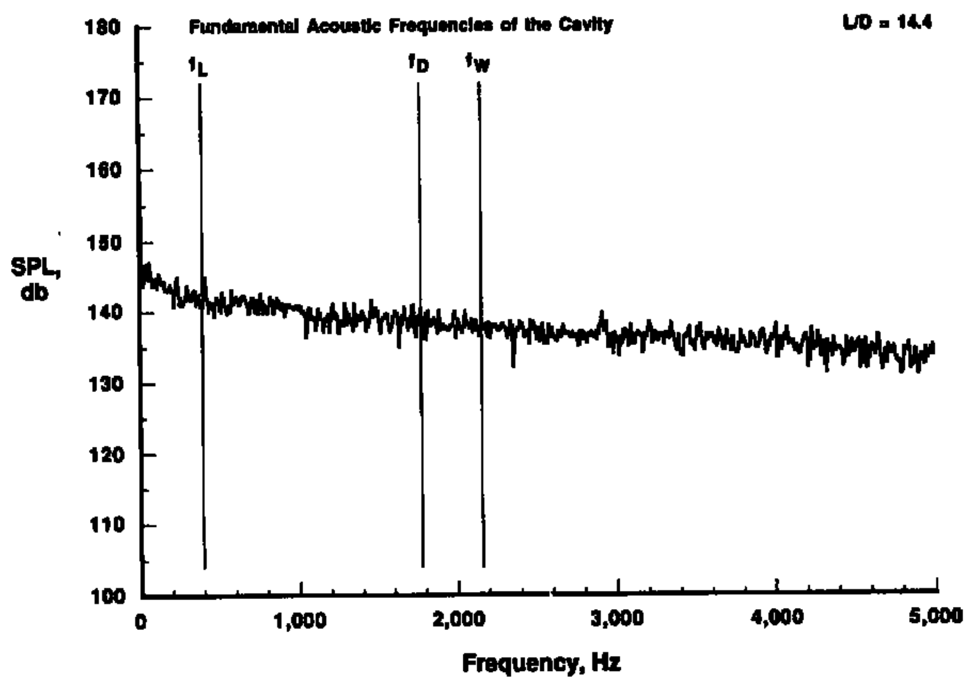

d. M_∞ = 5.04

Figure 5. Concluded.

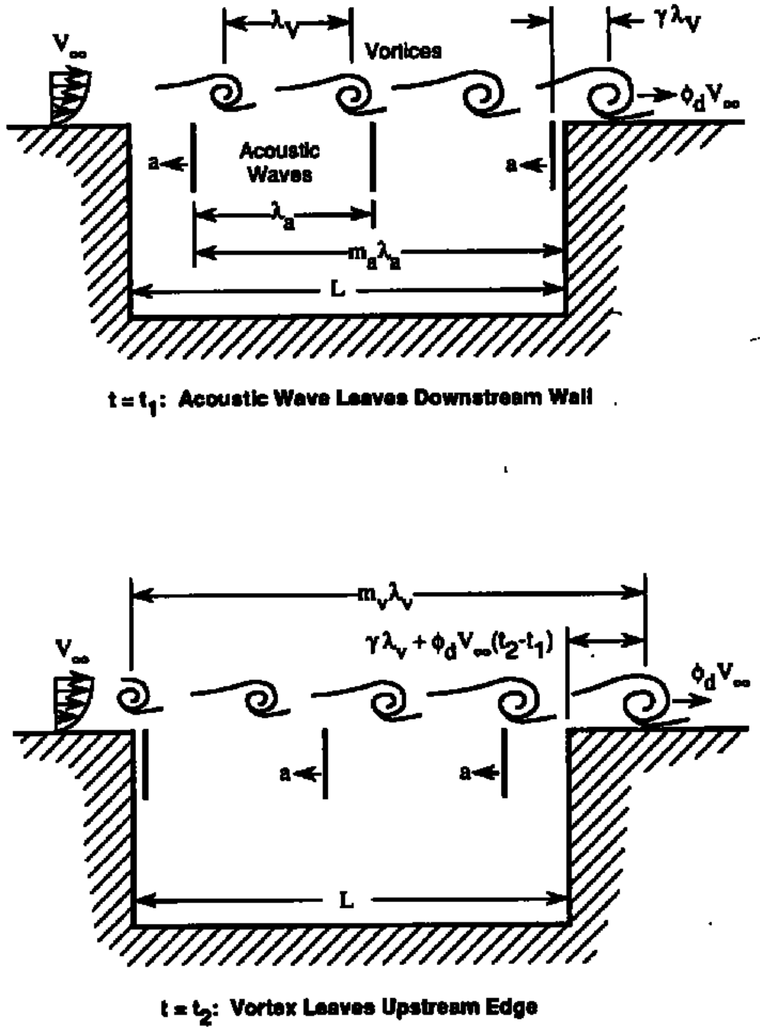

Figure 6. Model of cavity acoustic generation.

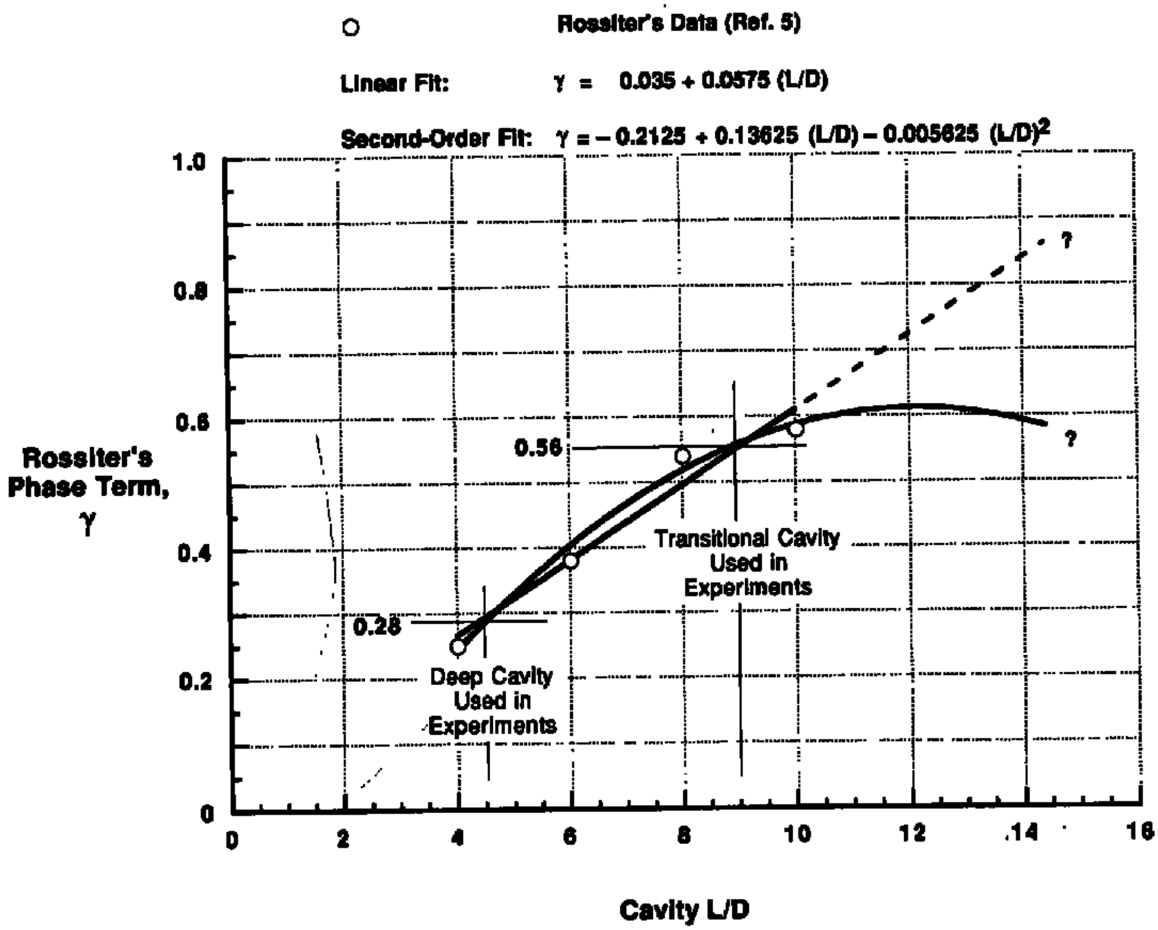

Figure 7. Variation of Rossiter's phase term, γ, with cavity L/D.

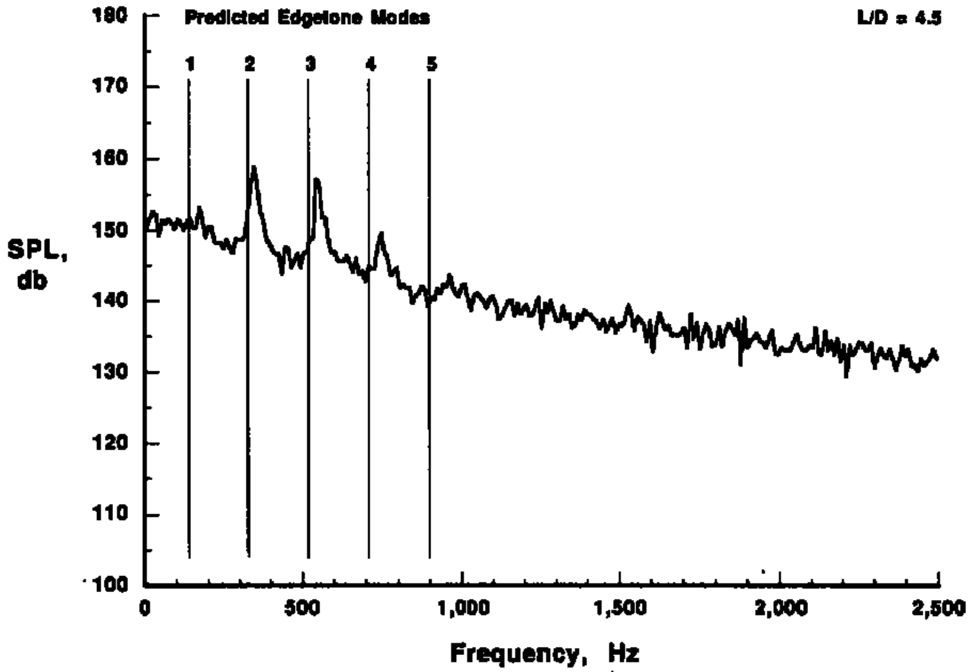

a. M_∞ = 0.60

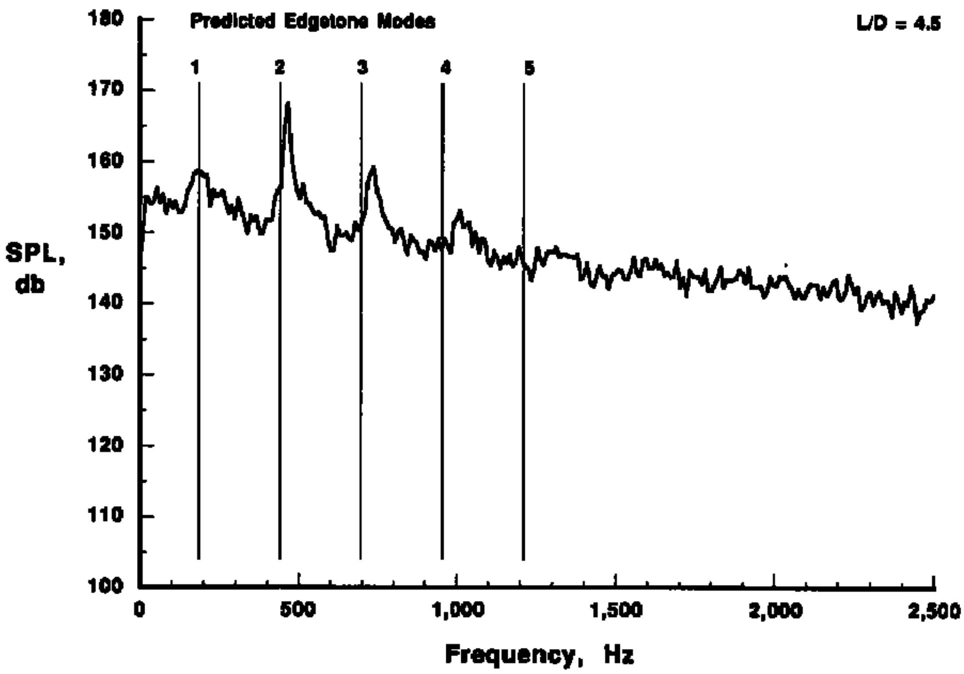

b. M_∞ = 0.95

Figure 8. Typical cavity pressure spectra and Rossiter edgetones, L/D = 4.5.

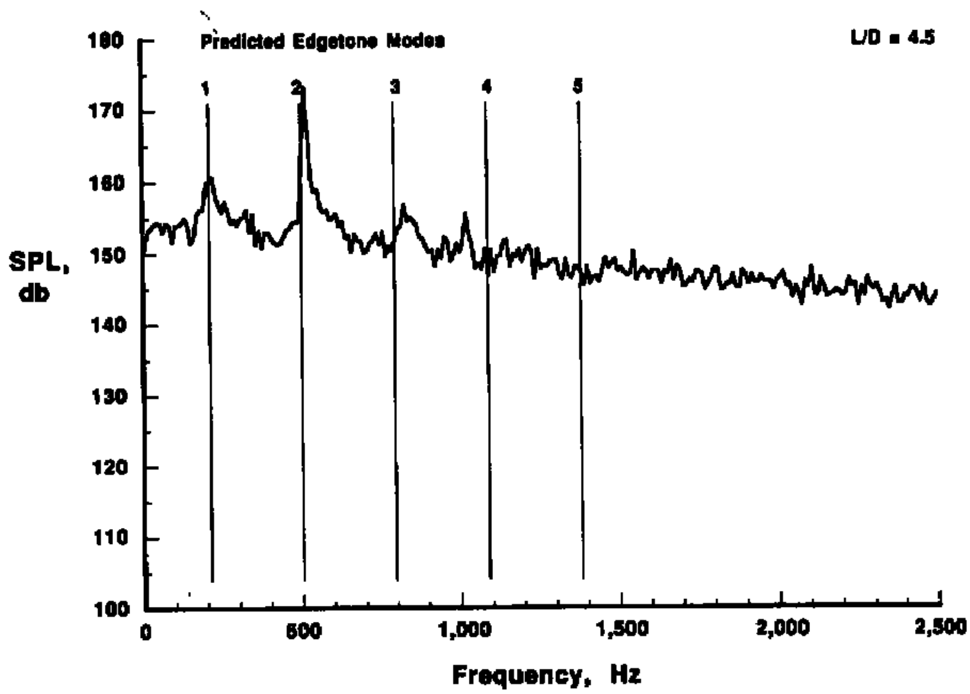

c. $M_\infty = 1.20$

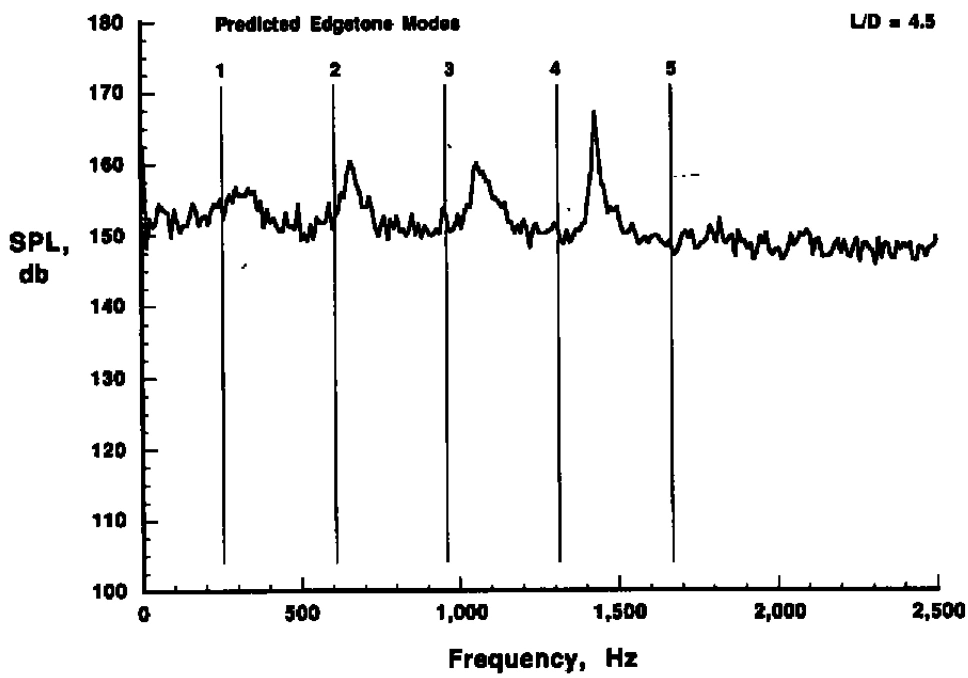

d. $M_\infty = 2.00$

Figure 8. Concluded.

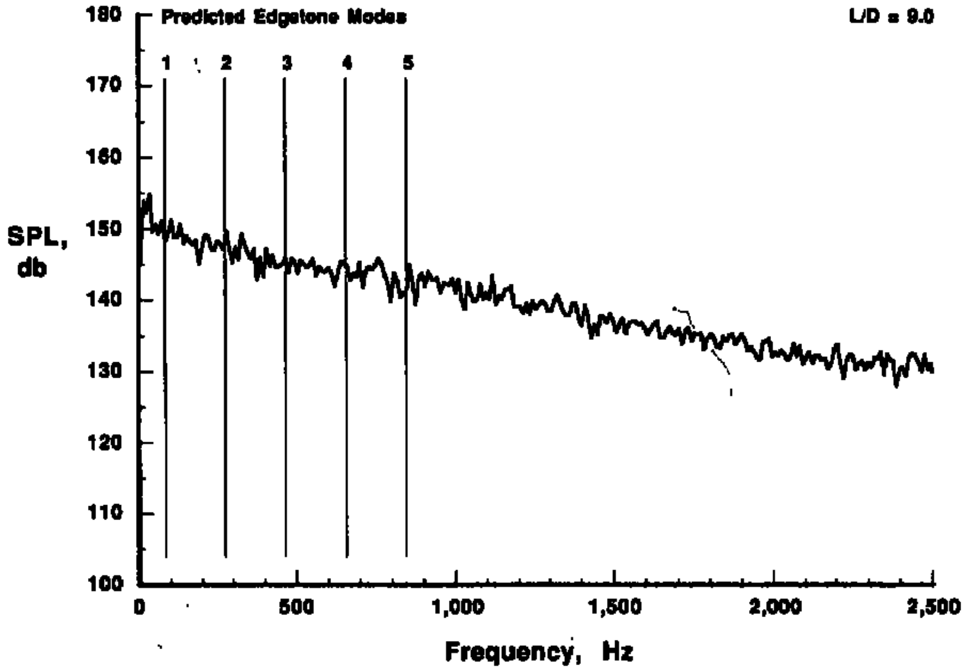

a. $M_\infty = 0.60$

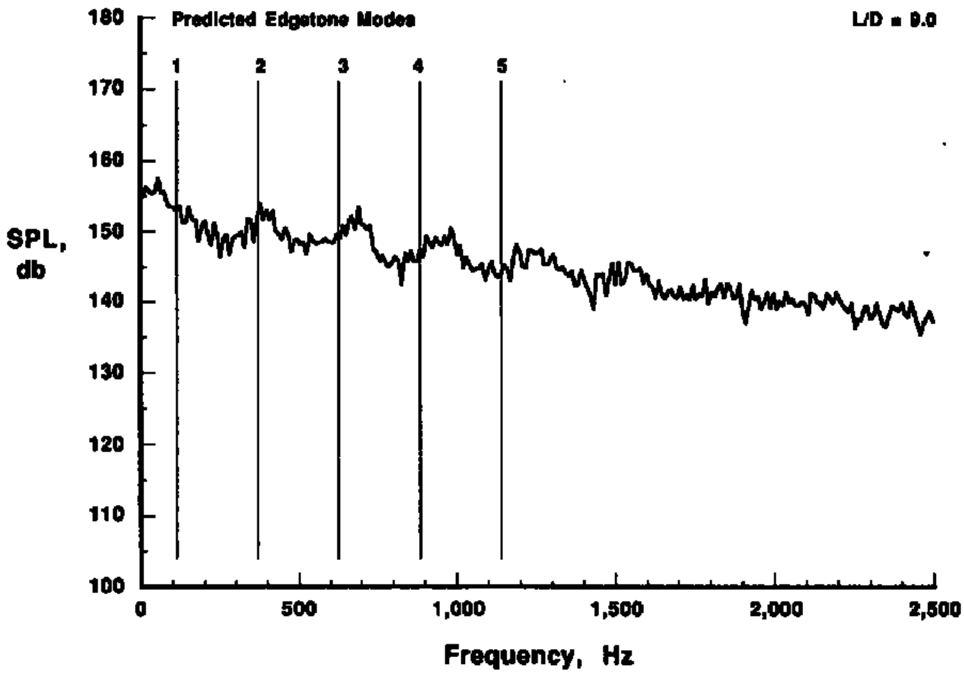

b. $M_\infty = 0.95$

Figure 9. Typical cavity pressure spectra and Rossiter edgetones, L/D = 9.0.

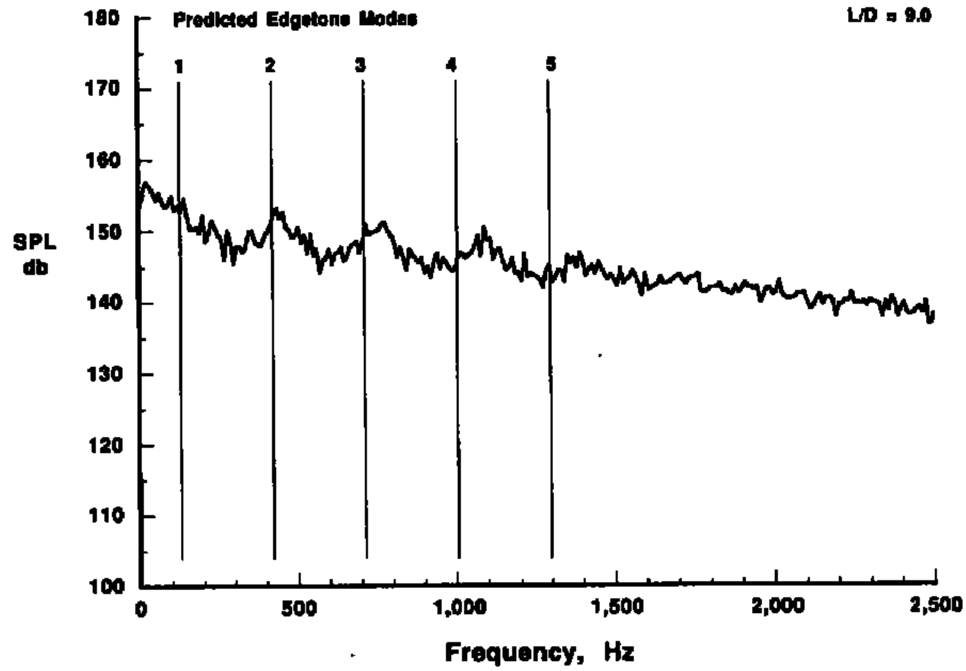

c. M_∞ = 1.20

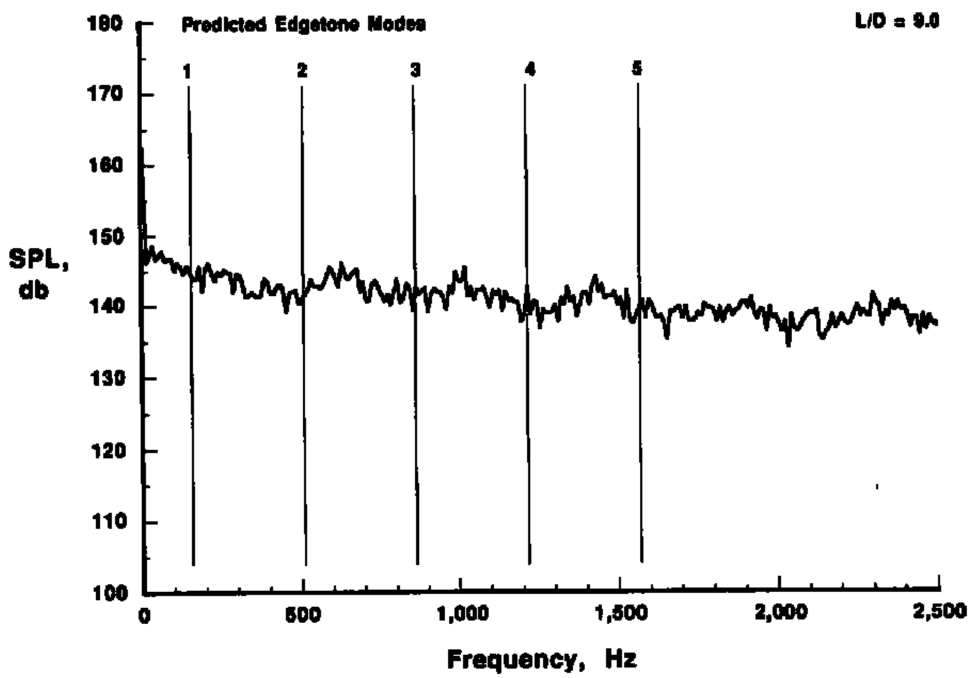

d. M_∞ = 2.00

Figure 9. Concluded.

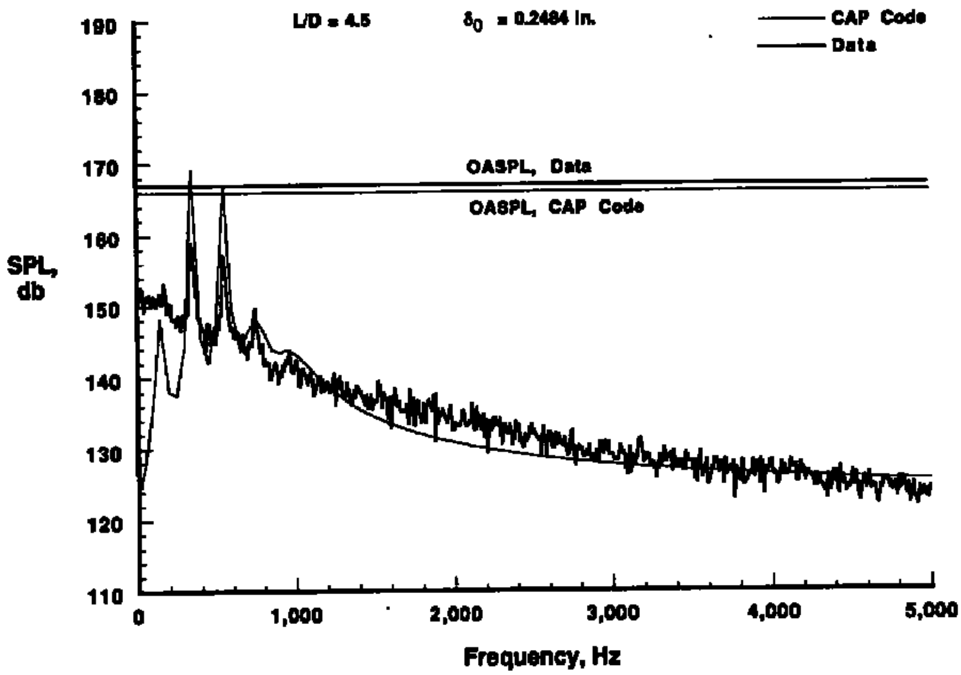

a. M_∞ = 0.60

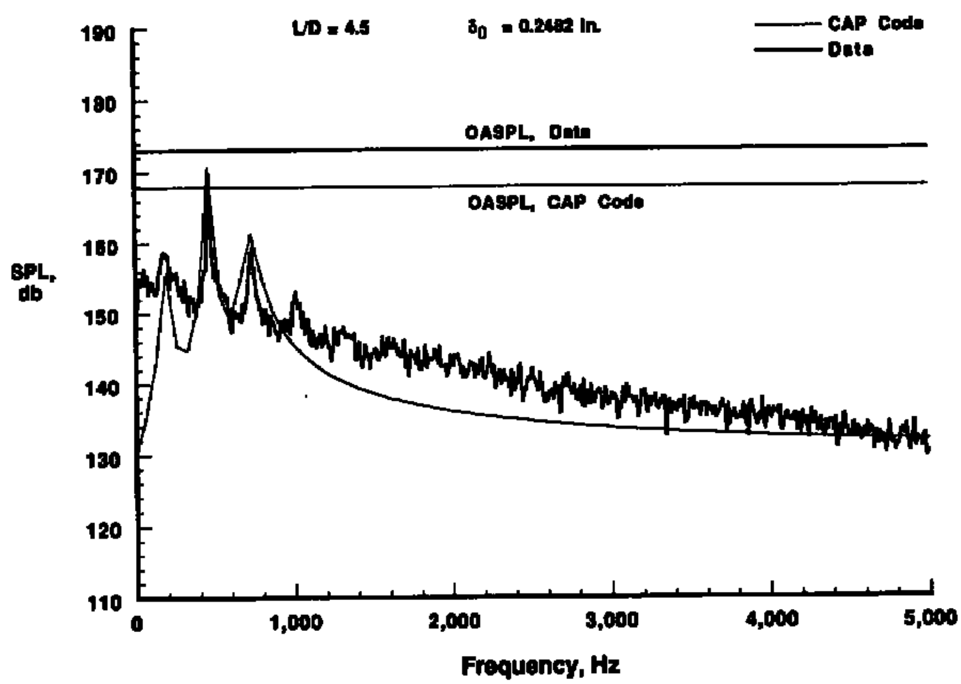

b. M_∞ = 0.95

Figure 10. Comparison of CAP Code predicted spectra and data, L/D = 4.5.

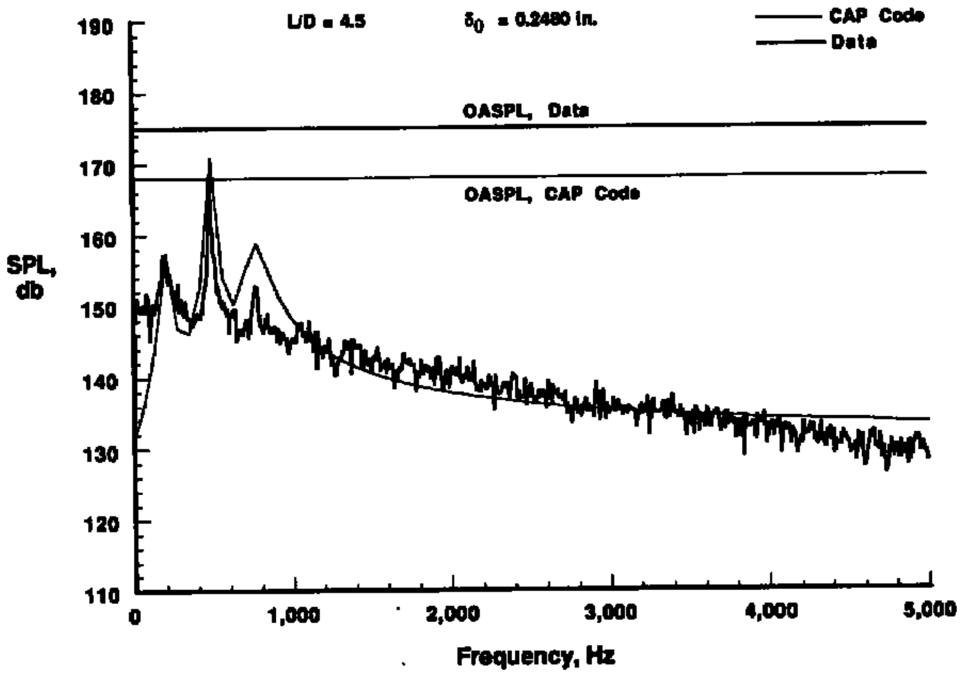

c. $M_\infty = 1.05$

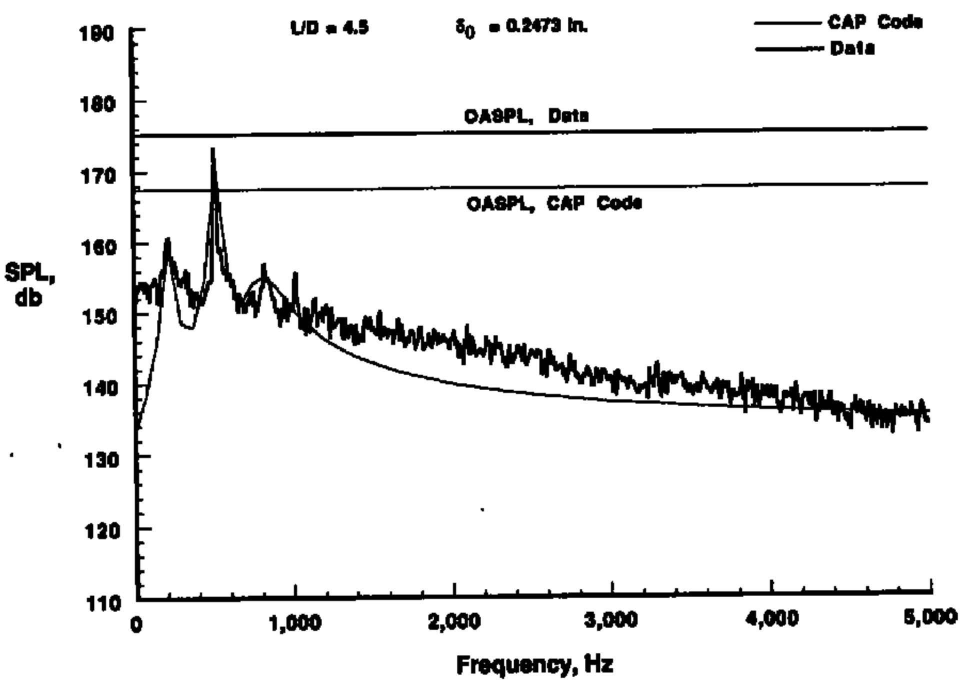

d. $M_\infty = 1.20$

Figure 10. Continued.

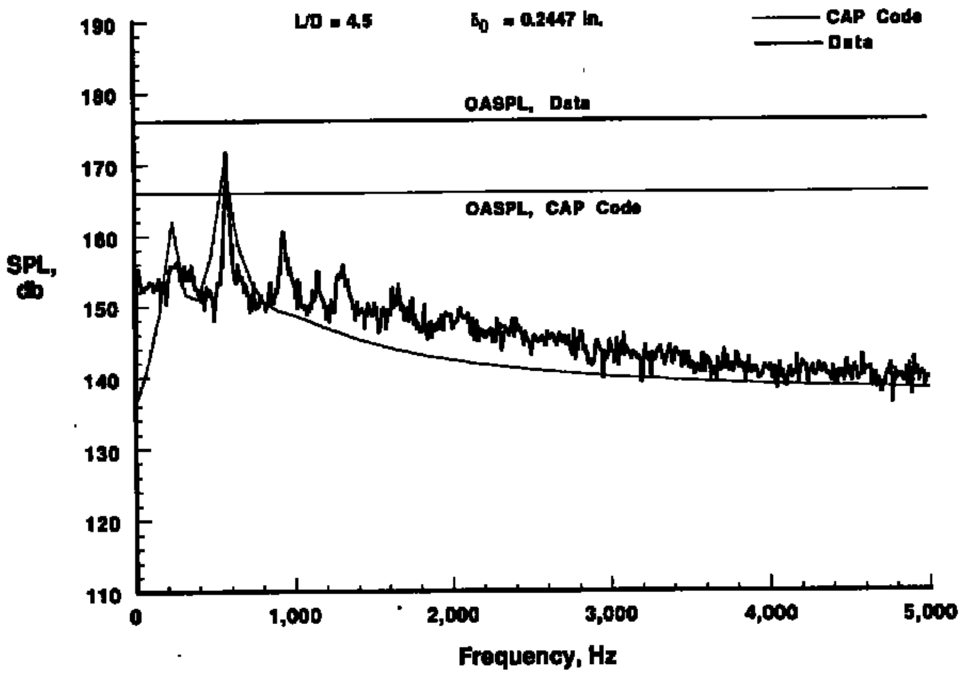

e. M_∞ = 1.50

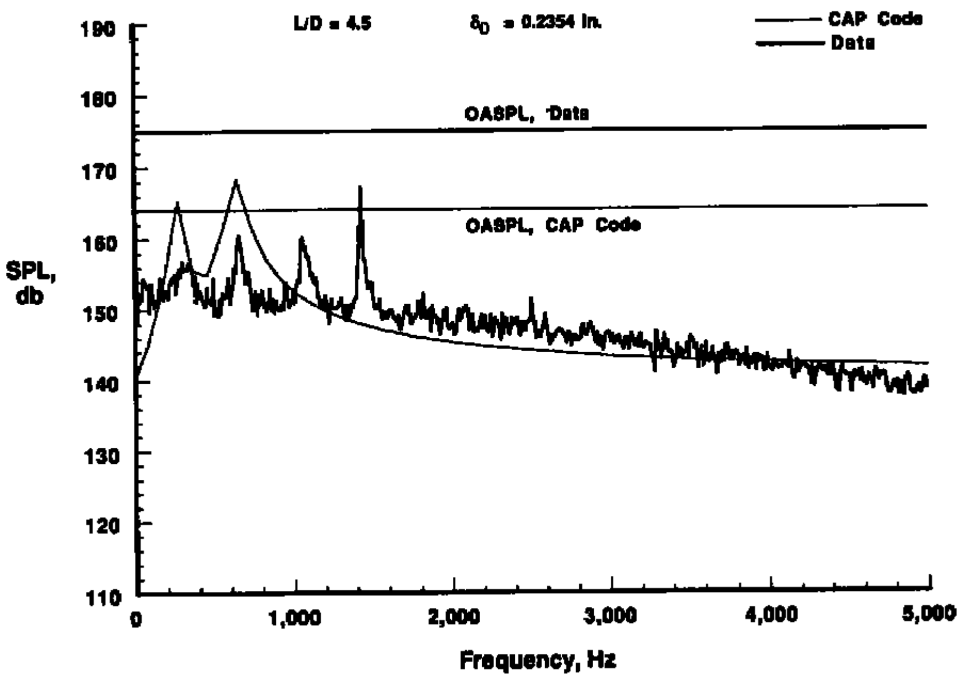

f. M_∞ = 2.00

Figure 10. Continued.

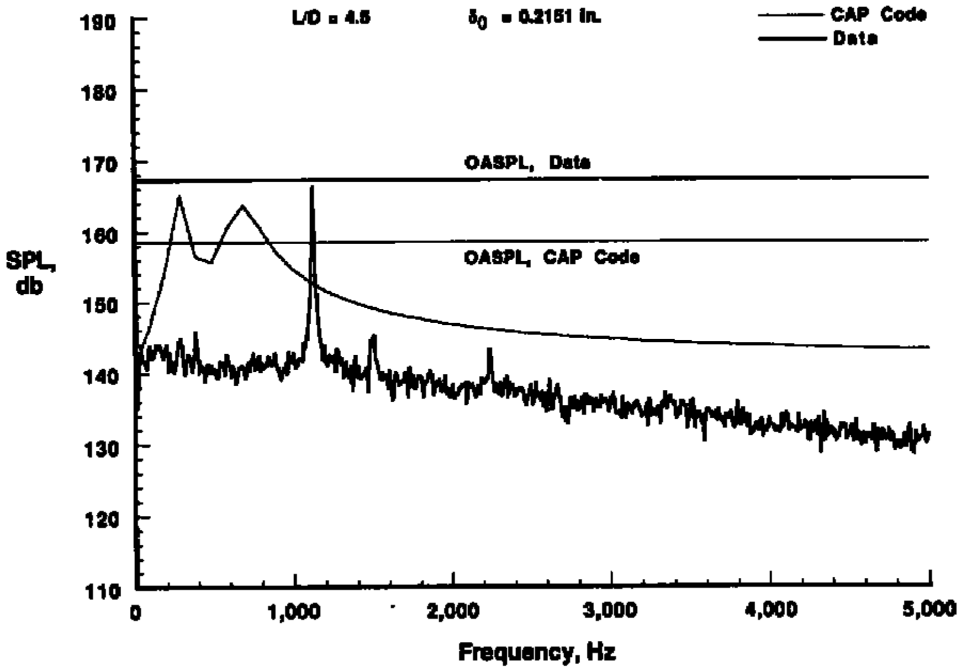

g. M_∞ = 2.75

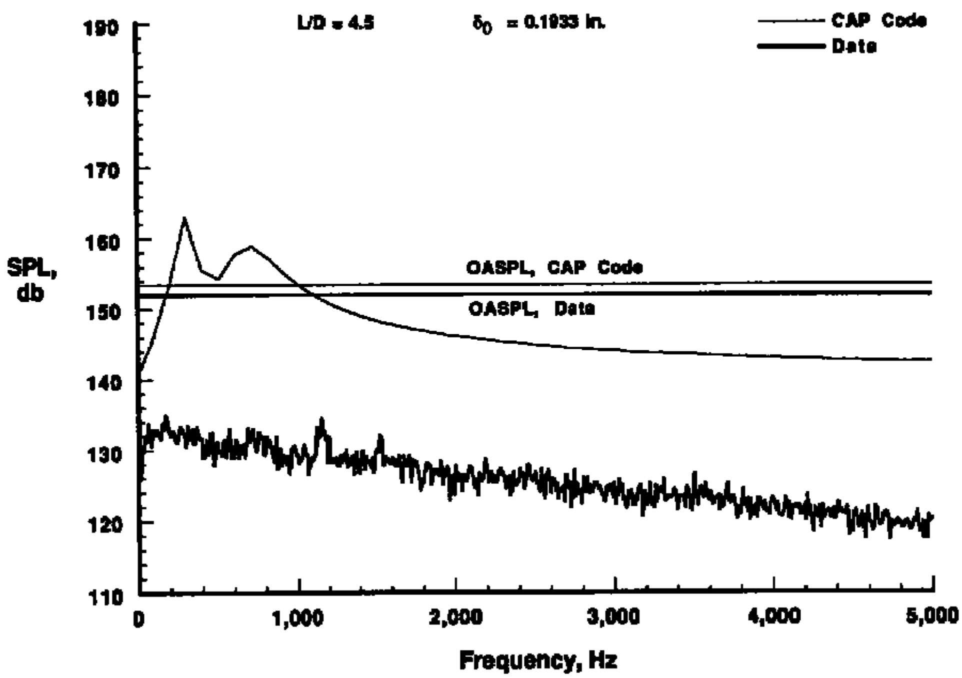

h. M_∞ = 3.51

Figure 10. Continued.

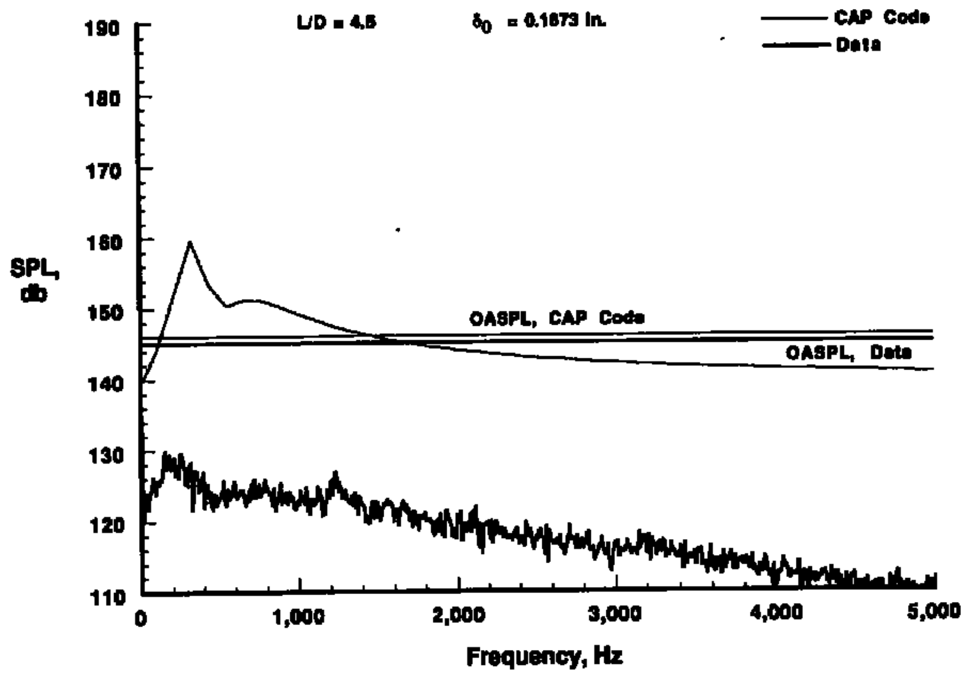

i. M_∞ = 5.04
Figure 10. Concluded.

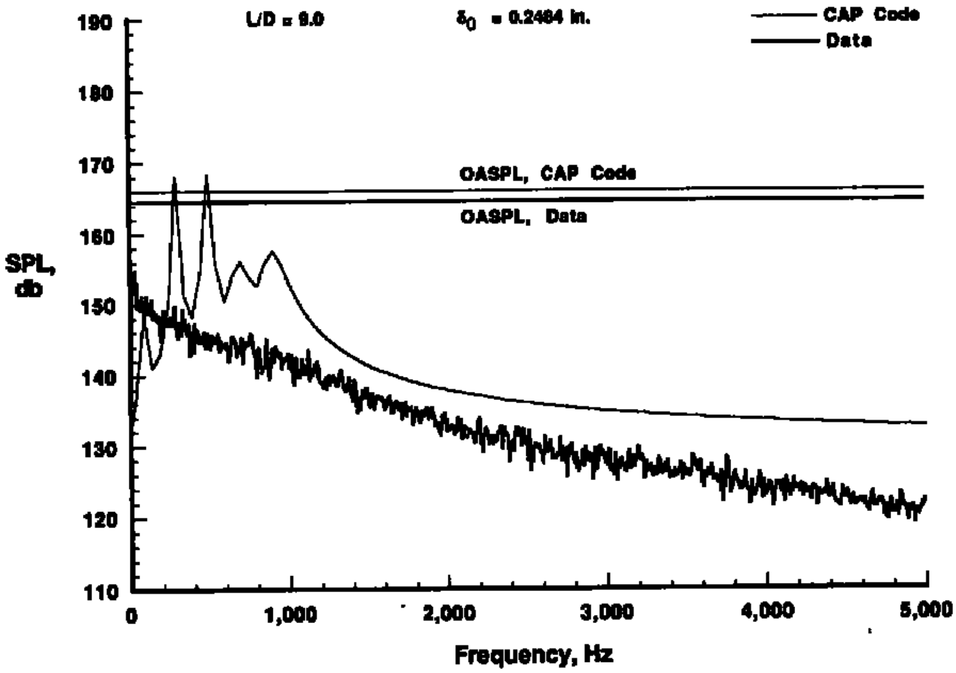

a. M_∞ = 0.60

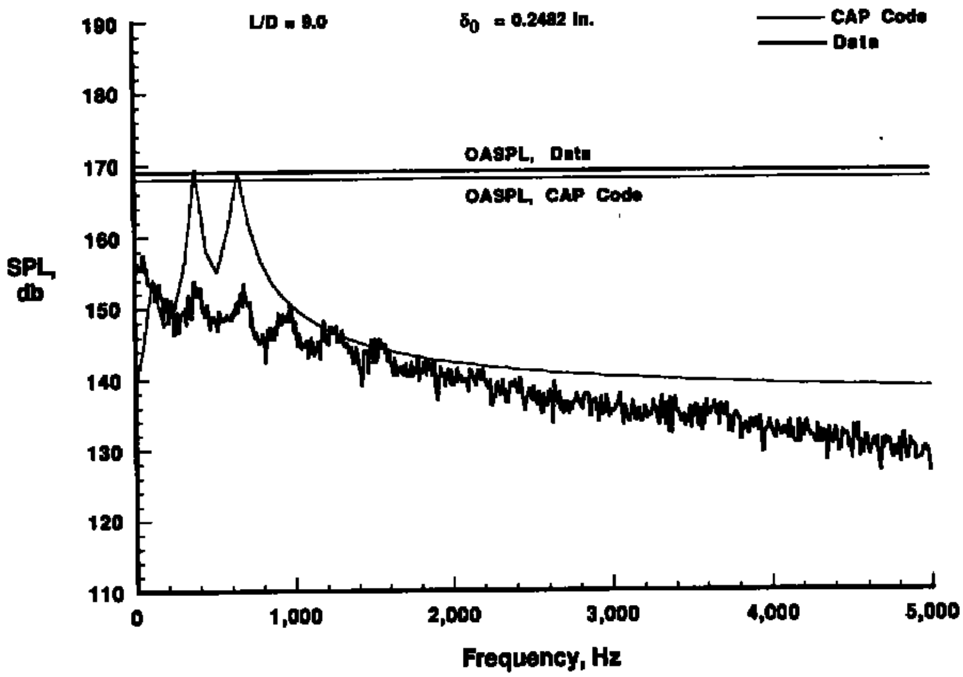

b. M_∞ = 0.95

Figure 11. Comparison of CAP Code predicted spectra and data, L/D = 9.0.

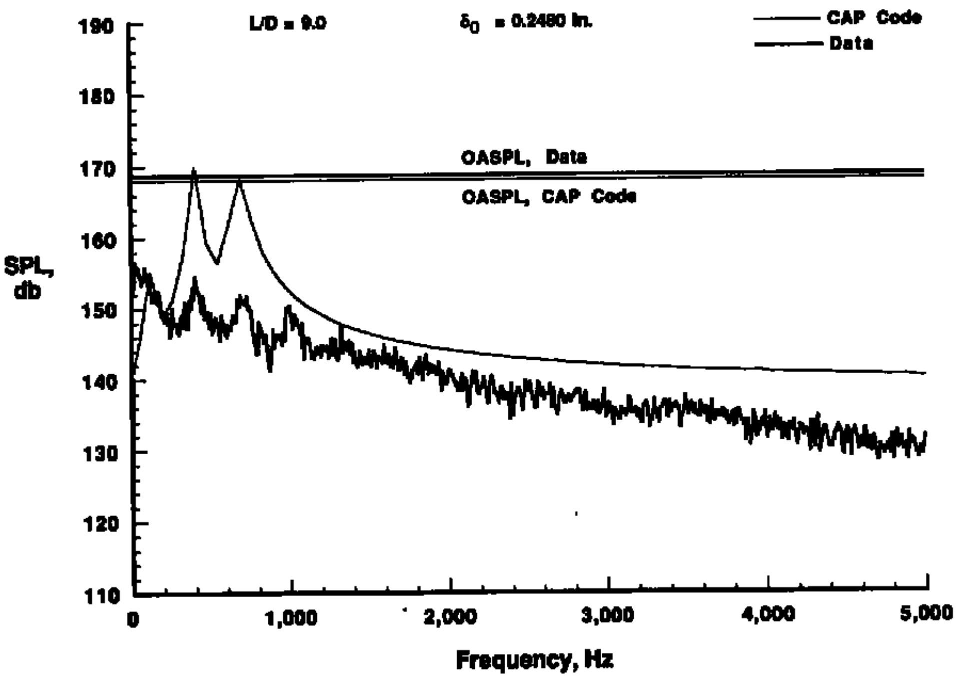

c. $M_\infty = 1.05$

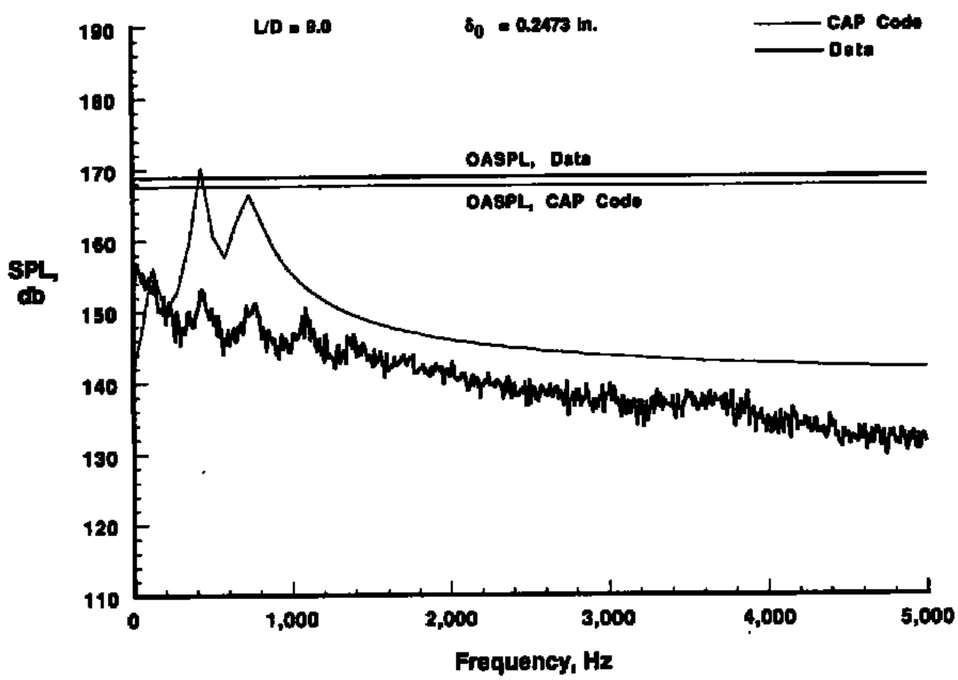

d. $M_\infty = 1.20$

Figure 11. Continued.

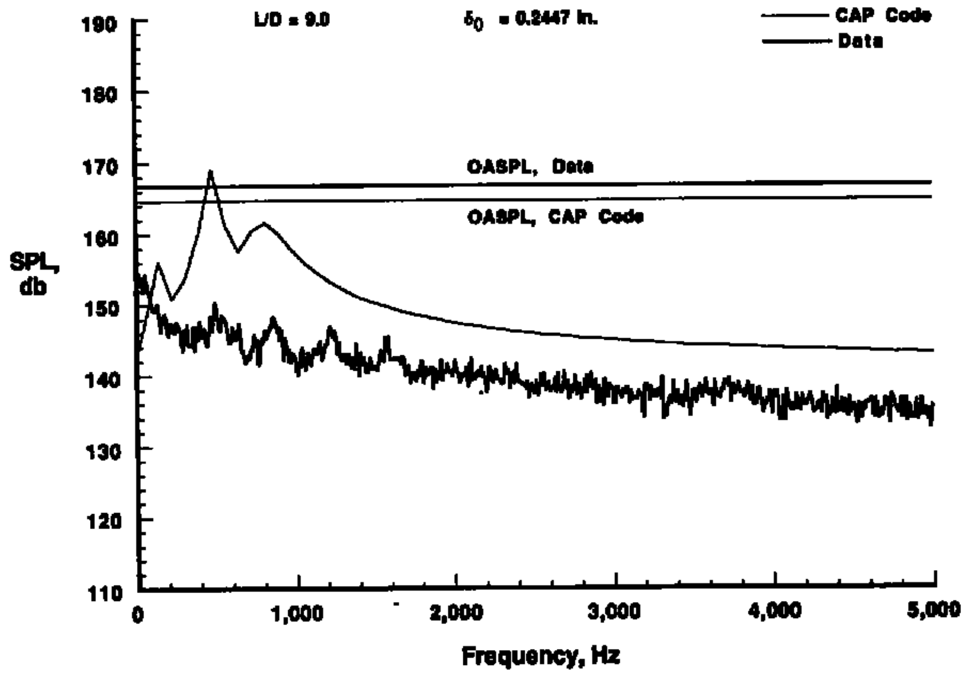

e. M_∞ = 1.50

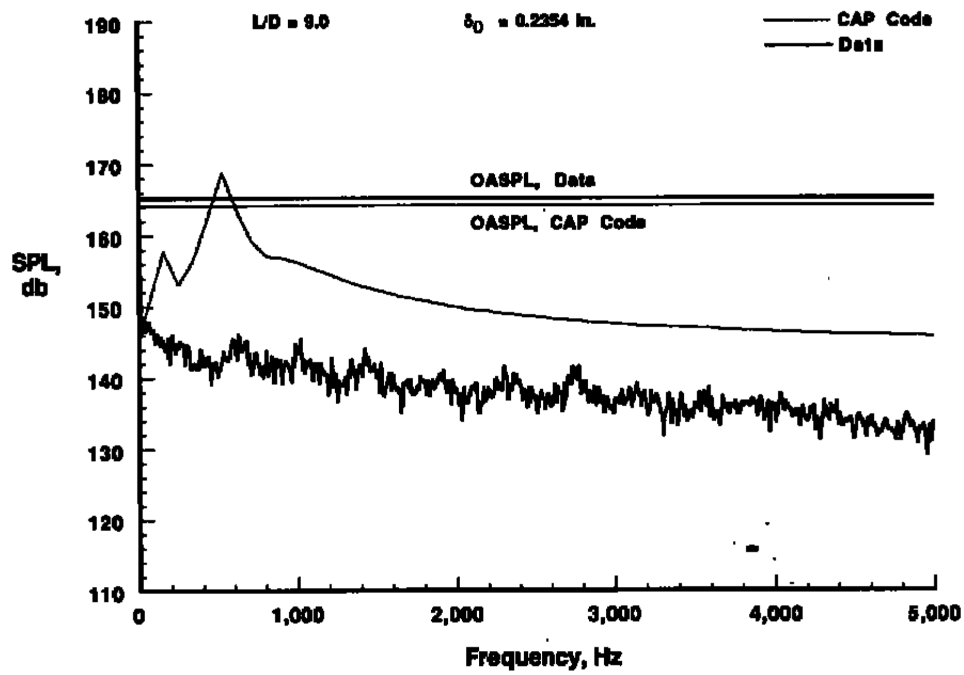

f. M_∞ = 2.00

Figure 11. Continued.

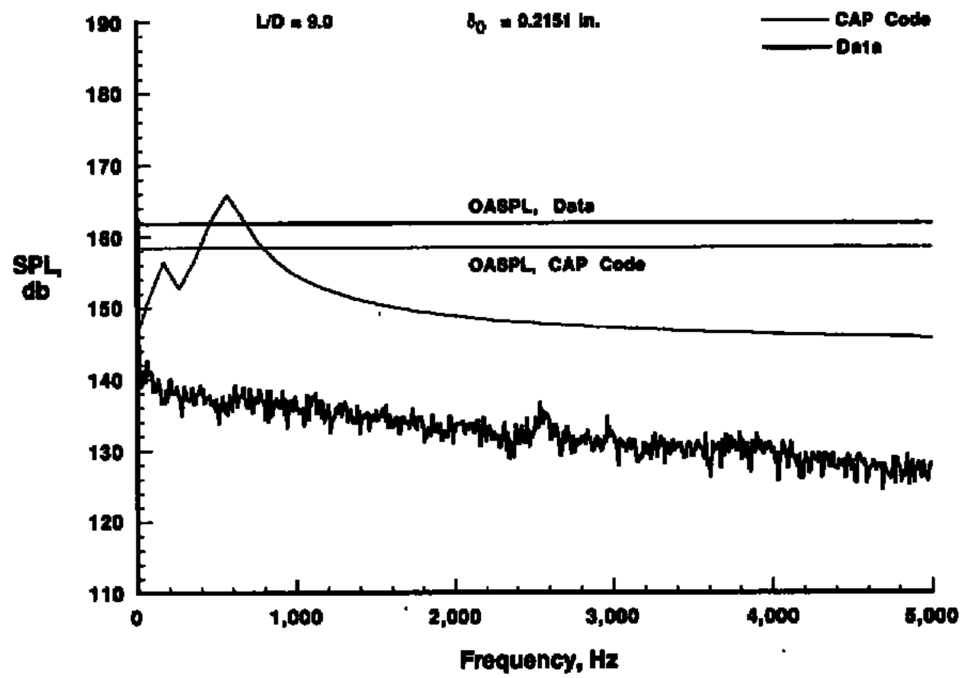

g. M_∞ = 2.75

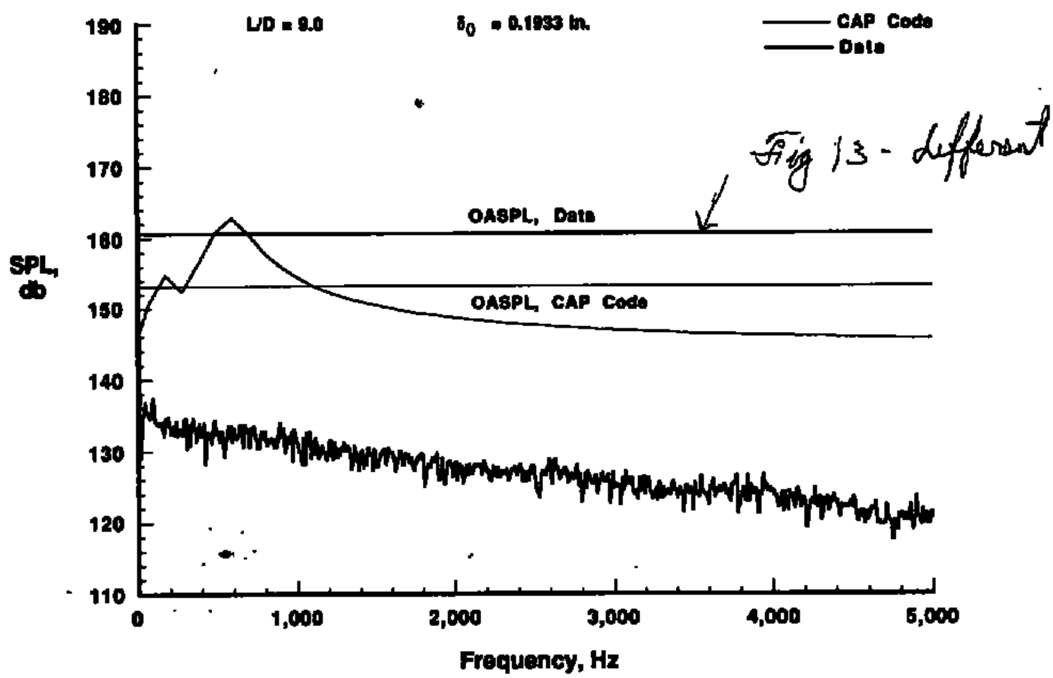

h. M_∞ = 3.51

Figure 11. Continued.

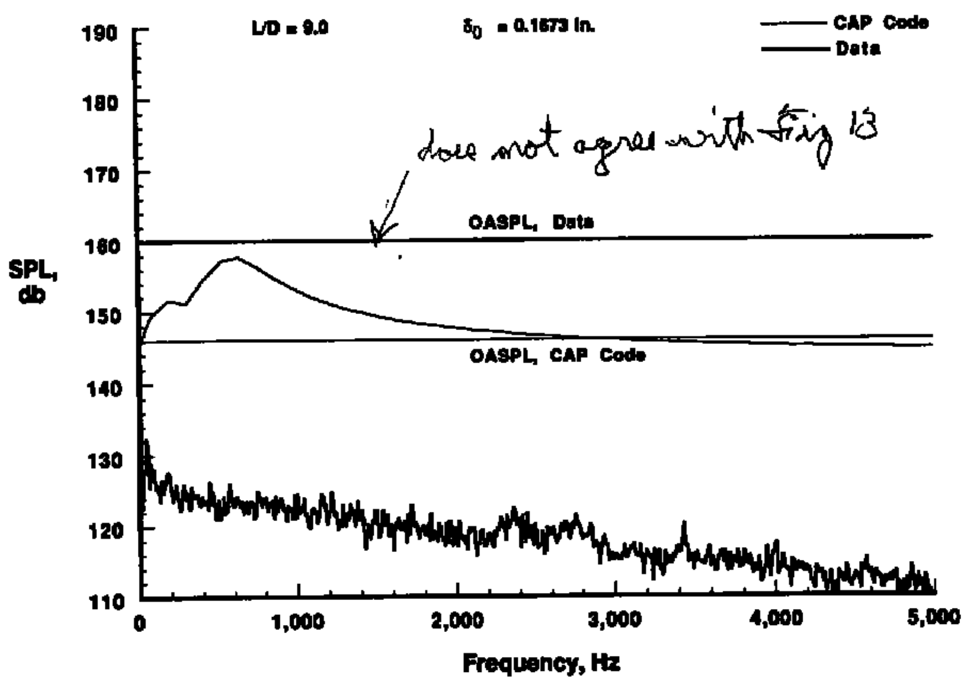

i. $M_\infty = 5.04$
Figure 11. Concluded.

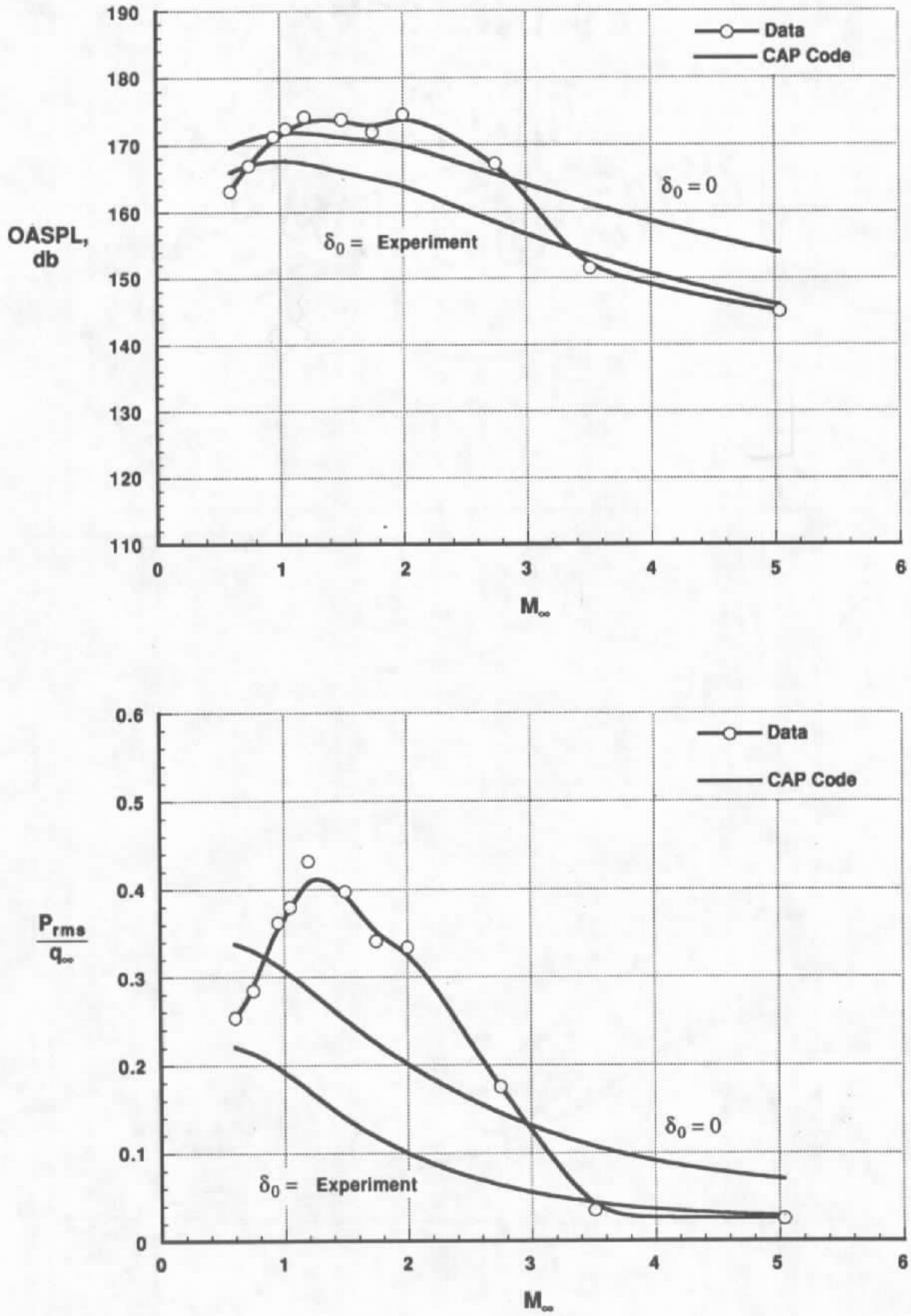

Figure 12. Comparison of CAP Code predicted overall rms pressure and data, L/D = 4.5.

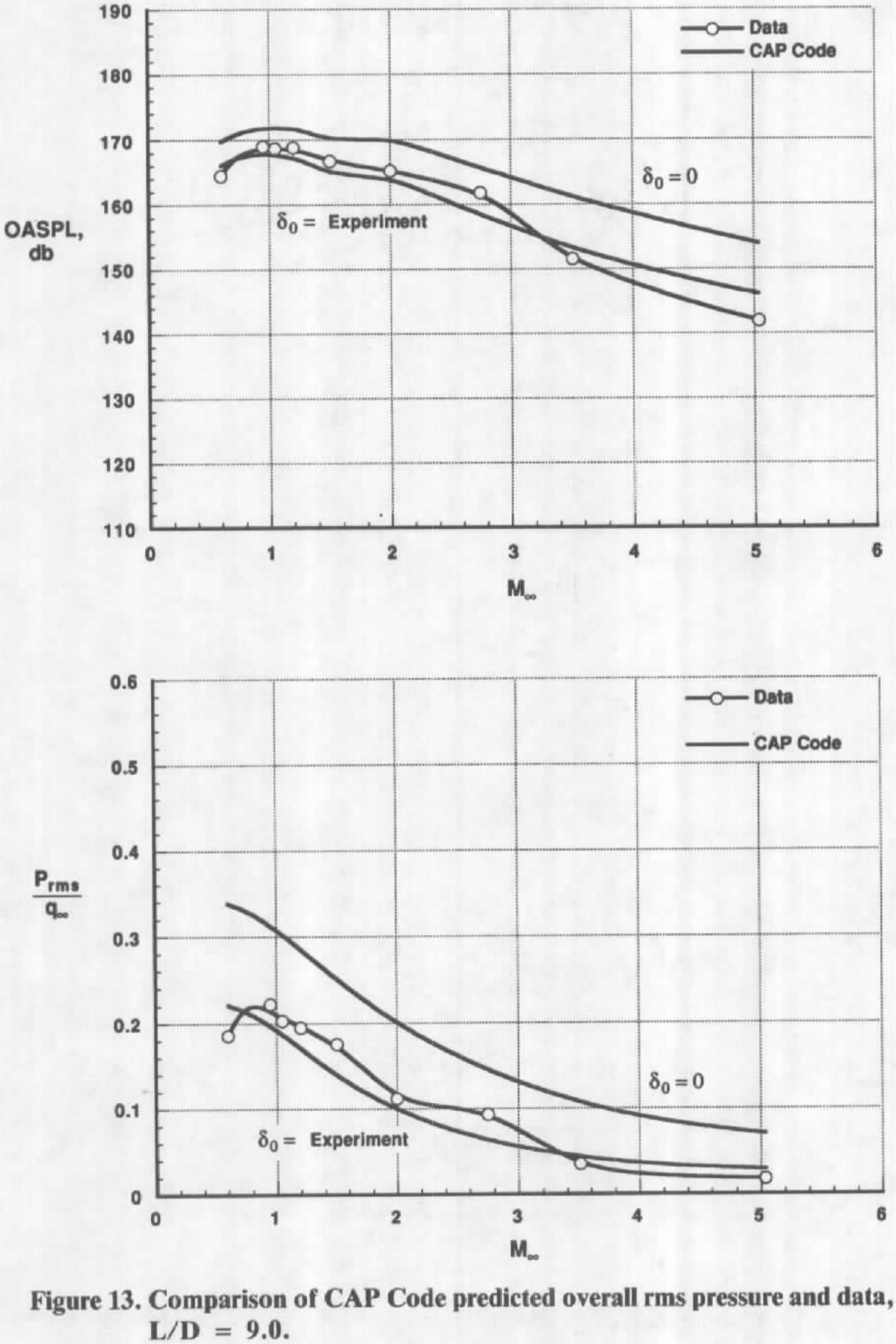

Figure 13. Comparison of CAP Code predicted overall rms pressure and data, L/D = 9.0.

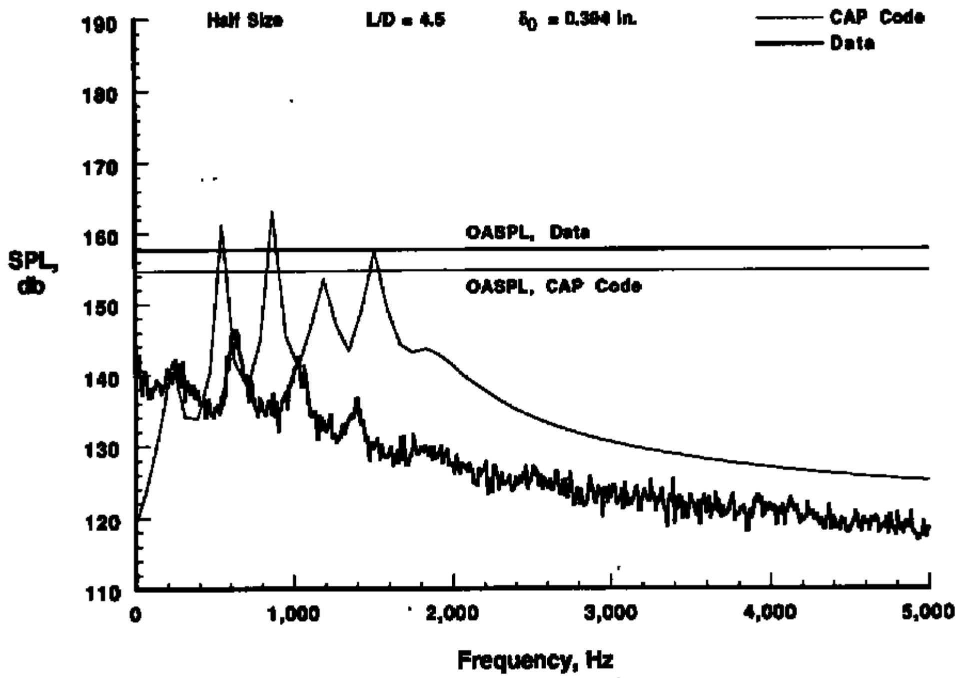

a. M_∞ = 0.60

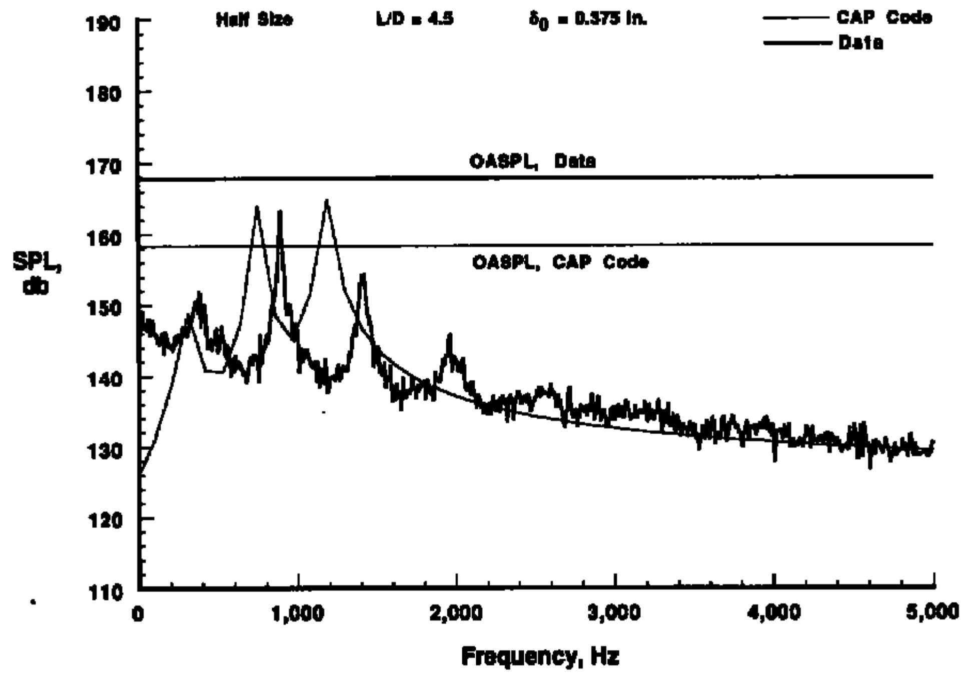

b. M_∞ = 0.95

Figure 14. Comparison of CAP Code predicted spectra and data, half-size cavity, L/D = 4.5, U-block open downstream.

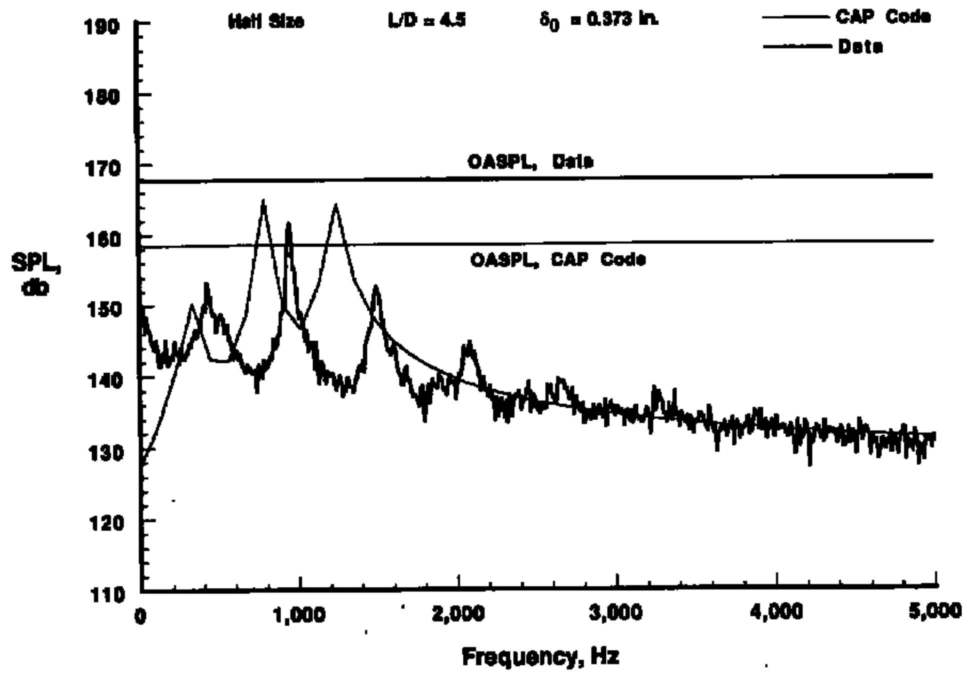

c. M_∞ = 1.05

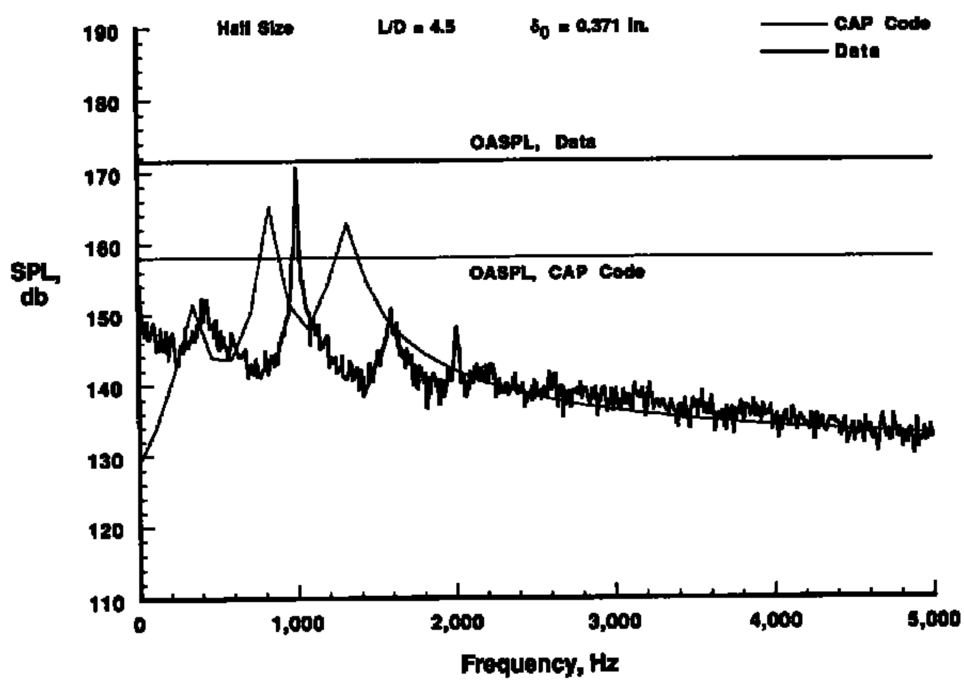

d. M_∞ = 1.20

Figure 14. Concluded.

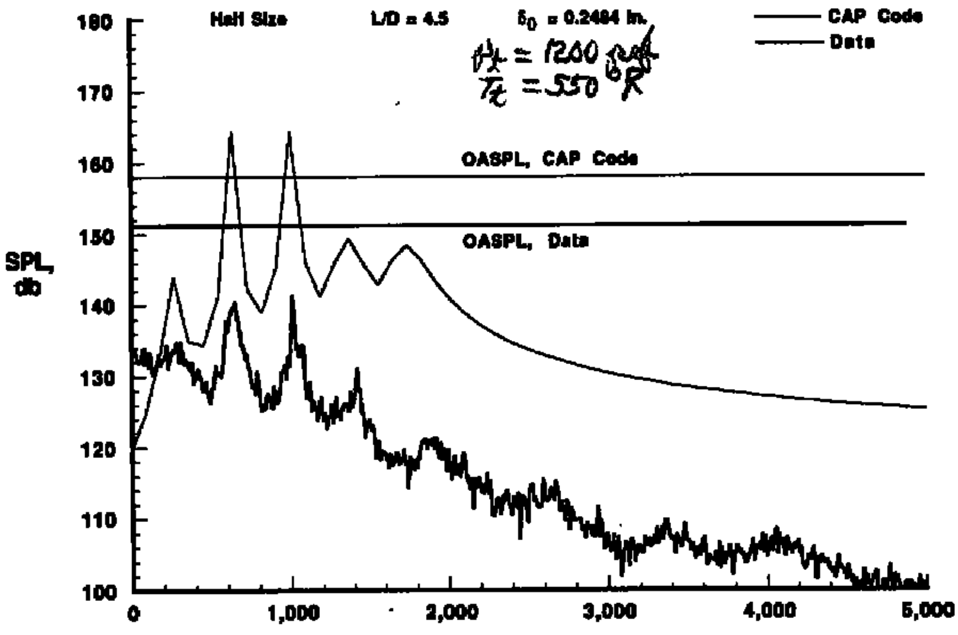

a. M_∞ = 0.60

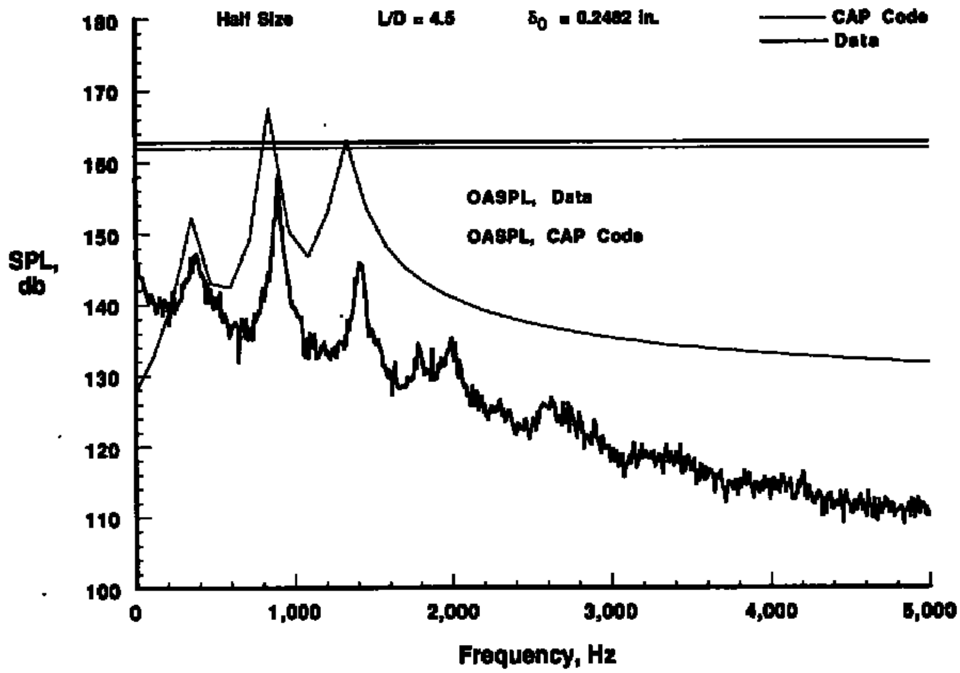

b. M_∞ = 0.95

Figure 15. Comparison of CAP Code predicted spectra and data, half-size cavity, L/D = 4.5, U-block open upstream.

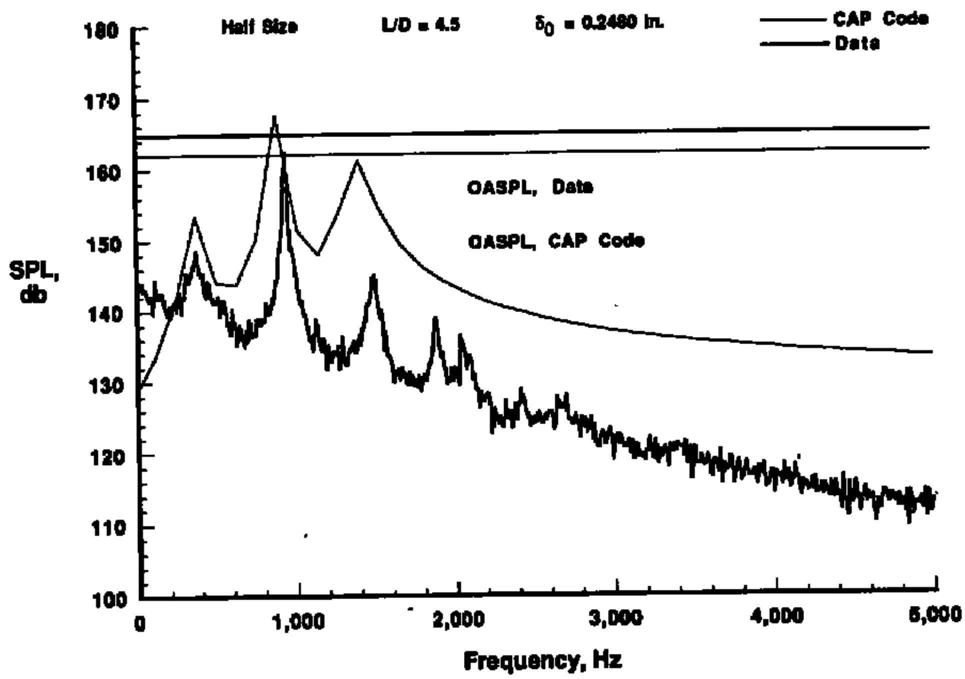

c. M_∞ = 1.05

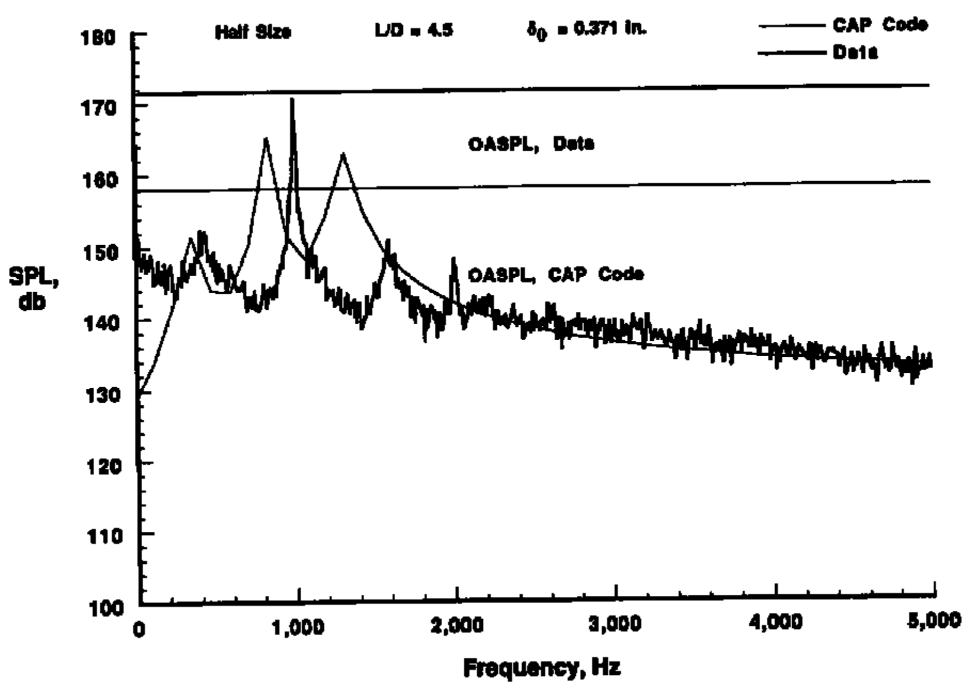

d. M_∞ = 1.20

Figure 15. Concluded.

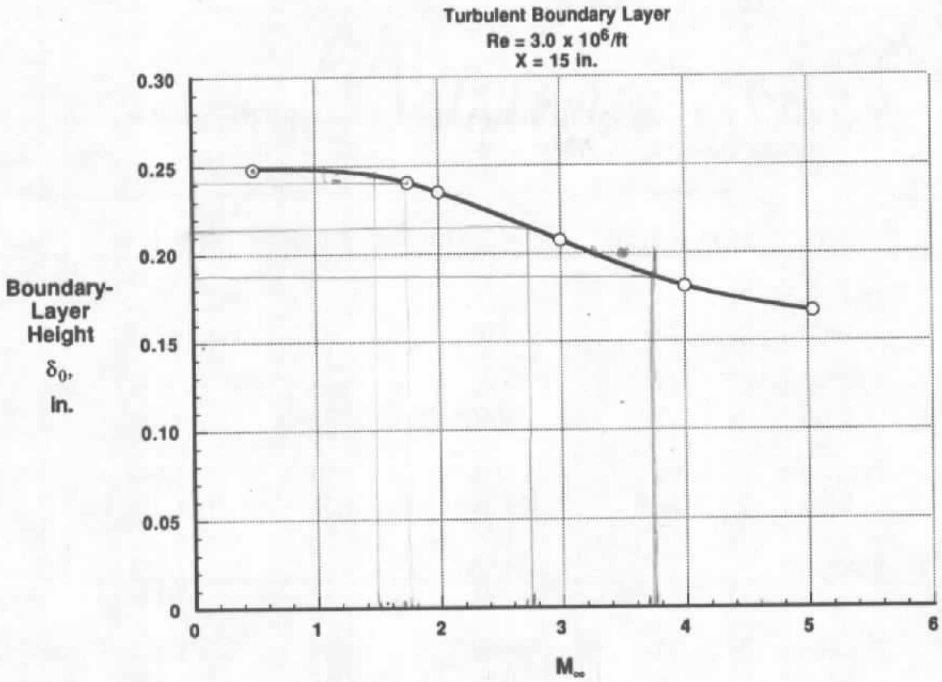

Figure 16. Boundary-layer height used for predictions.

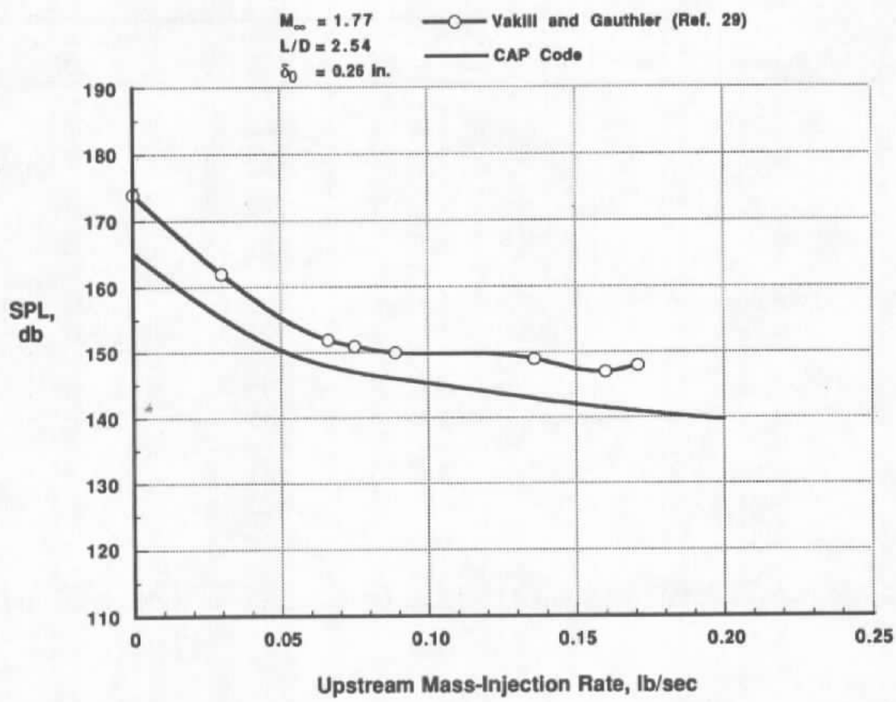

Figure 17. CAP Code prediction of overall rms pressure for a case of upstream bleed flow.

Table 1. Predicted and Measured Edgetone Frequencies

		L/D = 4.5				
M_∞	Source	m = 1, Hz	m = 2, Hz	m = 3, Hz	m = 4, Hz	m = 5, Hz
0.60	Prediction	137	327	518	708	898
	Data	137	352	547	752	967
0.95	Prediction	185	441	698	954	1,211
	Data	186	469	732	1,016	1,318
1.20	Prediction	210	502	794	1,087	1,379
	Data	225	518	830	1,025	1,338
1.50	Prediction	230	549	869	1,188	1,507
	Data	244	586	938	1,152	1,318
2.00	Prediction	254	608	961	1,314	1,668
	Data	303	664	1,064	1,436	1,797

		L/D = 9.0				
M_∞	Source	m = 1, Hz	m = 2, Hz	m = 3, Hz	m = 4, Hz	m = 5, Hz
0.60	Prediction	84	274	464	655	845
	Data	* ---	313	—	762	—
0.95	Prediction	113	369	626	883	1,139
	Data	—	400	684	986	1,270
1.20	Prediction	129	421	713	1,005	1,297
	Data	—	439	762	1,104	1,396
1.50	Prediction	141	460	779	1,099	1,418
	Data	—	498	859	1,230	1,592
2.00	Prediction	155	509	862	1,216	1,569
	Data	—	—	625	1,016	1,455

* Dash entries indicate that data values could not be resolved from wideband noise.

APPENDIX A

SUMMARY OF EXPERIMENTS

1.0 PLATE/CAVITY MODEL

Data used in the development of the CAP Code were recorded during experiments with a wind tunnel model consisting of a simple rectangular cavity with an opening 4 in. wide by 18 in. long (streamwise) built into a flat plate 16 in. wide by 47-in. long (Fig. A-1). Along the longitudinal edges of the flat plate, tip plates were installed to add stiffness and reduce three-dimensional flow over the surface of the plate. Tip plates used during the tests at transonic conditions were 2 in. high (Fig. A-1a), and 6-in. high for the tests at supersonic conditions (Fig. A-1b). The additional height allowed installation of two 3-in.-diam portholes of Schlieren-quality optical glass for observations of unsteady flow-field characteristics inside the cavity.

The cavity floor could be installed at any of several discrete depths between 0 and 4 in. Only 1.25-, 2-, and 4-in. depths were used during the tests, providing cavities of length-to-depth ratios (L/D) of 14.4, 9.0, and 4.5, respectively (Figs. A-1a and A-1b). A limited quantity of data was recorded with a block inserted in the cavity in the shape of the letter "U" (Fig. A-2). The dimensions of the cavity were halved with the block in place, i.e. to length by width by depth dimensions of 9 by 2 by 2 in. The open end of the "U" could be faced either up- or downstream.

2.0 INSTRUMENTATION AND BOUNDARY-LAYER RAKE

Static pressure on the plate and cavity model surfaces could be measured at 95 locations: 26 on the flat plate, and 69 on the walls and floor of the cavity (Fig. A-3). Pressures were sensed using electronically scanned pressure (ESP) modules, rated at 5 psi maximum differential (psid), mounted on the backside of the flat plate. A near-vacuum was used as the reference. For verification purposes, one channel on each transducer module was connected to a known pressure source of 2 psia. The temperature of each pressure transducer module was monitored to provide a means of correcting for temperature-induced zero shift. Module temperatures were controlled within $\pm 1°F$ during the tests at supersonic conditions by water cooling.

Fluctuating pressures were measured with Kulite® differential transducers at up to 45 locations: 7 on the flat plate, and 38 on the walls and floor of the cavity (Fig. A-4). Each transducer was rated at ± 5 psi, with a maximum allowable differential pressure three times the nominal rating of 15 psi. Each reference pressure port was vented to the static pressure in the instrument housing on the backside of the flat plate, which was approximately equal to free-stream static pressure (P_∞). Up to 64 channels of transducer signals could be simultaneously sampled, converted from analog to digital form, filtered, and recorded on a magnetic hard disk using a MASSCOMP® minicomputer as a process controller and data analyzer. Transducer signals were scanned at a rate of 10,000 samples/sec, producing a data flow of approximately 1 MB/sec. Because of data-storage limitations, only approximately 30 data points could be stored on the disk, after which data were transferred to a magnetic tape. After the test, data tapes were transported to a large mainframe computer for final fast-Fourier-transform (FFT) analysis.

Other instruments were also attached to the plate/cavity model (Fig. A-5). Angle of attack of the generic cavity model was measured with a gravity-sensing angular position indicator (Schaevitz®). Two single-axis accelerometers were used to provide a measurement of the plate/cavity model vibrations. One was mounted on the backside of the flat plate just upstream of the cavity to sense vertical acceleration in the Z direction. The other was mounted on the backside of the downstream bulkhead of the cavity to sense axial acceleration in the X direction. At a location 1-in. aft of the sharp leading edge of the plate, a ¼-in. wide strip of No. 60 size grit was applied to promote laminar-to-turbulent transition of the boundary layer. Five hot-film constant-temperature anemometers were installed along the flat plate upstream of the cavity to determine the laminar/turbulent state of the boundary layer. Four Chromel® -Alumel® thermocouples were mounted on the backside of the model to monitor plate and cavity surface temperatures.

Throughout the tests at supersonic conditions, Schlieren photographs of the cavity flow field were recorded for all configurations and test conditions at selected model attitudes. Black and white and color Schlieren high-speed movies (4,000 frames/sec) were also recorded for selected test conditions.

During blockage evaluation for the tests at supersonic conditions, the thickness of the boundary layer approaching the cavity was determined using a survey rake, consisting of 10 pitot tubes aligned vertically to 0.3 in. above the surface of the plate (Fig. A-6).

3.0 FLOW CONDITIONS AND DATA ACQUISITION

Data were recorded at Mach numbers in the range from 0.60 to 2.00 during the transonic tests, and from 2.00 to 5.04 during the supersonic tests. A nominal unit Reynolds number of 3×10^6/ft was selected, but since the transonic tests were done at a constant P_t of 1,200 psfa, unit Reynolds number varied from 1.9 to 3.0×10^6. The selected value of 3×10^6 was maintained during the supersonic tests. Some data were recorded at Re = 1×10^6 and 2×10^6/ft. Nominal values of the flow conditions are listed in Table A-1.

The wind tunnel tests were controlled to a large degree by various microprocessors. Flow conditions and model attitudes were set and maintained according to a programmed sequence, with signals being transmitted from a process controller to a data acquisition system to initiate the data recording cycle. During the transonic tests, all static pressure orifices were scanned at a rate of 20,000 samples/sec at intervals of 0.01 sec; but during the supersonic tests, static pressures and rake pressures were averages of 10 samples taken over a time span of 1 sec. The fluctuating pressure recording and analysis cycle was initiated during the tests by a signal transmitted from the tunnel data acquisition system to the MASSCOMP system. The recording process continued for 25 sec (15 sec for file management and 10 sec of actual data acquisition), during which time the tunnel control and data systems were prevented from taking any action. After data were recorded, a signal was transmitted by the MASSCOMP system to release the tunnel control system for appropriate test condition changes.

4.0 DATA CORRECTIONS AND MEASUREMENT UNCERTAINTIES

During the tests at transonic conditions, Mach number in the free stream was maintained within ±0.010 of the specified value, with a calculated uncertainty of ±0.003. Mach number in the supersonic free stream was maintained within ±0.016 of the selected value.

Quality of the experimental data was estimated by considering the effects of both systematic and random errors. Statistical confidence intervals of ±2 standard deviations, i.e., assured to include 95 percent of the measured values, were estimated from (1) the calibrations of the instruments used to sense the pressure and temperature of the airflow; and (2) the repeatability and uniformity of the free-stream flow during calibration of the wind tunnel. By using a Taylor series method of error propagation (Ref. A-1), the values of these intervals were combined to determine the 95-percent confidence intervals of the conventional static pressure coefficients that are listed in Table A-2. The uncertainty of the aeroacoustic data was estimated to be ±1 db for all conditions.

The Schaevitz absolute angle indicator attached to the underside of the flat plate (Fig. A-5) was used to set angle of attack of the generic cavity model. Consequently, corrections for the angular displacement of the generic cavity model attributable to the primary sting support deflections were unnecessary. The confidence interval for angle of attack of the plate/cavity model was ±0.10 deg.

5.0 DATA REDUCTION

All transducer outputs were sampled simultaneously 10,000 times/sec for 5 or more sec during a typical data point, producing approximately 50,000 pressure measurements for each transducer, which were transformed into power spectral density (PSD) graphs in the frequency domain using conventional fast Fourier transform (FFT) techniques. The set of pressure-time samples for each data channel was partitioned into subsets, or ensembles, of 1,024 samples each. Consequently, the bandwidth of the transformed data was 10,000/1,024, or approximately 9.76 Hz. Spectra from 25 ensembles were averaged to obtain the final PSD spectrum. Spectra extended over the range 0 to 5,000 Hz to be consistent with the sampling rate. All spectral data presented herein have been calculated with the Hanning data-tapering "window."

In the frequency domain, sound pressure level (SPL) is often more convenient. Therefore, acoustic spectra are presented in the conventional SPL format, using the familiar

$$SPL = 20 \log \left(\frac{P_{rms}}{P_{ref}} \right)$$

(The reference pressure, P_{ref} was the international threshold of audibility, i.e. 2 Pascals, or approximately 2.9×10^{-9} psi.) However, since the wind tunnel results were recorded at various values of total pressure (hence, different dynamic pressure, q_∞), comparison of overall rms data recorded at various Mach numbers and total pressures is more appropriate using the parameter P_{rms}/q_∞ rather than SPL as the dependent variable. Therefore, in cases where clarification would result, data are illustrated using both techniques.

REFERENCE

A-1. Beers, Yardley. "Introduction to the Theory of Error." Addison-Wesley Publishing Company, Inc., Reading, Massachusetts, 1957, pp. 26-36.

Linear Dimensions Are Inches

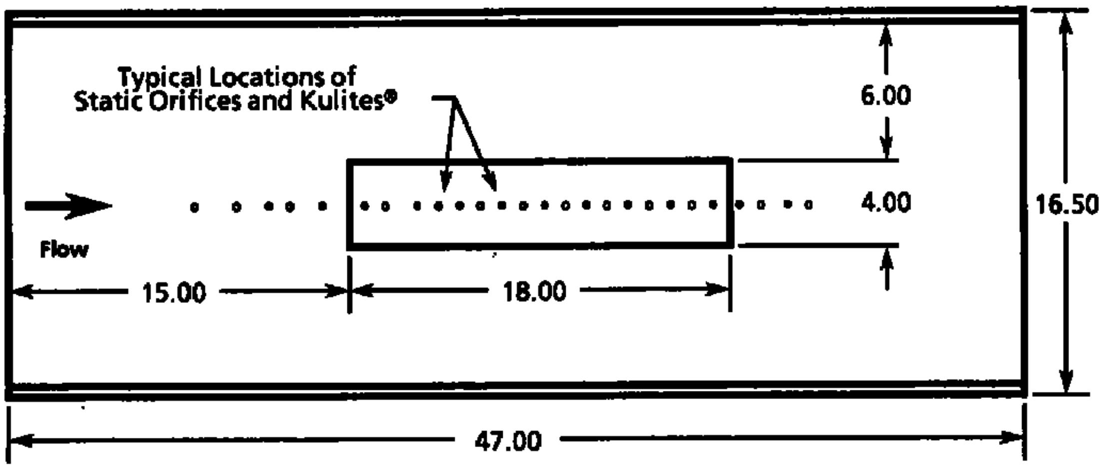

Top View (As Mounted in Wind Tunnel) of Plate/Cavity Model

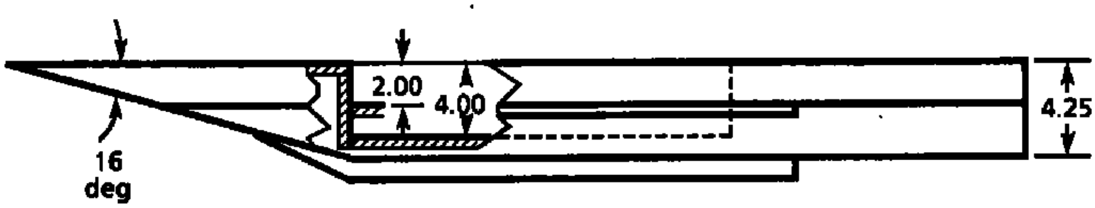

Side View

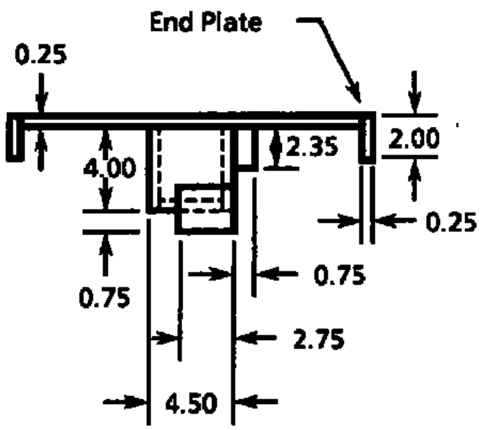

Front View

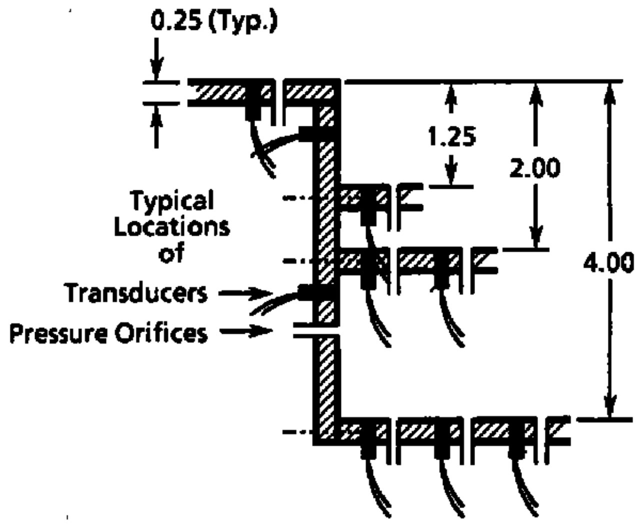

Section Through Cavity Showing Adjustable Ceiling

a. Model used in transonic tests

Figure A-1. Dimensions of the flat-plate/cavity model.

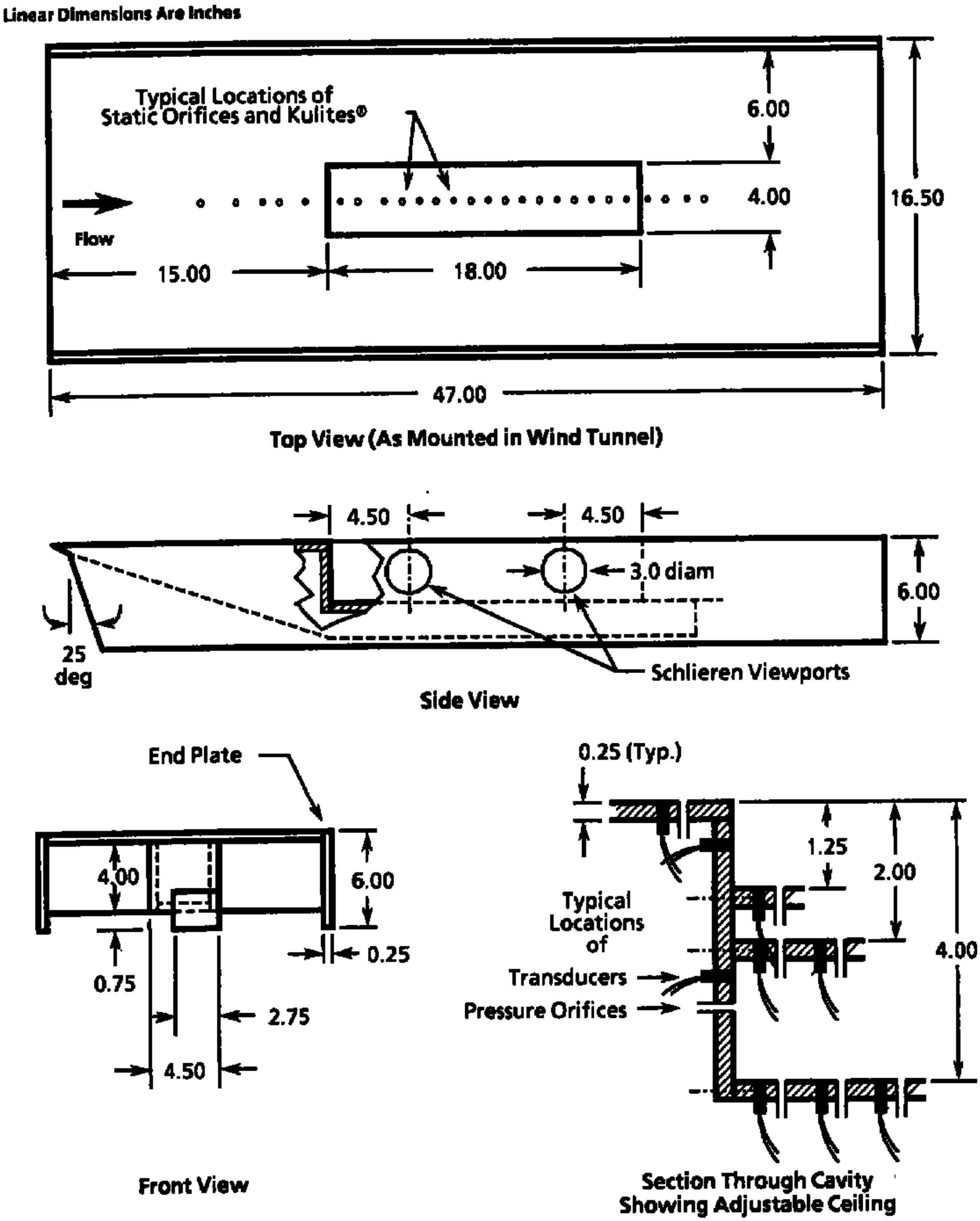

b. Model used in supersonic tests
Figure A-1. Concluded.

Dimensions Are Inches

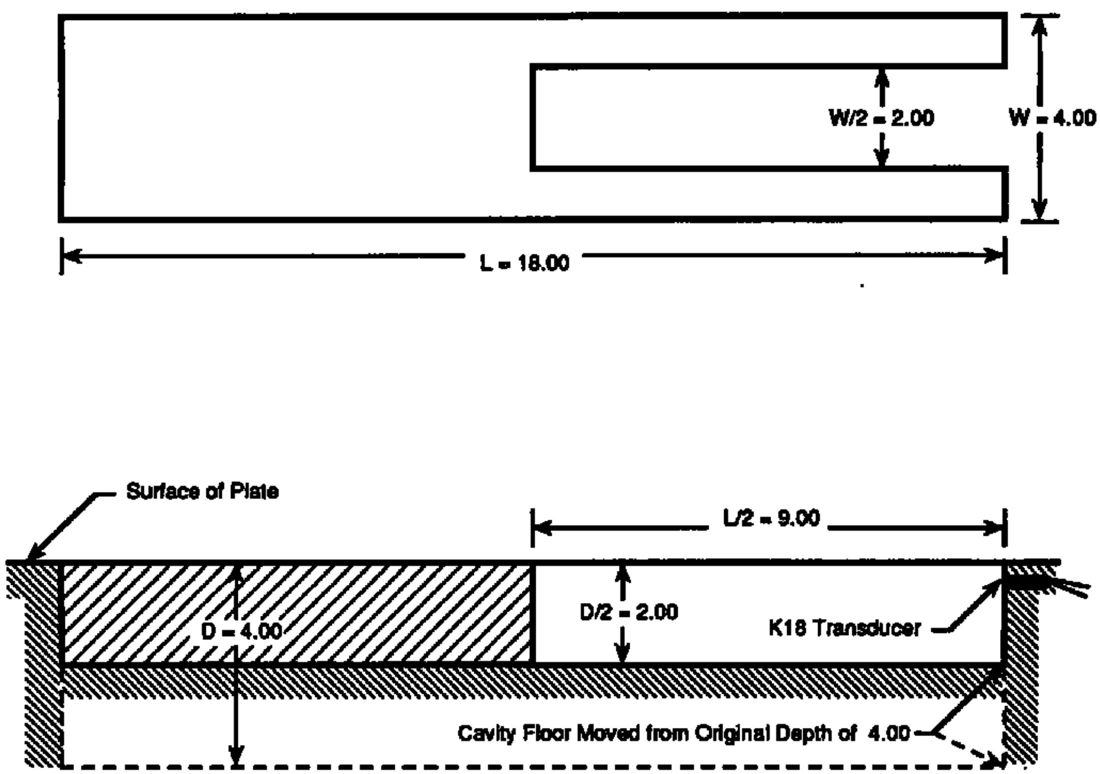

Figure A-2. U-block cavity insert.

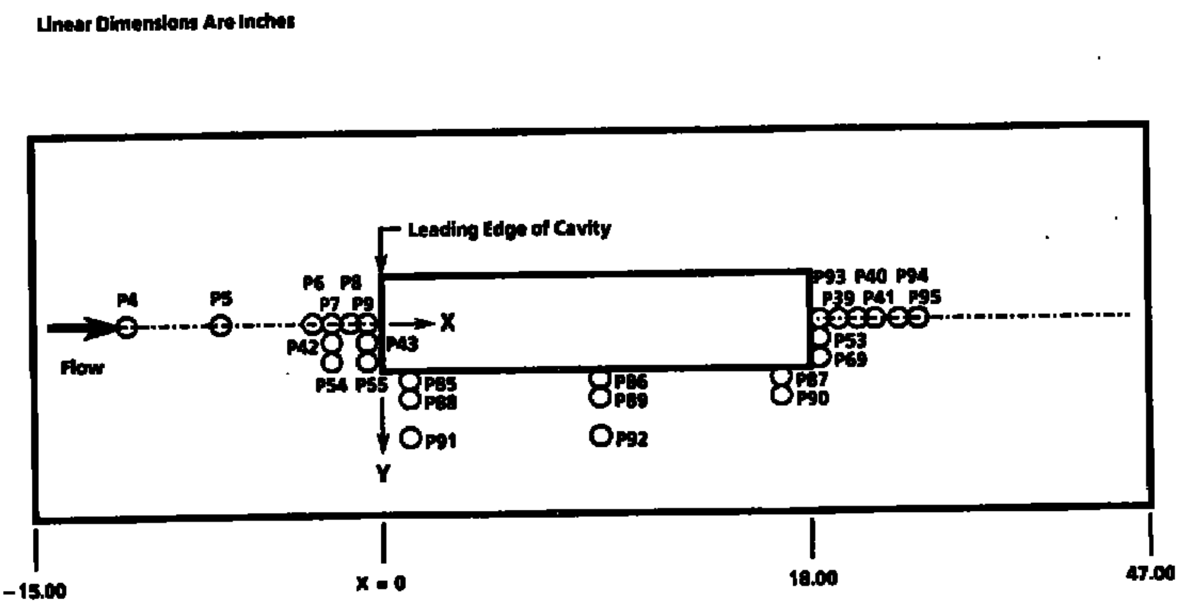

Planform View of Flat Plate

a. Location of pressure orifices on the flat plate
Figure A-3. Pressure orifice locations.

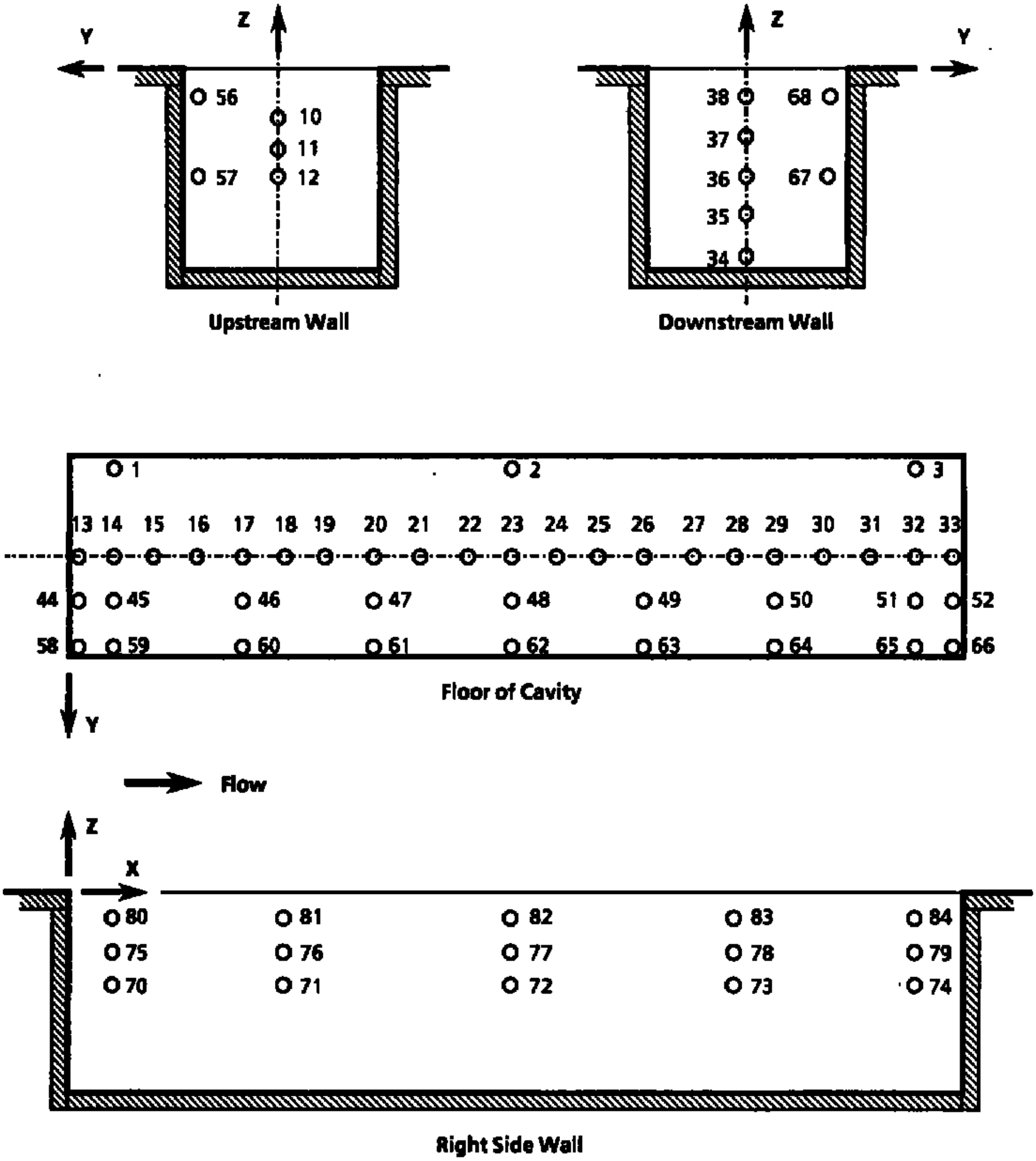

b. Location of pressure orifices in the cavity
Figure A-3. Continued.

Pressure Orifice Locations

Orifice Number	X Model, in.	X/L	Y Model, in.	Y/W/2	Z Model, in.
1	0.9	0.05	-1.8	-0.90	-D
2	9.0	0.50	-1.8	-0.90	-D
3	17.1	0.95	-1.8	-0.90	-D
4	-11.0	-0.611	0	0	0
5	-7.0	-0.389	0	0	0
6	-3.0	-0.167	0	0	0
7	-2.1	-0.117	0	0	0
8	-1.2	-0.067	0	0	0
9	-0.3	-0.017	0	0	0
10	0	0	0	0	-0.95
11	0	0	0	0	-1.55
12	0	0	0	0	-2.15
13	0.1	0.006	0	0	-D
14	0.9	0.050	0	0	-D
15	1.8	0.100	0	0	-D
16	2.7	0.150	0	0	-D
17	3.6	0.200	0	0	-D
18	4.5	0.250	0	0	-D
19	5.4	0.300	0	0	-D
20	6.3	0.350	0	0	-D
21	7.2	0.400	0	0	-D
22	8.1	0.450	0	0	-D
23	9.0	0.500	0	0	-D
24	9.9	0.550	0	0	-D
25	10.8	0.600	0	0	-D
26	11.7	0.650	0	0	-D
27	12.6	0.700	0	0	-D
28	13.5	0.750	0	0	-D
29	14.4	0.800	0	0	-D
30	15.3	0.850	0	0	-D
31	16.2	0.900	0	0	-D
32	17.1	0.950	0	0	-D
33	17.9	0.994	0	0	-D
34	18.0	1.0	0	0	-3.75
35	18.0	1.0	0	0	-2.95
36	18.0	1.0	0	0	-2.15
37	18.0	1.0	0	0	-1.35
38	18.0	1.0	0	0	-0.55
39	18.7	1.039	0	0	0
40	19.2	1.067	0	0	0
41	20.1	1.117	0	0	0
42	-2.1	-0.117	0.9	0.45	0
43	-0.3	-0.017	0.9	0.45	0
44	0.1	0.006	0.9	0.45	-D
45	0.9	0.050	0.9	0.45	-D
46	3.6	0.200	0.9	0.45	-D
47	6.3	0.350	0.9	0.45	-D
48	9.0	0.500	0.9	0.45	-D
49	11.7	0.650	0.9	0.45	-D
50	14.4	0.800	0.9	0.45	-D
51	17.1	0.950	0.9	0.45	-D
52	17.9	0.994	0.9	0.45	-D
53	18.7	1.039	0.9	0.45	0
54	-2.1	-0.117	1.8	0.90	0
55	-0.3	-0.017	1.8	0.90	0
56	0	0	1.9	0.95	-0.55
57	0	0	1.9	0.95	-2.15
58	0.1	0.006	1.8	0.90	-D
59	0.9	0.050	1.8	0.90	-D
60	3.6	0.200	1.8	0.90	-D
61	6.3	0.350	1.8	0.90	-D
62	9.0	0.500	1.8	0.90	-D
63	11.7	0.650	1.8	0.90	-D
64	14.4	0.800	1.8	0.90	-D
65	17.1	0.950	1.8	0.90	-D
66	17.9	0.994	1.8	0.90	-D

c. Location of pressure orifices
Figure A-3. Continued.

Pressure Orifice Locations, Concluded

Orifice Number	X Model, in.	X/L	Y Model, in.	Y/W/2	Z Model, in.
67	18.0	1.000	1.9	0.950	-2.15
68	18.0	1.000	1.9	0.950	-0.55
69	18.7	1.039	1.8	0.900	0
70	0.9	0.050	2.0	1.000	-1.95
71	4.5	0.250	2.0	1.000	-1.95
72	9.0	0.500	2.0	1.000	-1.95
73	13.5	0.750	2.0	1.000	-1.95
74	17.1	0.950	2.0	1.000	-1.95
75	0.9	0.050	2.0	1.000	-1.15
76	4.5	0.250	2.0	1.000	-1.15
77	9.0	0.500	2.0	1.000	-1.15
78	13.5	0.750	2.0	1.000	-1.15
79	17.1	0.950	2.0	1.000	-1.15
80	0.9	0.050	2.0	1.000	-0.35
81	4.5	0.250	2.0	1.000	-0.35
82	9.0	0.500	2.0	1.000	-0.35
83	13.5	0.750	2.0	1.000	-0.35
84	17.1	0.950	2.0	1.000	-0.35
85	1.2	0.067	2.3	1.150	0
86	8.8	0.489	2.3	1.150	0
87	16.8	0.933	2.3	1.150	0
88	1.2	0.067	3.2	1.600	0
89	8.8	0.489	3.2	1.600	0
90	16.8	0.933	3.2	1.600	0
91	1.2	0.067	6.2	3.100	0
92	8.8	0.489	6.2	3.100	0
93	18.100	1.006	0	0	0
94	20.775	1.154	0	0	0
95	21.775	1.210	0	0	0

d. Location of pressure orifices, concluded
Figure A-3. Concluded.

Linear Dimensions Are Inches

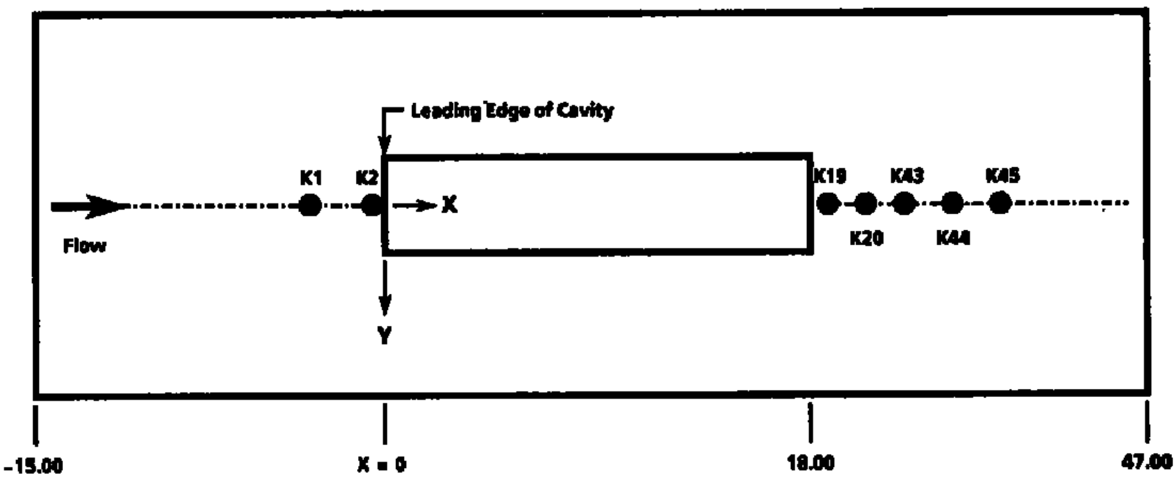

Planform View of Flat Plate

a. Location of pressure transducers on the flat plate
Figure A-4. Pressure transducer locations.

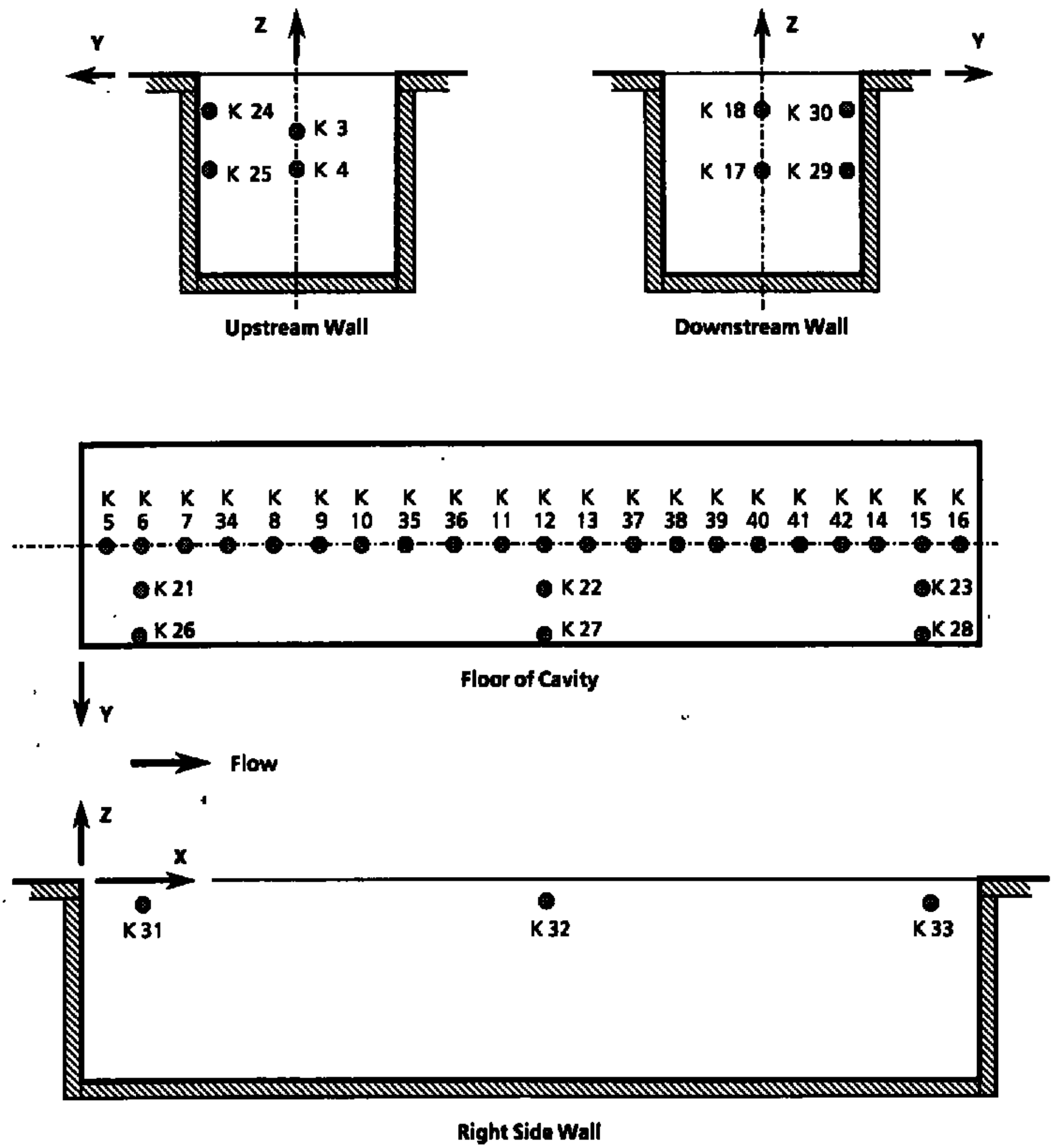

b. Location of pressure transducers in the cavity
Figure A-4. Continued.

Pressure Transducer Locations

Transducer Number	X Model, in.	X/L	Y Model, in.	Y/W/2	Z Model, in.
K 1	-3.175	-0.176	0	0	0
K 2	-0.475	-0.026	0	0	0
K 3	0	0	0	0	-1.125
K 4	0	0	0	0	-1.975
K 5	0.275	0.015	0	0	-D
K 6	1.075	0.060	0	0	-D
K 7	1.975	0.110	0	0	-D
K 8	3.775	0.210	0	0	-D
K 9	4.675	0.260	0	0	-D
K 10	5.575	0.310	0	0	-D
K 11	8.275	0.460	0	0	-D
K 12	9.175	0.510	0	0	-D
K 13	10.075	0.560	0	0	-D
K 14	16.025	0.890	0	0	-D
K 15	16.925	0.940	0	0	-D
K 16	17.725	0.985	0	0	-D
K 17	18.000	1.000	0	0	-1.975
K 18	18.000	1.000	0	0	-0.725
K 19	18.875	1.049	0	0	0
K 20	20.275	1.126	0	0	0
K 21	1.075	0.060	0.9	0.45	-D
K 22	9.175	0.510	0.9	0.45	-D
K 23	16.925	0.940	0.9	0.45	-D
K 24	0	0	1.9	0.95	-0.725
K 25	0	0	1.9	0.95	-1.975
K 26	1.075	0.060	1.8	0.90	-D
K 27	9.175	0.510	1.8	0.90	-D
K 28	16.925	0.940	1.8	0.90	-D
K 29	18.000	1.000	1.9	0.95	-1.975
K 30	18.000	1.000	1.9	0.95	-0.725
K 31	1.075	0.060	2.0	1.00	-0.35
K 32	9.175	0.510	2.0	1.00	-0.35
K 33	16.925	0.940	2.0	1.00	-0.35
K 34	2.875	0.160	0	0	-D
K 35	6.475	0.360	0	0	-D
K 36	7.375	0.410	0	0	-D
K 37	10.975	0.610	0	0	-D
K 38	11.875	0.660	0	0	-D
K 39	12.775	0.710	0	0	-D
K 40	13.675	0.760	0	0	-D
K 41	14.575	0.810	0	0	-D
K 42	15.475	0.860	0	0	-D
K 43	21.950	1.219	0	0	0
K 44	23.950	1.331	0	0	0
K 45	25.950	1.442	0	0	0

c. Pressure transducer locations
Figure A-4. Concluded.

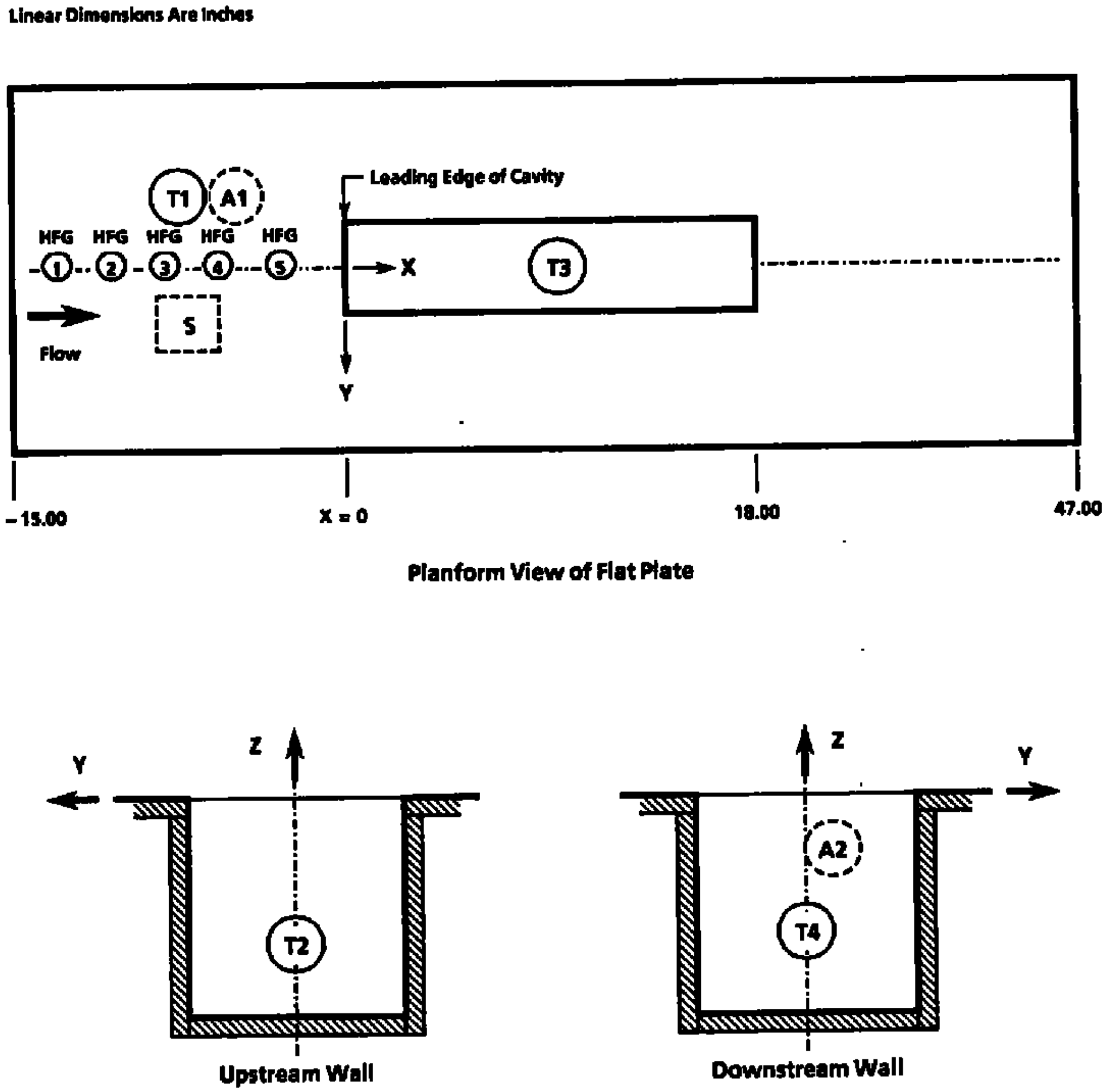

Figure A-5. Locations of other sensors.

LOCATIONS OF OTHER SENSORS

Instrument	X Model, in.	X/L	Y Model, in.	Y/W/2	Z Model, in.
Hot-Film Gages					
HFG 1	- 11.0	- 0.722	0.25	0.125	0
HFG 2	- 7.0	- 0.389	0.25	0.125	0
HFG 3	- 3.0	- 0.167	0.25	0.125	0
HFG 4	- 1.262	- 0.070	0.25	0.125	0
HFG 5	- 0.388	- 0.022	0.25	0.125	0
Thermocouples					
T 1	- 4.5	- 0.25	- 0.5	- 0.25	- 0.2
T 2	- 0.1	- 0.01	- 0.5	- 0.25	- 2.0
T 3	9.0	0.50	- 0.5	- 0.25	- (H + 0.2)
T 4	18.1	1.01	- 0.5	- 0.25	0
Accelerometers					
A 1	- 6.0	- 0.33	- 0.5	- 0.25	- 0.25
A 2	18.0	1.00	0.5	0.25	- 1.0
Inclinometer, S	- 9.0	- 0.50	0	0	- 0.25

Figure A-5. Concluded.

Linear Dimensions Are Inches

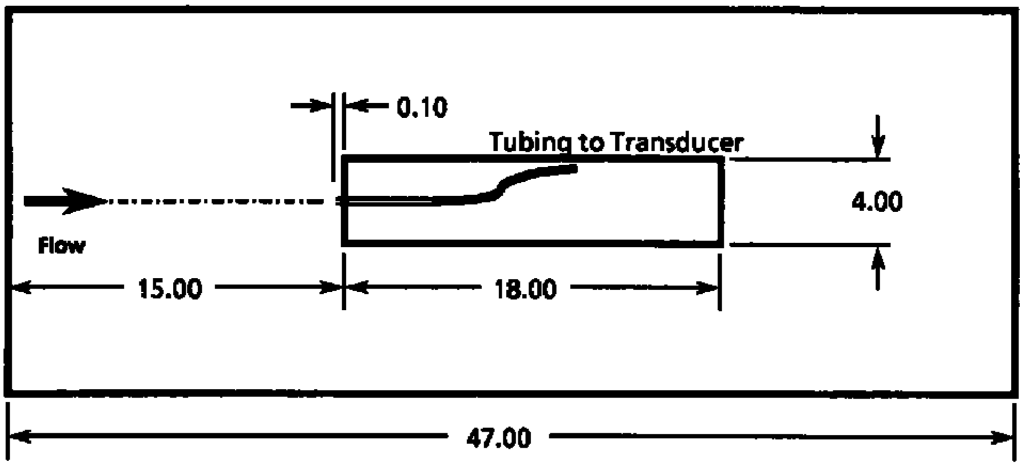

Top View (As Mounted in Wind Tunnel) of Plate/Cavity Model, Showing Boundary-Layer Rake

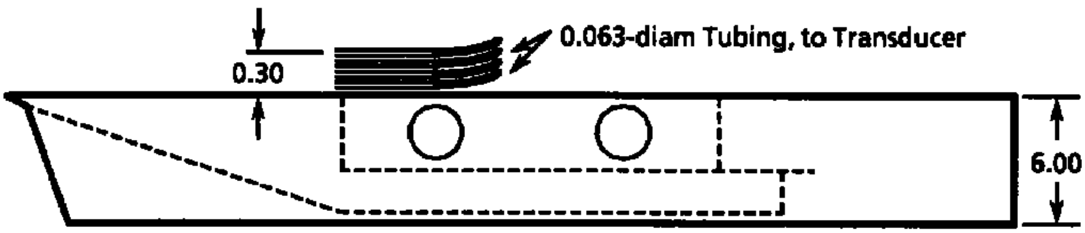

Side View of Plate/Cavity Model, Showing Boundary-Layer Rake

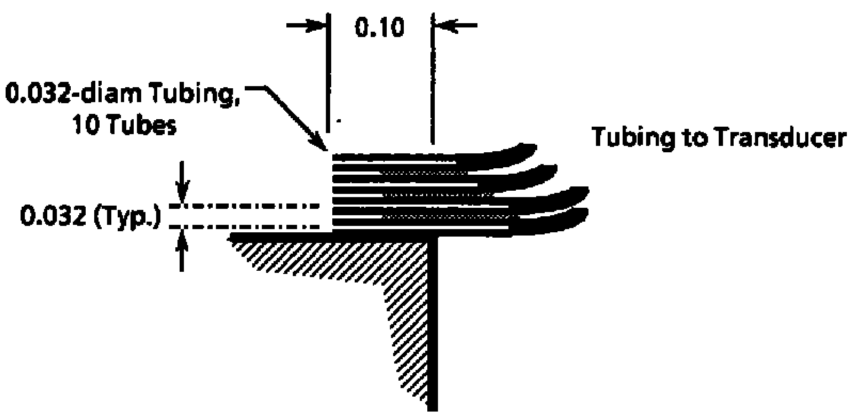

Detail View of Boundary-Layer Rake Installation

Figure A-6. Boundary-layer rake.

Table A-1. Nominal Flow Conditions for the Tests

M_∞	P_t, psf	T_t, °R	V_∞, ft/sec	q_∞, psf	Re, 1/ft
0.60	615	545	663	121	1.0×10^6
0.60	1,200	550	670	238	1.9×10^6
0.60	1,235	550	666	244	2.0×10^6
0.60	1,900	555	670	375	3.0×10^6
0.75	1,208	547	818	328	2.2×10^6
0.80	1,200	556	871	352	2.3×10^6
0.85	1,200	547	911	376	2.3×10^6
0.90	1,200	547	957	403	2.4×10^6
0.95	478	542	998	169	1.0×10^6
0.95	980	545	1,000	343	2.0×10^6
0.95	1,200	550	1,008	424	2.5×10^6
0.95	1,480	551	1,008	525	3.0×10^6
1.00	1,188	548	1,028	430	2.5×10^6
1.05	468	545	1,089	180	1.0×10^6
1.05	948	548	1,091	366	2.0×10^6
1.05	1,200	550	1,095	463	2.5×10^6
1.05	1,447	554	1,099	557	3.0×10^6
1.10	1,200	549	1,135	476	2.5×10^6
1.15	1,200	551	1,178	490	2.6×10^6
1.20	455	544	1,208	189	1.0×10^6
1.20	930	547	1,212	386	2.0×10^6
1.20	1,200	552	1,220	499	2.6×10^6
1.20	1,411	552	1,219	586	3.0×10^6
1.30	1,197	555	1,297	511	2.5×10^6
1.40	1,208	558	1,374	520	2.5×10^6
1.50	510	558	1,448	219	1.0×10^6
1.50	987	557	1,441	424	2.0×10^6
1.50	1,200	557	1,442	515	2.4×10^6
1.50	1,398	562	1,447	600	2.8×10^6
1.60	1,202	557	1,506	506	2.4×10^6
1.75	1,200	556	1,593	483	2.3×10^6
1.90	1,207	566	1,674	455	2.2×10^6
2.00	1,200	560	1,728	430	2.0×10^6
2.00	1,400	562	1,734	501	2.4×10^6
2.00	619	580	1,760	222	1.0×10^6
2.00	1,238	580	1,760	444	2.0×10^6
2.00	1,858 12.90	580	1,760	665	3.0×10^6
2.26	2,088	580	1,877	635	3.0×10^6
2.50	2,376	580	1,968	608	3.0×10^6
2.75	907	580	2,048	192	1.0×10^6
2.75	1,814	580	2,048	526	2.0×10^6
2.75	2,635 18.3	580	2,048	554	3.0×10^6
3.51	4,032 28	580	2,227	449	3.0×10^6
5.04	9,115 63.3	600	2,454	292	3.0×10^6

Table A-2. Statistical Confidence Intervals for the Static Pressure Coefficient.

M_∞	P_t, psf	q_∞, psf	$\varepsilon(q_\infty)$, psf	P_∞, psf	$\varepsilon(P_\infty)$, psf	$\varepsilon(C_p)$
0.60	615	121	± 3.28	480	± 2.78	± 0.023
0.60	1,200	238	± 5.48	920	± 2.78	± 0.012
0.60	1,235	244	± 5.62	960	± 2.78	± 0.012
0.60	1,900	375	± 8.33	1,485	± 2.78	± 0.008
0.75	1,208	328	± 6.89	825	± 2.78	± 0.009
0.80	1,200	352	± 7.31	790	± 2.78	± 0.008
0.85	1,200	376	± 7.76	745	± 2.78	± 0.008
0.90	1,200	403	± 8.22	710	± 2.78	± 0.007
0.95	478	169	± 4.49	265	± 2.78	± 0.016
0.95	980	343	± 7.31	535	± 2.78	± 0.008
0.95	1,200	424	± 8.68	675	± 2.78	± 0.007
0.95	1,480	525	± 10.5	815	± 2.78	± 0.006
1.00	1,188	430	± 9.05	625	± 2.78	± 0.007
1.05	468	180	± 4.91	235	± 2.78	± 0.015
1.05	948	366	± 7.87	470	± 2.78	± 0.008
1.05	1,200	463	± 9.59	595	± 2.78	± 0.006
1.05	1,447	557	± 11.3	720	± 2.78	± 0.005
1.10	1,200	476	± 10.1	560	± 2.78	± 0.006
1.15	1,200	490	± 10.5	525	± 2.78	± 0.006
1.20	455	189	± 5.54	188	± 2.78	± 0.015
1.20	930	386	± 8.85	383	± 2.78	± 0.008
1.20	1,200	499	± 11.0	494	± 2.78	± 0.006
1.20	1,411	586	± 12.6	580	± 2.78	± 0.005
1.30	1,197	511	± 11.9	434	± 2.78	± 0.006
1.40	1,208	520	± 12.9	377	± 2.78	± 0.006
1.50	510	219	± 7.34	137	± 2.78	± 0.013
1.50	987	424	± 11.6	267	± 2.78	± 0.007
1.50	1,200	515	± 13.7	327	± 2.78	± 0.006
1.50	1,398	600	± 15.7	380	± 2.78	± 0.005
1.60	1,202	506	± 14.6	280	± 2.78	± 0.006
1.75	1,200	483	± 16.0	225	± 2.78	± 0.006
1.90	1,207	455	± 17.4	180	± 2.78	± 0.006
2.00	1,200	430	± 18.3	150	± 2.78	± 0.007
2.00	1,400	501	± 20.9	155	± 2.78	± 0.006
2.00	619	222	± 2.44	78.8	± 1.87	± 0.011
2.00	1,238	444	± 4.88	158	± 1.87	± 0.011
2.00	1,858	665	± 7.32	237	± 1.87	± 0.011
2.26	2,088	643	± 8.26	181	± 1.87	± 0.010
2.50	2,376	605	± 7.90	138	± 1.87	± 0.008
2.75	907	188	± 2.88	35.6	± 1.87	± 0.007
2.75	1,814	383	± 7.89	72.4	± 1.87	± 0.007
2.75	2,635	554	± 8.31	105	± 1.87	± 0.007
3.51	4,032	449	± 5.48	52.1	± 1.87	± 0.006
5.04	9,115	293	± 6.37	16.5	± 1.87	± 0.006

APPENDIX B

UNSTEADY FLOW IN A TUBE

Originally, the analytical effort described here was undertaken to determine the dynamics of a single-tube pressure-measuring system similar to the concept illustrated as follows:

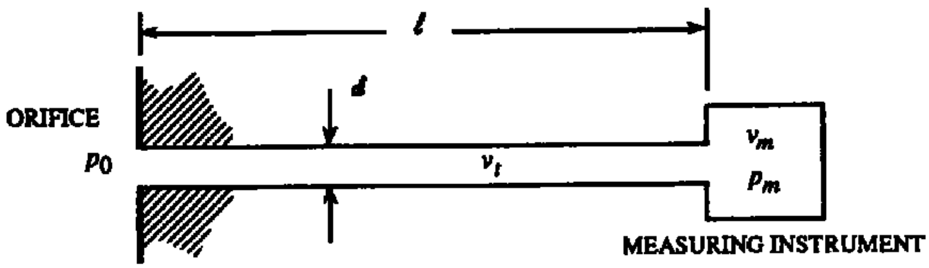

During the development of the cavity model described in the body of this report, it was assumed that the principles described here could be applied. The theory is based on Poiseuille's equation for unsteady flow derived in Ref. B-1, from which follows

$$\frac{d^2 p_m}{d t^2} + 2\omega_0\zeta \frac{d p_m}{d t} + \omega_0^2 p_m = \omega_0^2 p_0 - \frac{1}{1 + \frac{2v_m}{v_t}} \left[\frac{d^2 p_o}{d t^2} + 2\omega_0\zeta \frac{d p_0}{d t}\right]$$

where

$$\omega_0\zeta = \frac{32\,\mu\,RT}{d^2\,(p_0 + p_m)}$$

$$\omega_0^2 = \frac{2\,R\,T}{\ell^2\left(1 + \frac{2v_m}{v_t}\right)}$$

and the quantity v_t is the volume of the tube.

The equation is linearized by assuming that the orifice pressure, p_0, is given by

$$p_0 = A + B \sin \omega t$$

and that

$$p_0 \approx p_m$$

Substituting into the previous fundamental equation produces

$$\frac{d^2 p_m}{d t^2} + 2\omega_0\zeta \frac{d p_m}{d t} + \omega_0^2 p_m$$

$$= A\,\omega_0^2 - \frac{B\,\omega^2}{1 + \dfrac{2v_m}{v_t}} \sqrt{\left(\frac{2\,\omega_0\zeta}{\omega}\right)^2 + \left[\left(\frac{\omega_0}{\omega}\right)^2 \left(1 + 2\frac{v_m}{v_t}\right) + 1\right]^2}\ \sin(\omega t - \theta)$$

where

$$\tan\theta = \frac{2\,\zeta\left(\dfrac{\omega_0}{\omega}\right)}{\left(\dfrac{\omega_0}{\omega}\right)^2\left(1 + \dfrac{2\,v_m}{v_t}\right) + 1}$$

The steady solution for p_m is

$$p_m = A + \frac{B}{\left(1 + \dfrac{2\,v_m}{v_t}\right)} \left(\frac{\sin\beta}{\sin\theta}\right) \sin(\omega t - \theta - \beta)$$

where

$$\tan\beta = \frac{2\,\zeta\left(\dfrac{\omega_0}{\omega}\right)}{\left(\dfrac{\omega_0}{\omega}\right)^2 - 1}$$

The frequency response function is

$$R_s = \frac{\sin\beta}{\left(1 + \dfrac{2\,v_m}{v_t}\right)\sin\theta}$$

Substituting the expressions for θ and $\tan\beta$ into the frequency response equation, and setting $v_m = 0$ (a valid assumption for cavity geometry), the equation for R_s becomes

$$R_s = \left\{\frac{\left[1 + \left(\dfrac{\omega}{\omega_0}\right)^2\right]^2 + 4\,\zeta^2\left(\dfrac{\omega}{\omega_0}\right)^2}{\left[1 - \left(\dfrac{\omega}{\omega_0}\right)^2\right]^2 + 4\,\zeta^2\left(\dfrac{\omega}{\omega_0}\right)^2}\right\}^{\frac{1}{2}}$$

REFERENCE

B-1. Bauer, R. C. "A Method of Calculating the Response Time of Pressure Measuring Systems." AEDC-TR-56-7, November 1956.

APPENDIX C

CAVITY ACOUSTIC RESPONSE PHASE PARAMETER, γ

Acting on a suspicion that refined values might be selected for Rossiter's cavity acoustic phase parameter, γ, a study was made of the parameter by Dobson (Ref. 24). It was thought that γ might be some function of mode number and Mach number. First, the modified Rossiter equation was used with the conventional value of γ of 0.25 to construct a graph of Strouhal number as a function of free-stream Mach number, Fig. C-1. Data points from the current experiments as well as from several other experiments (Refs. 4 and 12) were marked on the graph. Then, at each Mach number for a selected cavity, an appropriate value of γ was selected to predict modal frequencies that would match the measured values. The averages of the γ values over all the Mach numbers of the current study where modes could be identified were as follows:

Cavity L/D	Mode	Adjusted γ
4.5	1	0.2473
	2	0.2281
	3	0.1344
9.0	1	(Tones Too Weak)
	2	0.4510
	3	0.3653

Using these values of γ, another set of Strouhal curves was generated, and the experimental data of Fig. C-1 were copied, forming Fig. C-2. Somewhat better correlation was provided by the adjusted values of γ than the original Rossiter values, especially for the cavity of L/D = 9.0.

Note that the data of Plumblee et al. (Ref. 4) do not correlate well with the predictions made using the Rossiter model and either value of γ (Figs. C-1 and C-2a). As mentioned in Section 1.0, the L/D of one of Plumblee's cavities was 0.8, in which Plumblee asserts that vertical modes dominate. Therefore, in treating only longitudinal modes, the Rossiter model is incomplete.

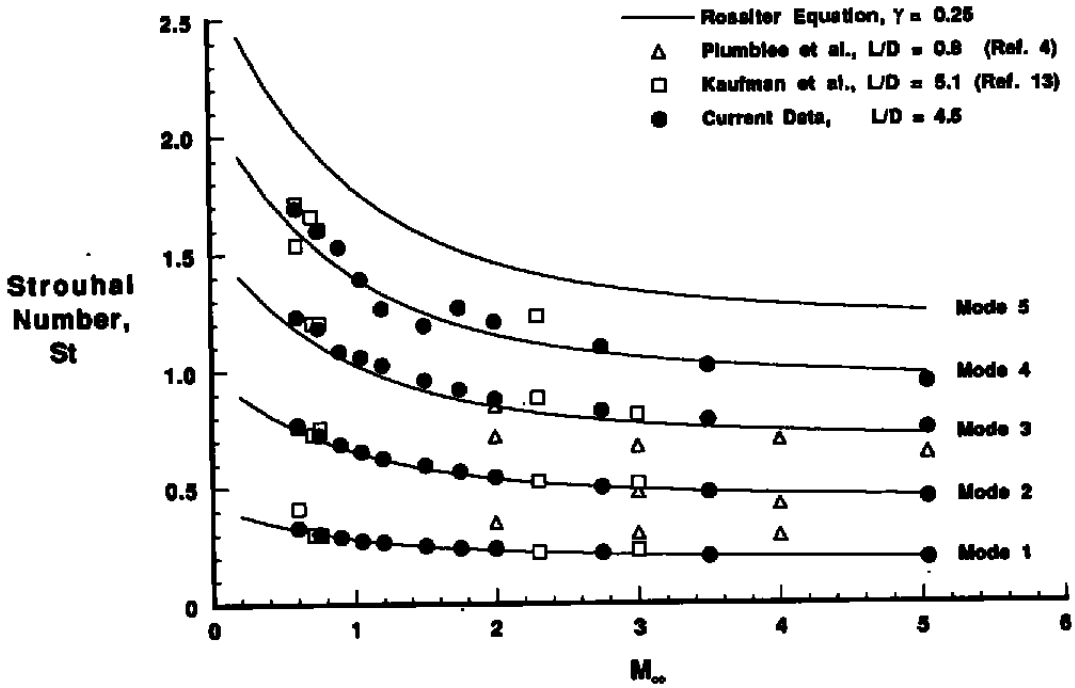

a. Deep cavities, L/D ≤ 5.1

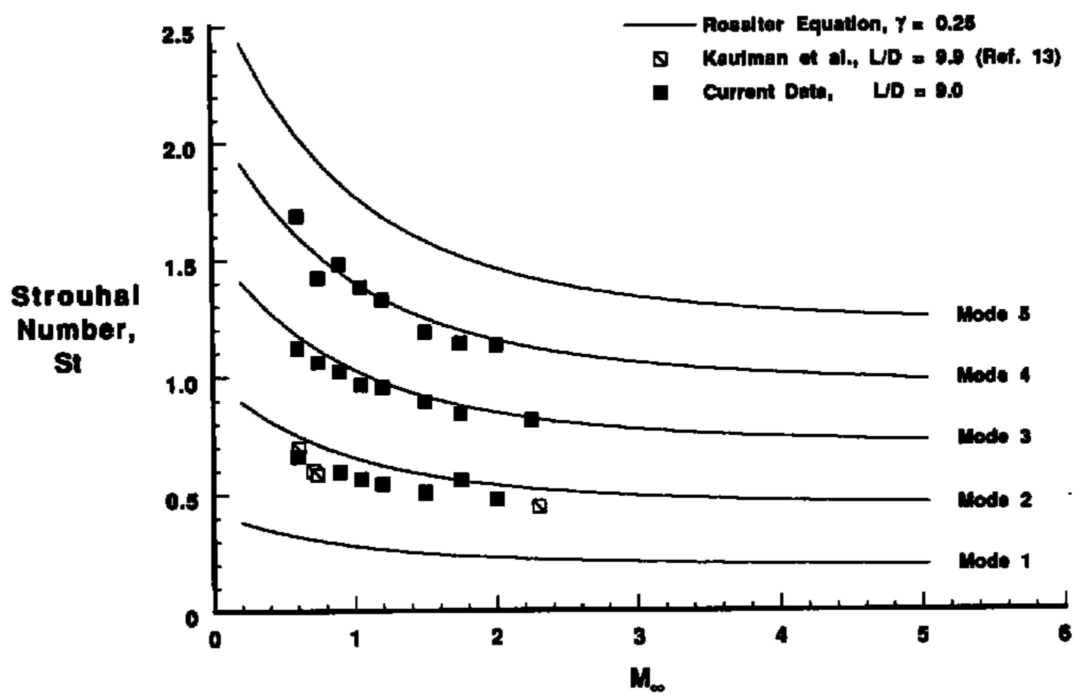

b. Transitional cavities, 9 ≤ L/D ≤ 13

Figure C-1. Strouhal number correlation of detected tones and tones predicted using Rossiter's equation with $\gamma = 0.25$.

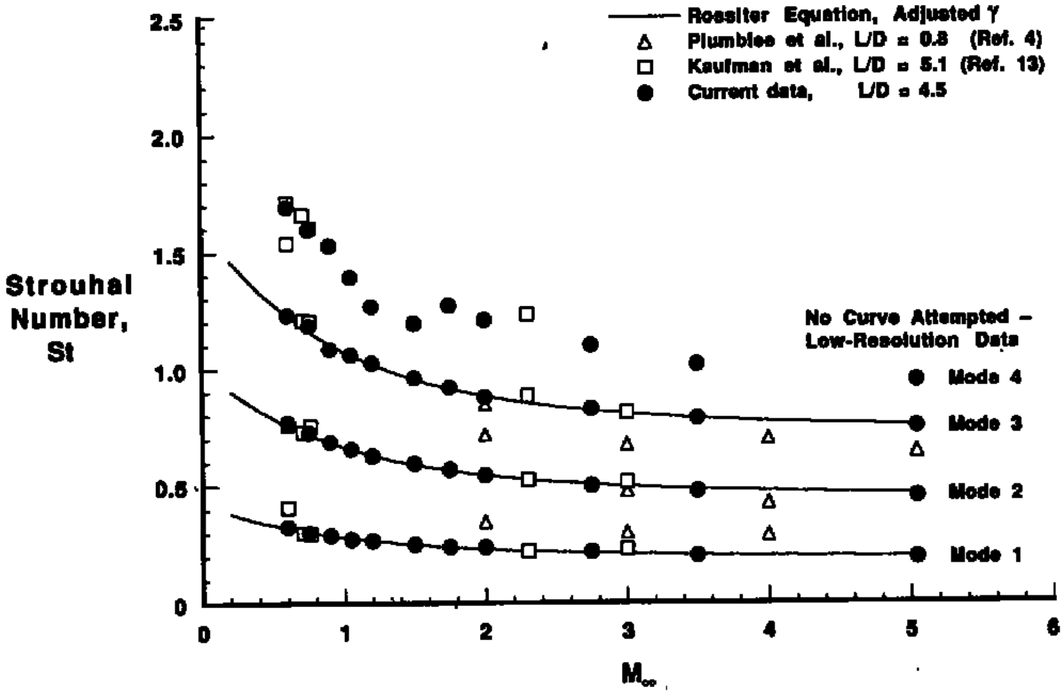

a. Deep cavities, L/D ≤ 5.1

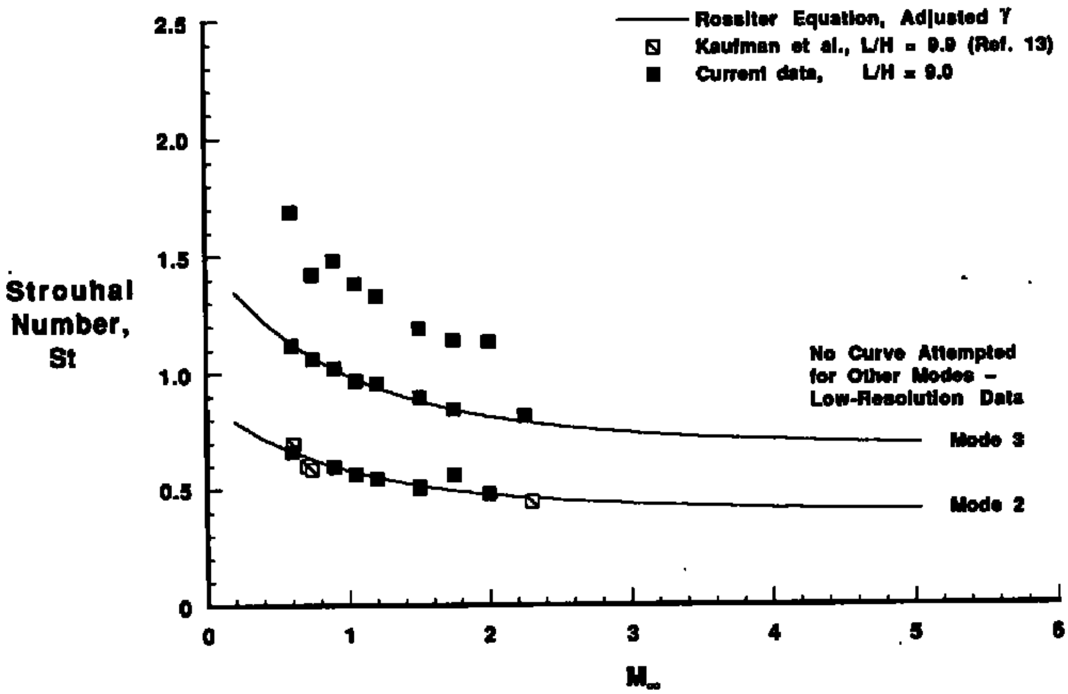

b. Transitional cavities, 9 ≤ L/D ≤ 13

Figure C-2. Strouhal number correlation of detected tones and tones predicted using Rossiter's equation with adjusted values of γ.

NOMENCLATURE

A	Accelerometer
a	Speed of sound, ft/sec
a_t	Speed of sound based on free-stream total temperature, ft/sec
a_n	Constant coefficients in a Fourier transform, n = 1, 2, 3, ... , 512
a_1	Constant assumed = 0.3
a_∞	Speed of sound based on free-stream static temperature, ft/sec
C_f	Friction coefficient along the dividing streamline between the turbulent mixing zone and the cavity, $= F_s/q_\infty$
C_P	Pressure coefficient, $= (P - P_\infty)/q_\infty$
C_∞	Crocco number, $C_\infty^2 = V_\infty^2/(2\ c_p\ T_t)$
c_p	Specific heat at constant pressure
D	Depth of the cavity, inches
d	Effective damping ratio
d_n	Effective damping ratio for the n^{th} coefficient in the wall pressure equation
d_w	Wave damping coefficient
d_μ	Viscous damping coefficient
d	Tube diameter, ft
F_s	Shear force along the dividing streamline between the turbulent mixing zone and the cavity
f	Frequency, Hz

f_D	Natural acoustic frequency of the cavity, depth mode, Hz
f_e	Edgetone frequency, Hz
f_L	Natural acoustic frequency of the cavity, length mode, Hz
f_m	Modal frequency, Hz
f_W	Natural acoustic frequency of the cavity, width mode, Hz
HFG	Hot-film gage
I_d	Momentum of mass flow entrained in the turbulent mixing zone, normalized by $\varrho_\infty V_\infty^2$
K	Kulite® pressure transducer (accompanying digits identify a specific transducer)
L	Length of the cavity, inches
L/D	Ratio of cavity length to cavity depth
ℓ	Tube length, ft
M_∞	Mach number in the free stream
m_a	Mode number for acoustic waves generated in the cavity
m_v	Mode number for vortices generated at the upstream edge of the cavity
$\dot{m}_b$	Mass injection (bleed-in) flow rate, lbsm/sec
OASPL	Overall sound pressure level, db (overall rms pressure converted to a sound pressure level using a reference of 2.9×10^{-9} psi)
P and p	Static pressure, psfa
P_{ref}	A reference pressure for calculation of SPL, usually the international threshold of audibility, 2 Pa ($\approx 2.9 \times 10^{-9}$ psi)
P_{rms}	Root-mean-square of fluctuating pressure values, psi

P_t	Total, or stagnation pressure, psfa
P_{wall}	Pressure acting on the downstream wall of the cavity, psi
P_∞	Static pressure in the free stream, psf
p_m	Static pressure in the sensing chamber of a pressure-measuring instrument, psf
p_0	Static pressure at an orifice, psf
q_∞	Dynamic pressure in the free stream, psf
R	Specific gas constant
Re	Unit Reynolds number, per foot
R_s	Response function or coefficient
rms	Root mean square
SPL	Sound pressure level, db (referenced to 2.9×10^{-9} psi)
St	Strouhal number, $f\ L/V_\infty$
s^2	Sample variance of n repeated static pressure measurements
T	Static temperature, °R
T_t	Total temperature in the free stream, °R
t	Time, sec
u	Local X-direction component of fluid velocity, ft/sec
u_{rms}	Root-mean-square value of the local X-component of fluid velocity, ft/sec
$\bar{u}$	Mean value of the local X-component of fluid velocity, ft/sec
V_b	Velocity of the fluid injected into a boundary layer, ft/sec

V_{∞} Velocity in the free stream, ft/sec

v_m Volume of the sensing chamber of a pressure-measuring instrument, ft^3

v_t Volume of the tube connecting an orifice and the sensing chamber of a pressure-measuring instrument, ft^3

W Width of the generic cavity, inches

X Distance from the leading edge of the cavity opening in the flat plate, measured in the X direction, inches

Y Distance from the longitudinal centerline of the cavity opening in the flat plate, measured in the Y direction, inches

Z Displacement from the plane of the surface of the flat plate, measured in the Z direction, inches

β A parametric angle, rad

γ Ratio of specific heats for a gas (Sections 2.3.1 and 2.3.5)

γ Rossiter's phase constant (Ref. 5)

δ Turbulent boundary-layer height, inches

δ_0 Turbulent boundary-layer height at the leading edge of a cavity, inches

δ^* Displacement thickness of a boundary layer, inches

$\epsilon(\ )$ Half-width of a two-standard-deviation (2σ) bandwidth of values of the independent variable that is calculated to include approximately 95 percent of the measurements of the independent variable

ζ Viscous damping ratio

η_p A mixing position parameter (Ref. 27)

θ A parametric angle, rad

λ_a	Wave length for acoustic waves
λ_v	Wave length for vortices
μ_t	Viscosity of a gas at the total temperature of the free stream
ϱ	Density of a gas
$\bar{\varrho}$	Mean density of a gas with fluctuating pressure
σ	Similarity parameter for turbulent mixing
σ_0	Similarity parameter for turbulent mixing of a single stream
τ_{KE}	Turbulent kinetic energy in the mixing zone, $= u_{rms}^2/2$
ϕ_c	Ratio of mass injection (bleed-in) velocity to free-stream velocity
ϕ_d	Ratio of the mixing zone/cavity dividing streamline velocity to free-stream velocity
ω	Arbitrary forcing frequency, rad/sec
ω_n	The n^{th} forcing frequency of the 512 frequencies assumed as a model of the fluctuating wall pressure in a cavity
ω_0	Undamped natural frequency, rad/sec

CAVITY AXIS SYSTEM

Origin: At a point on the cavity opening leading edge (defined by the intersection of two planes; the surface of the flat plate and the forward wall of the cavity), and midway between the sides of the cavity opening.

Directions of the Axes:

X	Parallel to the longitudinal axis of symmetry of the generic flat plate/cavity model, and in the plane of the opening of the cavity, positive downstream.
Y	Perpendicular to the X and Z axes and in the plane of the opening of the cavity.
Z	Perpendicular to the plane of the cavity opening, with the positive direction pointing away from the cavity.